Ultrafast Dynamics in Condensed Matter

University of Potsdam

Dissertation

Hybrid Nanolayer Architectures for Ultrafast Acousto-Plasmonics in Soft Matter.

Author:
Elena Pavlenko

First assessor:
Prof. Dr. Matias Bargheer

Second assessor:
Prof. Dr. Svetlana Santer

Third assessor:
Prof. Dr. Aurélien Crut

Faculty of Mathematics and Science
Institute of Physics and Astronomy

June 2016

Published online at the
Institutional Repository of the University of Potsdam:
URN urn:nbn:de:kobv:517-opus4-99544
http://nbn-resolving.de/urn:nbn:de:kobv:517-opus4-99544

Abstract

The goal of the presented work is to explore the interaction between gold nanorods (GNRs) and hyper-sound waves. For the generation of the hyper-sound I have used Azobenzene-containing polymer transducers. Multilayer polymer structures with well-defined thicknesses and smooth interfaces were built via layer-by-layer deposition. Anionic polyelectrolytes with Azobenzene side groups (PAzo) were alternated with cationic polymer PAH, for the creation of transducer films. PSS/PAH multilayer were built for spacer layers, which do not absorb in the visible light range. The properties of the PAzo/PAH film as a transducer are carefully characterized by static and transient optical spectroscopy. The optical and mechanical properties of the transducer are studied on the picosecond time scale. In particular the relative change of the refractive index of the photo-excited and expanded PAH/PAzo is $\Delta n/n = -2.6*10^{-4}$. Calibration of the generated strain is performed by ultrafast X-ray diffraction calibrated the strain in a Mica substrate, into which the hyper-sound is transduced. By simulating the X-ray data with a linear-chain-model the strain in the transducer under the excitation is derived to be $\Delta d/d \sim 5*10^{-4}$.

Additional to the investigation of the properties of the transducer itself, I have performed a series of experiments to study the penetration of the generated strain into various adjacent materials. By depositing the PAzo/PAH film onto a PAH/PSS structure with gold nanorods incorporated in it, I have shown that nanoscale impurities can be detected via the scattering of hyper-sound.

Prior to the investigation of complex structures containing GNRs and the transducer, I have performed several sets of experiments on GNRs deposited on a small buffer of PSS/PAH. The static and transient response of GNRs is investigated for different fluence of the pump beam and for different dielectric environments (GNRs covered by PSS/PAH).

A systematic analysis of sample architectures is performed in order to construct a sample with the desired effect of GNRs responding to the hyper-sound strain wave. The observed shift of a feature related to the longitudinal plasmon resonance in the transient reflection spectra is interpreted as the event of GNRs sensing the strain wave. We argue that the shift of the longitudinal plasmon resonance is caused by the viscoelastic deformation of the polymer around the nanoparticle. The deformation is induced by the out of plane difference in strain in the area directly under a particle and next to it. Simulations based on the linear chain model support this assumption. Experimentally this assumption is proven by investigating the same structure, with GNRs embedded in a PSS/PAH polymer layer.

The response of GNRs to the hyper-sound wave is also observed for the sample structure with GNRs embedded in PAzo/PAH films. The response of GNRs in this case is explained to be driven by the change of the refractive index of PAzo during the strain propagation.

Contents

1. Introduction

Ultrafast acoustics is a method, which allows the extraction of the in-depth information for thin films[1]. This method is well known for the investigation of thin metal films and crystalline structures[2–4]. The idea of the method is to study the interaction between photons and phonons generated in the investigated medium. The coherent phonon wave packets are typically generated by a thin metal transducer that is deposited on top of the investigated structure. Under the excitation by ultrafast laser pulses, the transducer expands and generates phonons in the adjacent medium. An X-ray beam can be used to probe changes in the crystal lattice. Optical probe light can be used to investigate modifications of the material by analyzing the interference between probe light reflected at the surface and the light reflected at the propagating phonon wave packet.

Only recently, this technique was applied to investigate soft matter films. Lomonosov et al[5]. used ultrafast acoustics to investigate the mechanical and optical properties of nanoporous low-k material thin film. Another publication by Ayouch[6] et al. reports about the study of elasticity of an assembly of disordered nanoparticles interacting via either van der Waals-bonded or covalently bonded coating layers. Several[7–10] groups have applied ultrafast acoustics to study cells in vivo and in vitro. In most investigations of the soft films by ultrafast acoustics, a conventional metal transducer, such as Al or Ti is used for the strain generation. The difference in densities of the transducer and the adjacent film leads to mismatch in acoustic impedances. Only a small fraction of the generated strain is transmitted into the investigated structure while the rest is reflected back into the transducer, which leads to multiple reflections and damping. Moreover, it is often challenging to deposit and reliably bond the investigated soft film to a metal transducer. One of the possible ways to improve this situation would be a soft matter transducer. Such a transducer can be made via the layer-by-layer deposition method with a well-defined thickness.

Layer-by-Layer deposition is a simple, cost effective technique for the preparation of thin polymer films with smooth interfaces and well-defined thicknesses[11,12]. This method is based on the electrostatic attraction between the oppositely charged polyelectrolytes, deposited one after another. By using polyelectrolytes functionalized by photosensitive molecules, one can manipulate the resulting films with light. Azobenzene is one of the well-known photosensitive molecules. It undergoes trans to cis isomerization when illuminated by UV-Vis light. Besides numerous studies of the molecular dynamics of photo-excited Azobenzene[13–15], there is also a large number of groups investigating properties and applications of Azobenzene containing polymer films[16–18]. For instance, the reversible change of the thickness and refractive index of a PAzo/PAH multilayer films has been studied by Tanchak et al[19]. However, optical and acoustic properties of Azobenzene-containing polymer films have neither been studied on the ultrafast time scale, nor have such film been considered as a transducer. In the present thesis a detailed and systematic investigation of PAzo/PAH as a transducer for soft and hard materials in presented. The generated strain is calibrated by ultrafast X-ray diffraction.

The layer-by-layer deposition method can be used for the construction of complex composite structures. For instance, it can be used for tuning the plasmon resonances of gold spheres[20] and nanorods[21]. Gold nanorods (GNRs) are widely used for sensing applications in chemistry[22,23,23,24] and biology[25–27]. In most cases, GNRs are covered by a shell in order to prevent clustering, or to obtain certain sensing properties. Even though GNRs are widely used in complex structures, the optical and elastic properties of the functionalized shells of the particles, and interaction of particles with the environment is not well understood. In this work I present several sets of measurements of GNRs in different conditions (different environment, excitation fluence). A systematic analysis of sample architectures, allow us to explore the interaction between gold nanorods (GNRs) and hyper-sound waves.

1.1. Structure of the thesis

I have divided my thesis to 11 chapters. Here I provide a short summary of the main ideas, conveyed in the different chapters.

- In chapter 1 I introduce a short literature overview of the ideas and methods, which motivated this work.
- Chapter 2 provides the theoretical background that is necessary for the phenomena discussed in the thesis. A short description of Azobenzene photo-dynamics is introduced. A brief introduction to the fundamentals of plasmonics is presented, followed by the description of time-domain Brillouin scattering. The basics of the linear-chain model are given at the end of this chapter.
- Chapter 3 contains details about the used materials and sample preparation procedure.
- Chapter 4 describes the methods used for the sample characterization. Details of the UV-Vis spectroscopy and ellipsometry methods are elaborated. The description of the time resolved techniques used in this project is provided in this chapter.
- Chapter 5 contains experimental results for sample structures containing GNRs on a small buffer.
- In chapter 6 I introduce the experimental data for the Azobenzene-based transducer.
- Chapter 7 contains the experimental results for the complex sample architectures, showing the interaction between GNRs and the hyper-sound waves, generated in Azobenzene layer.
- In chapter 8 the results presented in chapters 4-6 are analyzed, compared and discussed.
- Chapter 9 briefly summarizes the main findings of this thesis.
- Chapter 10 contains the discussion about the future prospects of the presented results.
- The Appendix contains the data, used for cross-check purposes.

2. Theoretical background

2.1. Azobenzene isomerization

Azobenzene is a well-studied photosensitive molecule, that has attracted the attention of scientists since 1834[28]. The reversible switching of Azobenzene isomerization states under UV-Vis illumination makes it very attractive for the manipulation of the matter on the molecular and larger scales. On the molecular level, Azobenzene is used for the mechanical control of chemical and biological processes, examples of which are presented in a review by Merino et al[29]. On larger scales (nm-μm), polymer films based on Azobenzene are widely used to create surface relief gratings[16,30,31]. Liquid crystals containing Azobenzene are used for the creation of light driven devices on macro scales[17,32,33].

In order to manipulate the molecular motion and use it in applications, it is necessary to understand the exact dynamics of the isomerization. Although the isomerization process has been debated for years, no consensus on the isomerization pathways and exact time scales of the relaxation processes has been reached by the time this thesis was written. Several studies suggest that there are two ways for Azobenzene molecule to isomerize from trans to cis state – rotation and inversion[34–37]. Others propose a third pathway called hula-twist, which is essentially a combination of rotation and inversion[13,14,38–40]. According to one of the latest detailed investigation of the transient absorption spectroscopy, hula twist is the most probable pathway for the switching on Azobenzene[14] (Figure 2-1a).

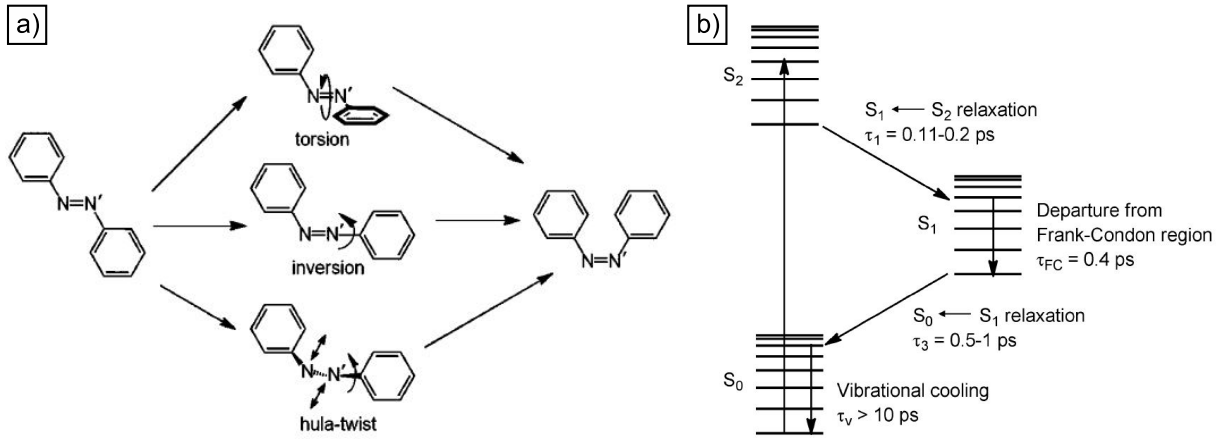

Figure 2-1 a) Schematic of Azobenzene isomerization pathways b) A simplified Jablonski diagram showing the S_0, S_1 and S_2 states of trans Azobenzene. Excitation to the S_2 state is followed by rapid relaxation to the S1 state. Then, departure from the Frank-Condon region and S_0'S_1 relaxation takes place, accompanied by a potential isomerization of the molecule. Finally, vibrational cooling in the S_0 state occurs.

A simplified Jablonski diagram showing the S_0, S_1 and S_2 states of trans Azobenzene (Figure 2-1 b), is discussed in the recent review by H.M Bandara et al[13]. The ground state of Azobenzene is a singlet state S_0. S_1 and S_2 are the first and the second excited states. S_1 state can be reached by the direct excitation of the ground state, or by the relaxation of the S_2 state. The excited states S_1 and S_2 generated by the excitation of trans and cis Azobenzene are different in energy and conformation. Several publications on the transient spectroscopy of trans Azobenzene reported the relaxation times to be 0.11-0.3 for $S_2 \rightarrow S_1$, and 0.5-1.0 ps for $S_1 \rightarrow S_0$, followed by the vibrational cooling for over 10 ps[15,36,41–45]. These relaxations appear to be monomodal, while the direct excitation of the S_1 state result in a monomodal or bimodal relaxation, depending on the solvent and the excitation wavelength[41,43].

Molecules of Azobenzene are capable of switching their isomerization state not only in solutions but also in polymers, where the molecular transformation is sterically hindered[46]. Moreover, some studies of surface relief gratings found the photo induced surface modification due to the Azobenzene isomerization strong enough to break a layer of gold (the internal pressure exceeds 1 GPa)[47,48]. The ability of Azobenzene to undergo reversible switching makes it a good candidate for a soft matter transducer.

2.2. Plasmonics

Plasmonics deals with the interaction between an electromagnetic field and free electrons in metals. Surface plasmon polaritons (SPPs), are electromagnetic waves, which travel along a metal-dielectric or metal-air interface. In nanoparticles, electrons are bound to the lattice by the restoring coulomb forces. This leads to the oscillations of the electrons at the particle surface when an external electromagnetic field is applied. These oscillations are called localized surface plasmon resonances (LSRP). Analytically this phenomenon derives from the dielectric function of gold, as described in the review G.V.Hartland[49], which we summarize here.

Drude model is a simple realistic model for the description of the dielectric function of a metal. For many metals, this model provides reasonable results. However, in the visible and near UV range, for noble metals it doesn't lead to the correct results because of the interband transitions[50]. After taking into account the frequency- dependent damping due to the interband transitions, the dielectric constant is described by the following formula

$$\varepsilon(\omega) = \varepsilon^{ib}(\omega) + 1 - \frac{\omega_p^2}{\omega(\omega + i\gamma)} \tag{2-1}$$

where ε^{ib} is the interband contribution, ω_p is the frequency of the plasma oscillations and γ is the damping constant. For nanoparticles the damping constant is

$$\gamma(l_{eff}) = \gamma_b + \frac{A}{l_{eff}} \tag{2-2}$$

where γ_b is the bulk damping constant, l_{eff} is the effective path length of the electrons before scattering off a surface, and A is a dimensionless parameter, which is usually assumed to be close to unity, and is determined by details of the scattering process[51]. After taking into account that at optical frequencies $\omega \gg \gamma$ into real and imaginary components of the equation (2-1) are the following

$$\varepsilon_r(\omega) = \varepsilon_r^{ib}(\omega) + 1 - \frac{\omega_p^2}{\omega^2} \tag{2-3}$$

$$\varepsilon_i(\omega) = \varepsilon_i^{ib}(\omega) + 1 - \frac{\omega_p^2 \times \gamma(l_{eff})}{\omega^3}. \tag{2-4}$$

Equation (2-3) shows that for nanoparticles the real part of the dielectric constant is essentially the same as for bulk material, while the imaginary part contains damping $\gamma(l_{eff})$ for the electron-surface scattering l_{eff}. Therefore, for metal nanoparticles, small size leads to increased damping of the electron motion by the surface scattering.

The spectra of metal nanoparticles are dominated by the LSPR. The position of the LSPR depends on particles composition, size, shape and their environment. For spherical particles, spectra can be calculated by using Mie theory. This theory requires the dielectric constants of both the particles and their environment. The formulas for the scattering and extinction cross section from Mie theory are the following[52]:

$$\sigma_{sca} = \frac{2\pi R^2}{x^2} \sum_{n=1}^{\infty} (2n+1)\{|a_n|^2 + |b_n|^2\} \tag{2-5}$$

$$\sigma_{ext} = \frac{2\pi R^2}{x^2} \sum_{n=1}^{\infty} (2n+1) Re\,[a_n + b_n] \tag{2-6}$$

Where $x = 2\pi R n_m/\lambda$, n_m is the refractive index of the medium, and R is the radius of the particle. The absorption cross section is given by $\sigma_{abs} = \sigma_{ext} - \sigma_{sca}$. The a_n and b_n factors are given by

$$a_n = \frac{\psi_n'(mx)\psi_n(x) - m\psi_n(mx)\psi_n'(x)}{\psi_n'(mx)\zeta_n(x) - m\psi_n(mx)\zeta_n'(x)} \tag{2-7}$$

$$b_n = \frac{m\psi_n'(mx)\psi_n(x) - \psi_n(mx)\psi_n'(x)}{m\psi_n'(mx)\zeta_n(x) - \psi_n(mx)\zeta_n'(x)} \tag{2-8}$$

where $\psi_n(z) = \sqrt{(\pi z/2)} \times J_{n+\frac{1}{2}}(z)$, $\zeta_n(z) = \sqrt{(\pi z/2)} \times (J_{n+\frac{1}{2}}(z) - iY_{n+\frac{1}{2}}(z))$. J and Y are the Bessel functions of the first and second kind, and $m = n_p/n_m$, where n_p is the refractive index of the particle. The different terms in equations (2-5) and (2-6) correspond to the dipole (n=1), quadrupole (n=2), etc., contributions.

When the particles are much smaller than the wavelength of light, only the dipole contributions in equation (2-5) and (2-6) are important. In this case the extinction is dominated by absorption[53] and the absorption cross-section is given by[52]

$$\sigma_{abs} = 4\pi R^2 x Im\left(\frac{m^2-1}{m^2+2}\right) \tag{2-9}$$

Equation (2-9) can be rewritten if we express the ration between ε (dielectric constants of the particle) and ε_m (dielectric constant of the medium) as $m^2 = \varepsilon/\varepsilon_m$

$$\sigma_{abs} = \frac{18\pi V}{\lambda}\varepsilon_m^{3/2}\frac{\varepsilon_2}{(\varepsilon_1+2\varepsilon_m)^2+\varepsilon_2^2} \tag{2-10}$$

where V is the volume of the particle[52]. Equation (2-10) shows that in the quasi-static limit for spherical nanoparticles the plasmon resonance occurs when $\varepsilon_1 = -2\varepsilon_m$. An extension of the equation (2-10) to ellipsoidal particles was derived by Gans[54]

$$\sigma_{abs} = \frac{2\pi V}{3\lambda}\varepsilon_m^{3/2}\sum_{j=1-3}\frac{(1/P_j^2)\varepsilon_2}{\left(\varepsilon_1+\left(1-P_j\right)\varepsilon_m/P_j\right)^2+\varepsilon_2^2} \tag{2-11}$$

where the depolarization factors P_j for a cylindrical rod are given by

$$P_A = \left(\frac{1-e^2}{e^2}\right)\left\{\frac{1}{e^2}\ln\left(\frac{1+e}{1-e}\right)-1\right\} \tag{2-12}$$

$$P_B = P_C = \frac{1-P_A}{2} \tag{2-13}$$

and $e = \sqrt{(1-(1/AR)^2)}$, where AR is the aspect ratio of the rod (length divided by width). Equations (2-12) and (2-13) predict two localized surface plasmon resonances for rod-shaped particles. Longitudinal resonance corresponds to electrons oscillating along the major axis of the rod and a transverse resonance corresponding to electrons oscillating along the minor axis of the rod. A cartoon depicting the oscillations of the electron cloud for the longitudinal and the transverse resonances is shown in Figure 2-2.

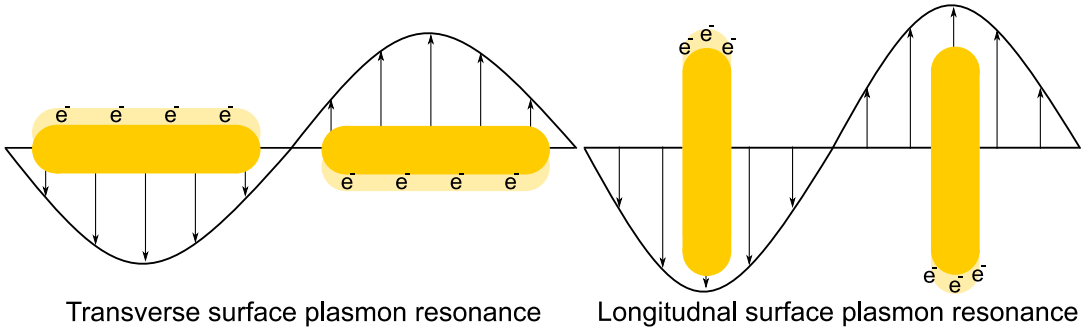

Figure 2-2 A cartoon of the electron displacement in a gold nanorod caused by an external electric field. The resonant oscillation of these electrons is called localized surface plasmon. For rods there are two resonances – one is transverse and the other is longitudinal, depending on the dimension along which electrons are oscillating

When rods are excited, the incoming energy dissipates through electron-electron interaction, coherent vibrations, and heat. Figure 2-3 shows a typical transient signal of GNRs (GNRs type II for the probe wavelength 500nm), in order to illustrate the characteristic time scales in the pump-probe experiments with gold nanoparticles. After the excitation of the free electrons by a femtosecond laser pulse in a metal nanoparticle, three characteristic relaxation processes are observed: a) thermalisation of the electron gas (<1 ps), b) electron-lattice thermalisation (several picoseconds), and c) the particle – surrounding medium energy exchange (several nanoseconds)[55–58].

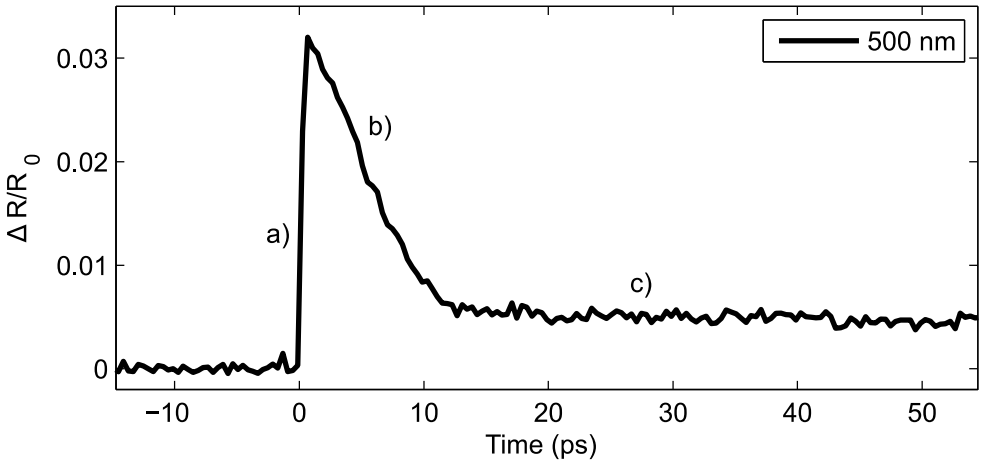

Figure 2-3 Illustrations of the three characteristic processes in excitation of gold. a) Excitation and thermalisation of the electrons to a hot Fermi distribution. b) Transfer of the electrons' energy to the lattice via electron-phonon coupling. c) Lattice relaxation.

The coherent vibrations caused by the excitation are called the extensional and the breathing breathings modes and correspond to the oscillations of the diameter and the length respectively (Figure 2-4). A theoretical and experimental analysis of the vibrational response of nanorods to ultrafast laser induced

heating has been performed by Hu et al[59]. Continuum mechanics has been employed to derive expressions for the breathing and extensional vibrational frequencies of freestanding nanorods. For a cylindrical rod with a length L and radius R, the vibrational frequencies can be expressed in terms of the elastic moduli and dimensions of the nanorods as:

$$\nu_{br}^{(n)} = \frac{\varphi_n c_1^{(s)}}{2\pi R} \tag{2-14}$$

$$\nu_{ext}^{(m)} = \frac{2m+1}{2L}\sqrt{\frac{E}{\rho^{(s)}}} \tag{2-15}$$

where the integer n indicates the radial mode number (for the fundamental breathing mode, $n = 0$), integer m indicates the extension mode number (for the fundamental extension mode $m = 0$), $c_1^{(s)}$ is the longitudinal speed of sound in gold, E is the Yong's modulus along the long particle axis, and $\rho^{(s)}$ is the density of gold. The eigenvalue φ_n for the breathing more of a rod is given by $\varphi_n J_0(\varphi_n) = (1 - 2\sigma)J_1(\varphi_n)/(1-\sigma)$, where σ is the Poisson's ratio.

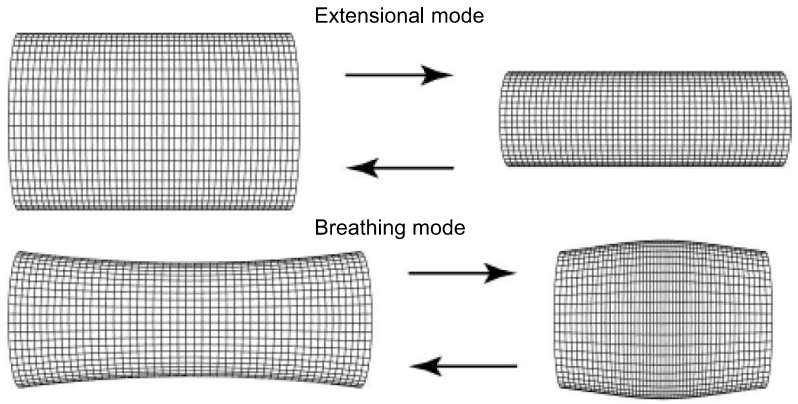

Figure 2-4 A Schematic of the vibrational modes of a cylindrical rod.

2.3. Phononics

A phonon is a quantum of a vibrational motion in which a lattice of atoms or molecules uniformly oscillates at a single frequency. Phonons can be represented as waves and quasiparticles. Such quasiparticles can interact with each other, with light or with other quasiparticles such as plasmons or magnons.

2.3.1. Brillouin scattering

Brillouin scattering is the scattering of light from acoustic phonons. It can also be interpreted as the interaction between light and a change of the refractive index, which can be caused by phonons.

In the presented work Brillouin scattering is discussed in the context of the interaction between an ultrashort light pulse and phonon wave packets (Figure 2-5 a).

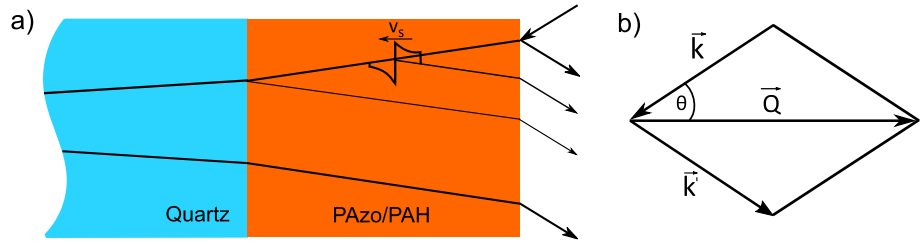

Figure 2-5 a) A schematic of the Brillouin scattering event. The transducer layer excited from the surface generates a strain wave, that propagates towards the substrate. The probe light reflects from the surface and interferes with the probe light reflected from the strain wave. Constructive interference appears for the wavelengths fulfilling the Laue condition. b) Vector diagram of the Laue equation.

In the following I summarize the interpretation of the light scattering from hyper-sound waves, as discussed by Bojahr et al[3] and applied in the presented work. The phonon wave packets can be treated as a moving Bragg grating with lattice constant $d = 2\pi v_s/\omega_s$, where v_s is the sound velocity in the propagating medium and ω_s is the phonons angular frequency. Optical photons are diffracted if they fulfill Bragg's law

$$\lambda_m = 2d_s sin\theta \tag{2-16}$$

where $\lambda_m = \lambda/n(\lambda)$ and $n(\lambda)$ is the refractive index of the propagating medium. In reciprocal space, the scattering of light with a wave vector $\vec{k}$ at a phonon with wave vector $\vec{Q}$ is described by the Laue equation:

$$\vec{Q} = \vec{k}' - \vec{k} \tag{2-17}$$

Figure 2-5 b) shows the corresponding vector diagram. In the direction perpendicular to the surface $|Q| = 2k_{\|}$, where $k_{\|} = k * cos\theta$. Taking into account that $k = (2\pi n(\lambda))/\lambda$, rewriting equation (2-17)

$$Q(\lambda) = \frac{4\pi}{\lambda} n(\lambda) cos\theta. \tag{2-18}$$

This equation expresses the phonon wave vector, in terms of the given angle and the wavelength of the probe light.

When the probe light, reflected from the propagating phonon wave-packet interferes with the light reflected from the surface, it results in a wavelength dependent interference pattern with a period

$$T = \lambda / [2v_s n(\lambda)\, cos(\beta)] \tag{2-19}$$

where β is the internal angle of incidence according to Snell's law. By analyzing the period T for different time delays e.g. for different position of the propagating strain within the investigated medium, one can extract the in-depth information about the refractive index and the sound velocity of the medium.

2.3.2. Linear chain model

For the simulation of the acoustic waves, we use a linear chain model, which was confirmed to be reliable by many publications[3,4,60,61]. A detailed description of the model is described by Herzog et al[62] and the UDKM simulation tool box based on this model is elaborated in the publication by Schick et al[63]. In short the one-dimensional model consist of N mases and springs, along the z-axis (out of plane). Each unit cell of the medium is represented by a masses m_1, m_2, ...m_N, which are connected by springs with a force constant $k_i = m_i v_i^2 / a_i^2$. Here v_i is the longitudinal sound velocity, m_i is the mass and a_i is the out of plane lattice constant of the *i-th* unit cell ($i = 1,2,\dots,N$). This model allows for the simulation of all longitudinal acoustic modes propagating perpendicular to the surface of the sample. Figure 2-6 schematically shows the process of the strain generation inside the transducer (orange circles with mass M_1), and adjacent propagating medium (blue circles with mass M_2). At time $t \to \infty$ the coherent strain has propagated out of the transducers layer and all the masses are located at their new equilibrium position. For mass n the new position defines the strain ε_n^1, which depends on many parameters such as energy deposited into the system, penetration depth, elastic constant etc. ε_n^2 is the strain in the adjacent material.

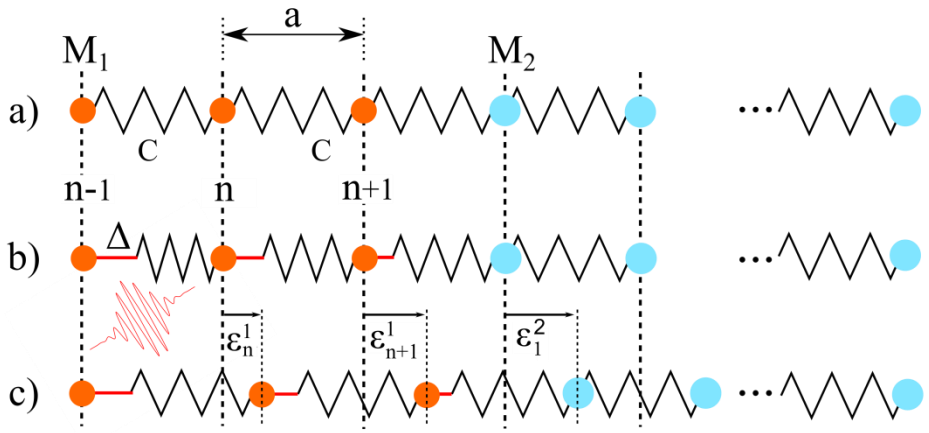

Figure 2-6 A schematic of the linear-chain model. a) For $t < 0$ all masses are at rest. b) At $t = 0$ an excitation stress Δ is induced by a short laser pulse. In the linear-chain schematic, it is represented by incompressible sticks, which lead to an instantaneous compression of the springs. c) New equilibrium position in the excited state.

The linear chain model allows us to simulate the strain profile at certain times after the excitation in different structures. The Fourier transformation of a rectangular bipolar strain pulse results in spectral phonon density with an amplitude of [64]

$$A = \frac{4sin^2(\frac{1}{2}d_T Q')}{Q'} \tag{2-20}$$

where the wave vector Q'

$$Q' = \frac{4\pi \upsilon_s n(\lambda)\cos\beta}{\upsilon_T \lambda} = \frac{\upsilon_s}{\upsilon_T} Q(\lambda) \tag{2-21}$$

The variables d_T and υ_T describe thickness and sound velocity of the transducer. β is the incident angle of light within the medium. Figure 2-7 compares the simulated phonon spectra for two transducers with different thickness. The plot is essentially the Fourier-transform of the strain in an adjacent material. If the spectrum is analyzed for the strain within a transducer, the peak of the phonon amplitude is observed at *k* = 0.

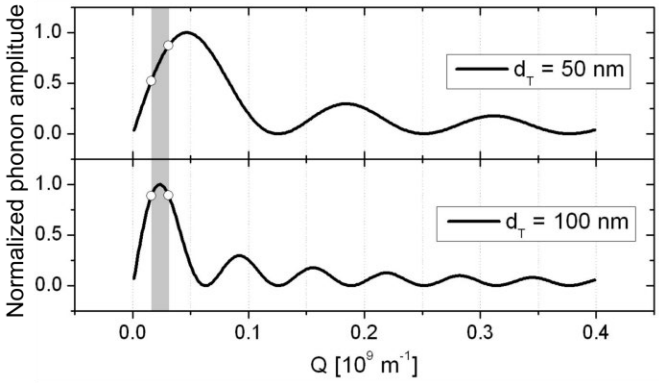

Figure 2-7 Phonon spectra generated in an adjacent material by a transducer of thickness 50 and 100 mn. Grey area marks the optically accessible region of probe wavelength.

3. Experimental methods I: Sample Preparation

3.1. Materials

3.1.1. Polyelectrolytes

For an investigation of the dynamics in polymers, homogeneous films with controlled thickness and smooth interfaces are required. There are several ways to prepare such structures and the Layer – by – Layer deposition technique is one of them. This method is based on the electrostatic attraction between the oppositely charged polyelectrolytes, deposited one after another. For the pump-probe experiments, it is important to choose the polymers according to the absorption spectra e.g. avoid redundant absorption, and chose the photosensitive polyelectrolytes according to the available excitation wavelength. PSS and PAH

polyelectrolytes that do not absorb in the visible light range, were chosen for building spacers and propagating media. PAzo is a polyelectrolyte that contains photosensitive Azobenzene molecules as side groups. Its properties were used to generate strain in the investigated structures.

Poly (ethyleneimine), (PEI) is a cationic polyelectrolyte with a branched structure, purchased as a 50 % wt. aqueous solution. This polymer is used to provide a homogeneous layer and a reliable bonding between the Quartz substrate and the following layered structure of the polyelectrolytes. Poly(sodium 4-styrensulfonate), (PSS) is an anionic polymer, used in transparent spacers. It was also used to cover gold nanorods in order to attach them to substrates. Poly (allylamine hydrochloride) (PAH) is a cationic polymer and was used as a connector between anionic polyelectrolytes. Poly [1-[4-(3-carboxy-4-hydroxyphenylazo) benzenesulfonamido]-1,2-ethanediyl, sodium salt] (PAzo) is a photosensitive anionic polymer used to create photo-responsive structures.

For the preparation of the PAzo solution, NaCl and PAzo must be dissolved in water separately and then mixed together to reach the needed concentrations of polymer (0.1 % wt) and NaCl (0.7 M). To dissolve PAzo in water, the mixture of saline water and the polymer was left constantly stirring for half an hour. To prepare the PSS, PAH and PEI solutions, mixtures of saline water and polymers with the correct proportions were placed in the ultrasonic bath for 15 min (the concentration of the polymers and NaCl are listed in Table 3-1). All polymers are purchased from Sigma-Aldrich (Germany). PSS was dialyzed in order to remove the fragments with only few repetition units. All other polymers were used without further purification. The complete summary of the parameters used for preparing polyelectrolyte solutions is given in Table 3-1.

Table 3-1 Summary of the polyelectrolyte solution properties.

Abbreviation	PEI	PAH	PSS	PAzo
Chemical structure	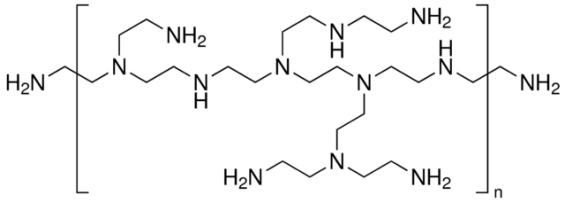	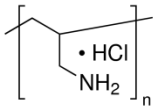	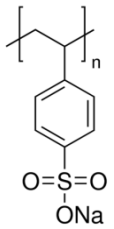	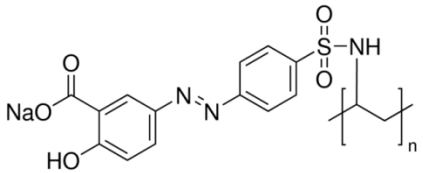
Chemical name	Poly(ethyleneimine)	Poly(allylamine hydrochloride)	Poly(sodium 4 - styrensulfonate)	Poly[1-[4-(3-carboxy-4-hydroxyphenylazo) benzenesulfonamido]-1,2-ethanediyl, sodium salt]
Molecular weight of monomer unit g/mol	527.81	93.56	205.2	369.33
Degree of polymerization	60000	58000	70000	unknown
Surface charge	positive	positive	negative	negative
Concentration of polyelectrolyte (% wt.)	1.0	0.1	0.1	0.1
Concentration of NaCl	None	0.7 M	0.7 M	0.2 M

3.1.2. Other chemicals

To investigate whether the Layer-by-layer preparation technique results in a pronounced alignment of the Azobenzene molecules, I used a different way of the polymer film preparation. 95 % methoxyethanol and 5 % ethyleneglycol solution were mixed with PAzo to reach the final concentration of 250 mg/mL and were left over night. The resulting solution is very viscous and spin coating at 11 000 rpm for 1 min creates a layer of approximately 1 μm.

3.1.3. Gold Nanorods

A selection of different GNRs types, used in the investigated complex structures is required for crosscheck purposes and for the tuning of the spectral features.

Several types of gold nanorods (GNRs) were used in this work. Type I, II, and III differ from each other in diameter, length, and aspect ratio. These particles were synthesized following the growth method by Sau and Murphy[65]. GNRs type IV are very similar to the type II and were purchased from Nanopartz™. GNRs type V were purchased from Sigma Aldrich. All GNR are stabilized by a shell of CTAB surfactant during the synthesis process.

To make the particles attachable to the polyelectrolyte film, they were covered with PSS. For the coverage of 5 ml GNRs, they first were centrifuged for 15 min at 8000 rpm speed. The centrifuged particles were dissolved in 5 ml CTAB (1μM/L). The resulting GNRs solution was then added dropwise to a continuously stirred solution of 5 ml PSS (cwt = 0.2 %, 0.01 M NaCl). In order to remove the free CTAB and nonattached PSS molecules the resulting solution was centrifuged at 8000 rpm for 15 min. The part of the solution which is devoid of particles replaced by purified water and the centrifugation step was repeated. Afterwards the clear solution was removed and the rest (highly concentrated GNRs) was redispersed in 0.2 M NaCl solution. The resulting solution was stored at 4 °C. Table 3-2 summarizes the properties of the used GNRs.

Table 3-2 Summary of the used gold nanorods properties.

Gold nanorods type	Length L (nm)	Diameter D (nm)	Aspect ratio R (D/L)	Position of the transverse plasmon resonance (nm)	Position of the longitudinal plasmon resonance (nm)
I	63.4 ± 8.1	16.3 ± 1.5	3.9 ± 0.6	511	783
II	70.1 ± 7.7	23.4 ± 2.8	3.0 ± 0.3	517	663
III	79.0 ± 9.8	32.7 ± 2.7	2.4 ± 0.3	517	602
IV	71	25	2.8	514	650
V	47	25	1.88	513	600

The data for the rods I, II, and III are taken from the publication[21] by Mitzscherling et al. Parameters for the rods type IV and V are taken from the data provided by the selling companies.

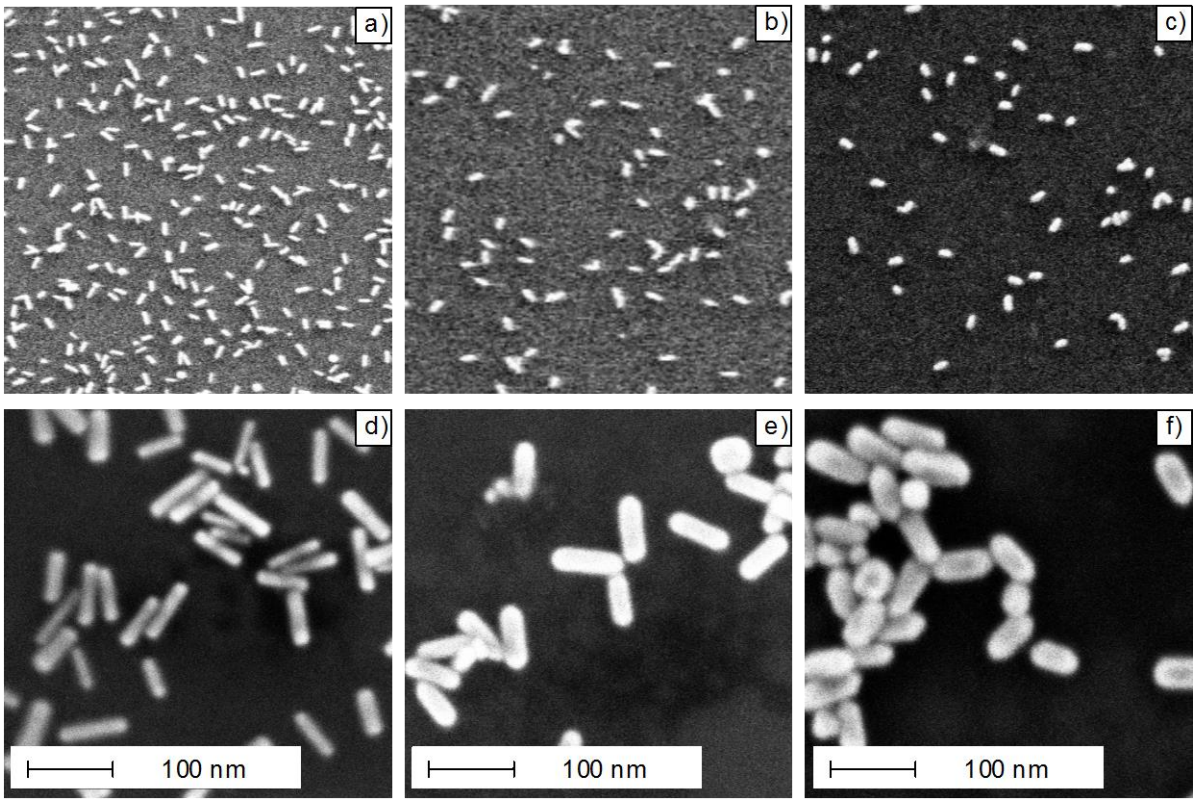

Figure 3-1 SEM pictures of the used gold nanorods. Pictures a)-c) shows the density on the particles type I,II,III on the PAH/PSS surface on 2 μm area. Pictures d)-f) are the same with higher resolution and represent the size distribution.

3.1.4. Substrates

For the correct spectroscopic analysis and to avoid undesirable excitation in the pump-probe experiments, the substrates must be transparent in the visible spectral range. For the deposition of the polyelectrolyte multilayers, the substrate must be hydrophilized by a very strong acid (described below). Fused silica satisfies all the described requirements. Fused silica discs were used in order to provide homogeneous distribution of the solutions during the spin-coating. The discs were purchased from Plano (Germany). They have a thickness of 1.58 mm, and the diameter of 24.5 mm.

For the X-ray measurements, it is necessary to use substrates with crystalline structure. In this work, a 4 μm thick Mica film was chosen as a substrate for these measurements, because Quartz films in the required thickness range were not available.

3.2. Sample preparation

3.2.1. Cleaning

To make the quartz discs suitable for the layer-by-layer deposition, they should be hydrophilized by a "piranha" treatment. The substrates were left for an hour in the mixture of the 3 parts of concentrated sulfuric acid and 1 part of 30 % hydrogen peroxide solution (purchased from Sigma-Aldrich (Germany)). Then they were washed excessively with purified water and dried with a nitrogen flow.

3.2.2. Spin-Assisted Layer-by-Layer Deposition

The spin-assisted layer-by-layer deposition is a reliable and simple way to build a multilayer structure with homogeneous layers[66–70]. This method is based on the electrostatic attraction between oppositely charged polyelectrolytes, which were deposited one after another. To avoid dust contamination, it is important that the substrate is placed in the spin-coating machine straight after the washing procedure and that the first layer is deposited as soon as possible. For the homogeneity of the layers, it is crucially important to place the substrate exactly in the center of the rotation axis and to deposit the solutions exactly in the center of the rotating sample.

To build a layer of polymer, the solution of polymer was deposited dropwise onto the continuously rotating substrate. After the surface has been homogeneously covered with the polymer, the sample must be thoroughly washed with purified water almost immediately (3-5 seconds wait) to wash the non-attached polyelectrolytes away and the left over NaCl. If the washing step is delayed then the NaCl may crystalize while the surface is drying, which will leads to inhomogeneity of the next layers. After the washing step, the sample should be dried until no water drops are left on the surface. The steps are then repeated, with the oppositely charged polyelectrolyte. The entire procedure of building the layered structure is performed with the sample continuously rotating at 3000 rpm. Figure 3-2 represents the process of building a structure by spin coating. The resulting thickness of one double layer (dl) of PSS/PAH is ~2,5 nm[20]. For PAzo/PAH the thickness of one double layer is ~4.7 nm, as has been determined by AFM measurements. When films of dozens of double layers are constructed, the total thickness deviation is within 10 % of the expected thickness.

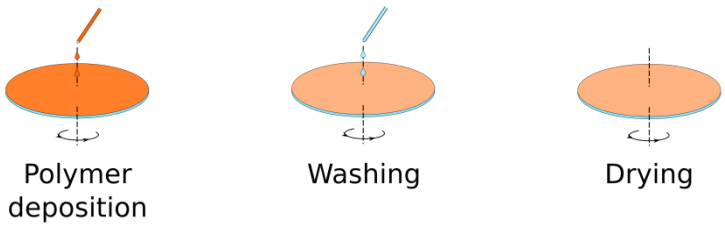

Figure 3-2. A schematic of the spin-assisted layer-by-layer deposition of polyelectrolytes.

During the work on this thesis I have discovered that for the construction of relatively thick films (hundreds of nanometers) the concentration of NaCl in PSS and PAH and should be decreased to 0.7 M, relative to 1M used in previous experiments by our group. The decrease of the NaCl concentration leads to the reduction of inhomogeneities, caused by the crystallized salt. This observation is confirmed by the publication by Lvov et al[71]. It is reported that the concentration of NaCl in PSS/PAH films which is higher than 0.8 M leads to an increase of the layers roughness.

3.2.3. Gold Nanoparticle deposition

PSS coated gold nanorods can be deposited onto a substrate with a positively charged surface, e.g a PAH layer. To do so, the substrate surface was covered completely with a GNRs solution and left for 1 hour. The samples should be stored in a box to avoid drying. After 1 hour, the GNR solution was washed away with purified water. When GNR are deposited as the first active layer of the sample structure, they are deposited onto 4 or 8 double layers of PSS/PAH (~10-20nm).

3.3. Investigated structures

Table 3-3 List of the investigated structures.

Sample name	Substrate	Structure
24	Quartz	4dl PSS/PAH - GNR type III + (2 dl PSS/PAH)*5 + 10 dl PSS/PAH
17	Quartz	60 dl + 30 dl + 30 dl + 30 dl + 30 dl + 50 dl PAzo/PAH
35	Quartz	120 dl PAzo/PAH
OD	Quartz	2412 nm film, prepared by the «One drop» method
M	Mica	880 nm PAzo/PAH
26	Quartz	116 dl PSS/PAH - (GNR type III - 8 dl PSS/PAH)*4 - 104 dl PSS/PAH - 30 dl PAzo/PAH
15	Quartz	8 dl PSS/PAH – GNR type II + 60 dl PAzo/PAH
40	Quartz	90 dl PAzo/PAH – (GNR type III – 8 dl PSS/PAH)*8
42	Quartz	90 dl PAzo/PAH – (GNR type III – 16 dl PSS/PA)*2
49	Quartz	120 dl PAzo/PAH – 70 dl PSS/PAH – GNR V
22	Quartz	120 dl PAzo/PAH – 30 dl PSS/PAH – GNR II
52	Quartz	180 dl PAzo/PAH – 100 dl PSS/PAH – GNR IV
45	Quartz	90 dl PAzo/PAH – (GNR III – 15 dl PAzo/PAH)*3 – GNR III – 60 dl PAzo/PAH).

Double layer – dl. 1dl PSS/PAH = 2.5 nm. 1dl PAzo/PAH = 4.7 nm. «-» represents that the following layer is deposited on the top of the previous. «+» represents that the following layer is deposited on the top of the previous and the transient dynamics of the sample has been measured in between.

4. Experimental methods II: Sample Characterization

4.1. UV-VIS Spectroscopy

Static UV-Vis spectroscopy was used to define the position of various spectral features such as absorption bands, plasmon resonances, or thin film interference patterns. For the pump-probe measurements, static spectra were used as references.

Static reflection (R) and transmission (T) spectra were measured with the UV-VIS-NIR spectrometer (VIRIAN CARY 5000), with an integrating sphere (Ulbricht sphere), schematically shown in Figure 4-1. This device allows the collection of the specular and diffuse contributions of the reflected and the transmitted light. The absorption spectra were calculated as A = 1 – T – R. It is noted that the absorption mode of most spectrometers is not applicable for exact absorption measurements, since scattering and interference effects in thin films are not considered.

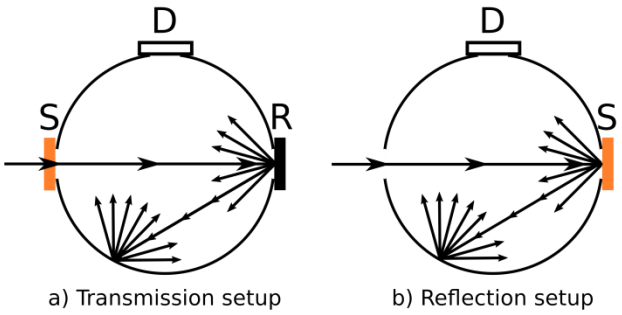

Figure 4-1. A schematic representation of an integrating sphere. In a) the sample (S) is placed on the transmission port. Transmitted light is scattered on a diffuse reflector (R) and collected by the detector (D). For reflection measurements, the setup in b) is used. The sample placed on the reflection port.

4.2. Spectroscopic Ellipsometry

For the interpretation of the pump-probe experiments, it is important to have a precise measurement of the thickness and refractive index of the investigated films. The measurements were performed using a spectroscopic ellipsometer (Sentech). The incident, linearly polarized beam, is reflected from the sample under an angle of typically 60 degrees. After the reflection from the sample, the beam goes through a second polarizer, which is oriented perpendicular to the first one. The reflection from an investigated thin film leads to an elliptical polarization due to the interference of multiple reflections from the interfaces (film/substrate, film/air) and propagation in the medium. Equation (4-1) determines the relation between Ψ (the intensity ratio of p- and s-polarized light), Δ (the phase shift between p- and s-polarization) and the ratio of the measured reflection $R_{\parallel}$ and $R_{\perp}$

$$\frac{R_{\parallel}}{R_{\perp}} = \tan\Psi * \exp(i\Delta) \tag{4-1}$$

To extract the layer's thickness and the refractive index, a model of optical properties of the film has to be built. Ψ and Δ are calculated using Fresnel formulas and equation (4-1).

4.3. Pump-probe spectroscopy

Time resolved techniques are very helpful for investigating the internal structure and dynamics in complex composite materials. In this chapter, the information about the pump-probe setup and its components is presented.

The pump - probe technique The pump-probe technique allow us to perform time resolved measurements with short light pulses. By changing the delay time between pump and probe pulses arrival at the sample, one can observe the dynamics of the investigated system at different time delays after the sample has been excited. To perform such an experiment the pump and probe beams must overlap in space and in time. The time difference between the pump and probe pulses, is controlled by a delay stage from Newport, which moves mirrors to change the path length of the pump pulse.

Ti:Sapphire Laser System All-optical time-resolved measurements were performed with a commercial regenerative femtosecond laser system from Spectra Physics. This system contains three parts. The oscillator (MaiTai) provides ultrashort laser pulses with high repetition rate. These pulses are amplified by the amplifier (Spitfire Pro), which is pumped by a high-power diode laser (Empower). A Ti:Sapphire crystal is used as the active medium in the oscillator and the amplifier. The central wavelength of the amplifier was set to 795 nm and the repetition rate was 5 kHz. The pulse length was ~ 120 fs and the energy of a pulse was 340μJ. About 20 % of the 1.5 Watt of the p - polarized output was used for the described setup and then split between the pump and probe beams.

Frequency Doubling In order to generate pump beam with a wavelength within the absorption band of Azobenzene, the fundamental wavelength of 795 nm has to be frequency doubled. This effect was achieved by focusing the beam into a 1 mm thick nonlinear birefringent crystal β - barium borate (BBO)[72]. In order to use the generated second harmonic, one has to remove the fundamental 795 nm by using a BG-38 filter. The polarization of the resulting second harmonic is perpendicular to the original one.

White Light Generation To generate white light for the probe pulse, I used the supercontinuum generation effect[73–75]. This is a nonlinear effect that is mainly driven by self-phase modulation (SPM). During the propagation, an ultrashort pulse of light induces a change of the medium's refractive index, due to the optical Kerr effect. This refractive index variation will cause a phase shift in the pulse, which will lead to a change in the frequency spectrum of the pulse. Such an effect can appear in many solid materials and gases. In this setup, a Sapphire plate was used as a medium for the white light generation.

Experimental Setup Time resolved optical spectroscopy measurements were performed with the optical setup presented in Figure 4-2**.** A 20 % fraction of 795 beam, coming out from the amplifier goes to a beam splitter, where it is separated into the pump and the probe pulses. Most of the power goes to the pump beam, which is directed over the delay stage. The delay stage moves the mirrors for the pump beam and therefore shortens or elongates the optical path of the pump relative to the probe beam. After the delay stage, the beam goes through chopper. Synchronization of the chopper frequency to the pulse repetition rate allows distinguishing spectra of pumped and unpumped sample. After the chopper, the beam is shaped by lenses and directed to the sample though the BBO. The probe beam is directed though the white light generation setup, followed by a Calflex X filter. Both beams are focused onto the sample surface. The reflected and the transmitted probe beams are simultaneously detected by a two-channel fiber spectrometer from Avantes.

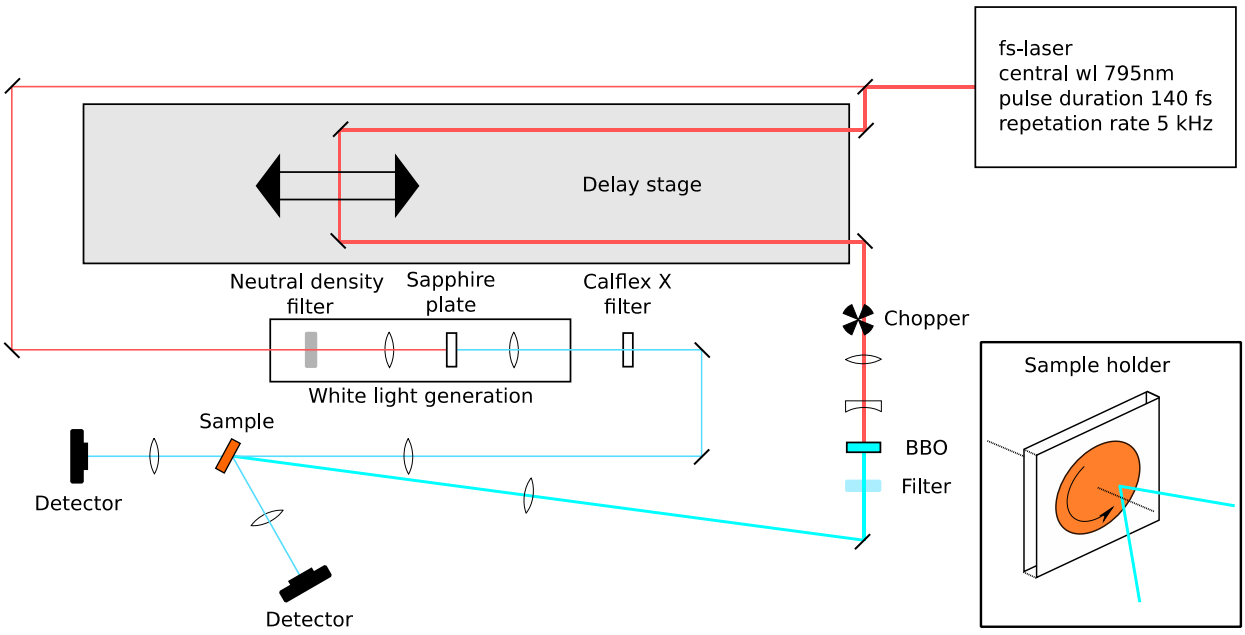

Figure 4-2 A schematic of the experimental setup for the pump-probe spectroscopy. The inset represents the sample holder.

In order to increase signal-to-noise ratio of the recorded data, each data set is an average of several (5-20) loops, where each loop is a set of spectra recorded for different time delays.

For Azobenzene containing samples it is important to take into account the modifications of the polyelectrolytes under the excitation, especially with a high fluence. Due to repetitive switching and heating, the surface and thickness of the film will be modified with time. To make the measurements consistent, the Azobenzene containing samples were continuously rotated so that each spot is illuminated only for one pump-probe event over the cycle.

4.4. Time resolved X-ray Diffraction

In order to calibrate the strain induced by the investigated transducer, we used the time resolved X-ray diffraction. These experiments were performed by using femtosecond X-ray pulses, to track the dynamics in the crystalline material (Mica). As an X-ray source, we used a laser driven plasma X-ray source.

A detailed description of the laser driven plasma source used for the ultrafast X-ray diffraction can be found in the publication by Schick et al[76,77]. In summary: a high energy pulsed laser beam is focused onto a continuously refreshing copper tape, and by that generates X-ray pulses. The plasma X-ray source provides a temporal resolution below 200 fs at an X-ray photon energy of 8.047 keV (Cu Kα).

5. Gold nanorods. Static and transient spectroscopy

One of the main results presented in this thesis is the response of GNRs to the propagating hyper-sound waves inside relatively thick multilayer samples. Such complex structures, containing Gold nanorods and photosensitive polymers, were investigated with static and transient spectroscopy. In order to distinguish various superimposed spectral features, I have investigated each component of the complex structures separately.

In this chapter, static transmission, reflection, and absorption spectra of GNRs are presented, discussed, and compared to the transient measurements. A set of transient measurements performed under the different pump pulse fluences is presented.

5.1. Transient response of GNRs in comparison to the static spectra.

The absorption spectra of GNRs directly markers the eigen frequencies of the electrons oscillating within the rods e.g. plasmon resonances (see chapter 2.2 for more detailed elaboration). For the complex structures, with relatively thick layers of polymers, it is impossible to use static reflection to define the position of GNRs plasmon resonances as the transmission spectra are dominated by the absorption band of Azobenzene. Therefore, only absorption can be used as a reference for the complex structures investigated in this thesis. This chapter qualitatively identifies the correlation between the static absorption, reflection, transmission and the transient spectroscopy of GNRs.

Sample 24 is a layer of GNR type II deposited on 10 nm PSS/PAH buffer on a Quartz substrate as described in 3.2.3. The static spectra of reflection, transmission, and absorption are presented in Figure 5-1 a)-c). All the spectra clearly show two plasmon resonances: the transverse and the longitudinal. The Positions of these resonances are defined by the GNRs aspect ratio and by the dielectric properties of the surrounding medium. The absorption of the transverse resonance (PR_T) for the particle of type II, used in this sample, appears around 530 nm. The position of the longitudinal resonance (PR_L) in the absorption spectrum is around 640 nm. Two vertical lines drawn on the top of all three spectra indicate the positions

of PR_T and PR_L in the static absorption spectrum. It is visible that the minimum or the maximum related to the position of the transverse plasmon resonance appears at the same wavelength in all three spectra, while the longitudinal plasmon resonance is slightly shifted in the transmission spectrum and even more so in the reflection spectrum in respect to the absorption spectrum. The longitudinal mode of the plasmon resonance in gold nanorods is very sensitive to changes of the dielectric function of both the surrounding and particle itself. By tracking the dynamics of the PR_L under the laser excitation, one can study the inner processes of the investigated complex system.

Figure 5-1 d) and e) shows the relative change of the transient reflection (RCTR) and transmission (RCTT) at certain times after the excitation. Relative changes of the transient spectra are complex data and it is sometimes difficult to assign a direct connection between the positions of the features appearing in these spectra to the static ones.

If we assume for example an arbitrary static spectrum containing a peak and this peak would transiently broaden, change in intensity or shift – all these changes will result in essentially the same features in intensity modulations of the transient spectra leading to the appearance of minima and maxima in the spectra of relative changes. The final spectrum of the relative changes would depend on what exactly is happening (width change, intensity change or shift) and what is the sign of the feature (width increase or decrease etc.). In the presented work, we will not discuss in detail the connection between the positions of the plasmon resonances related features in static spectra versus transient relative changes.

Figure 5-1 b) shows the static reflection spectrum overlaid with the relative changes of the transient reflection for the same sample (sample 24). Figure 5-1 e) shows the same data sets for transmission spectra. In this experiment, the fluence of the 398nm on the sample was ≈ 1 mJ. The excitation of the GNRs leads to the negative signal in RCTR in the area corresponding to the left shoulder of the longitudinal peak in the static reflection spectrum. This negative signal extends to smaller wavelength up to the peak position of the transverse resonance peak. In the other regions (left shoulder of PR_T and right shoulder of PR_L) it appears as a positive signal on the transient reflection spectrum. In the transmission, the signs of the signal are opposite to the signs in the transient reflection spectra. However, the change in $\Delta R/R$ doesn't fully account for the change in $\Delta T/T = -\Delta R/R - \Delta A/A$, so there must be some modification of the absorption ΔA or scattering.

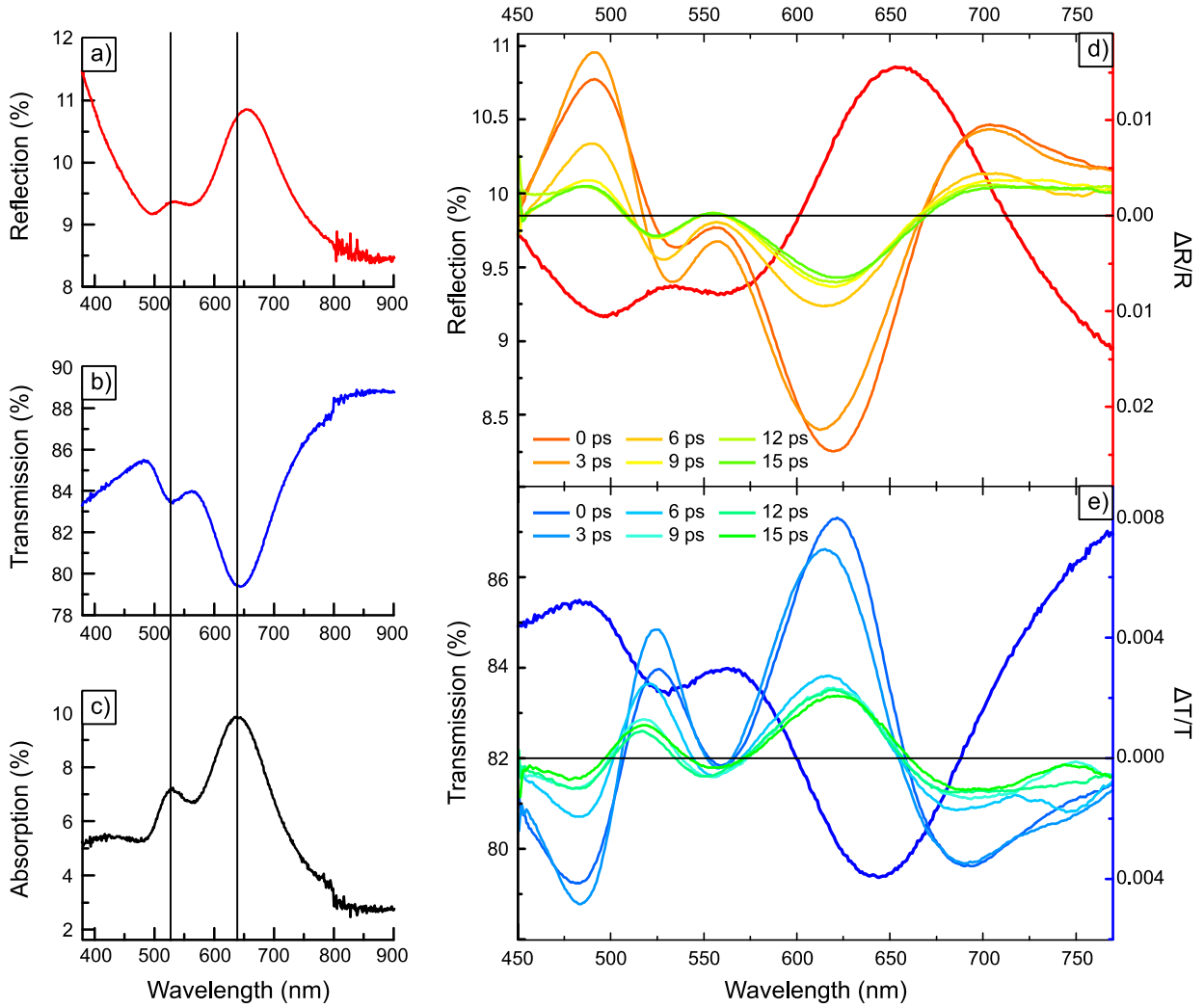

Figure 5-1. For sample 24 of GNRs type III,deposited on a small buffer of PSS/PAH (10 nm) on a Quartz substrate. a),b) – measured static spectra of reflection (R) and transmission (T). c) Static absorption spectrum, calculated as A = 1 – T – R. of sample 24. d) The relative change of the transient reflection for different time delays, overplayed with the static spectrum of reflection. e) The relative change of the transient transmission for different time delays, overplayed with the static spectrum of transmission. 398 nm pump pulse, fluence - 1 mJ.

5.2. Transient response of GNRs to the excitation with different fluences.

In the presented work, different experiments were performed with different fluence of the excitation pulse. In the complex structures, where GNRs are embedded or covered with an absorbing polymer, the fluence absorbed by GNRs will be different, comparing to the uncovered case. Part of the excitation pulse is then

absorbed by the covering layer, therefore the effective fluence seen by GNRs is different. To understand what is the influence of the different fluences to the transient response of GNRs, I performed an examination of the GNR's transient response depending on the excitation fluence of the 398nm pump pulse. Transient data for the relative change of the transmission and reflection of sample 24 (GNRs type III on 10nm PSS/PAH on Quartz) are presented in Figure 5-2. This figure represents the typical response of the GNRs type II, for which the position of the transverse plasmon resonance is around 530 nm and the position of the longitudinal plasmon resonance is around 640 nm. For the other types, the positions of the minima and maxima of the ΔT/T and ΔR/R will be different, depending on the aspect ratio of the GNRs. Typically transient spectra of GNRs measured during the work on this project would not show the expected breathing mode of longitudinal plasmon resonance (see chapter 2.2). In Figure 5-2 b) this mode can be seen as a modulation in ΔR/R spectrum at wavelengths 600-650 nm. The spectral minimum shifts slightly to higher wavelength at ~ 80 ps and then shifts back to the initial position at ~ 140 ps. The weakness of this feature in these experiments is explained by the noticeable size distribution of the excited GNRs that were probed by the ⌀ 120 μm probe pulse.

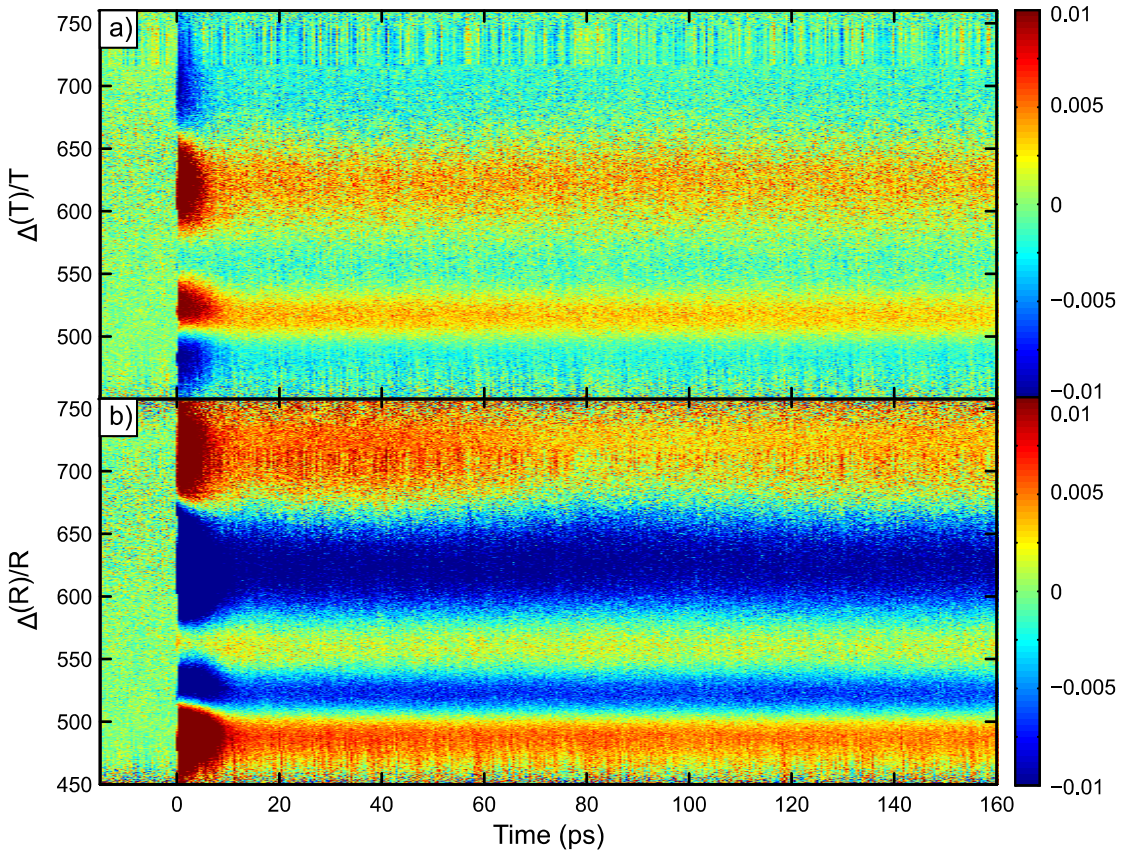

Figure 5-2 The relative change of the transient a) transmission, b) reflection for sample 24 (GNRs type III on 10nm PSS/PAH on Quartz). Excitation wavelength - 398nm, fluence - 1.2 mJ.

Figure 5-3 shows cuts at 5 ps of ΔR/R for the same sample excited with the different fluences (from 0.5 to 1.2 mJ). Higher fluence leads to the higher amplitudes of the relative changes in the spectra and to a slight

shift of the spectral features towards higher wavelength. However, the difference between the positions of the features is not crucial for the data interpretation.

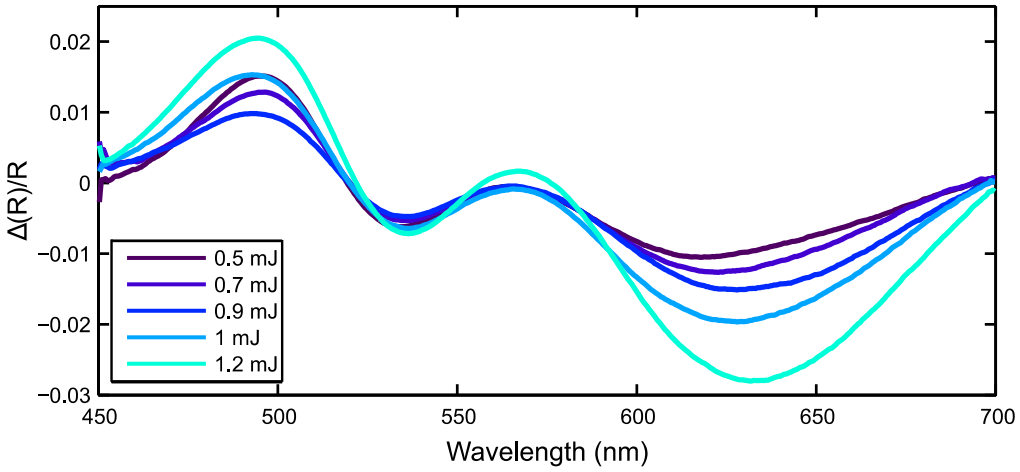

Figure 5-3 Cuts at 5 ps of the ΔR/R measurements with different fluences for sample 24 (GNRs type III on 10nm PSS/PAH on Quartz).

5.3. Transient response versus PSS/PAH coverage

It is known from the literature that the position of the longitudinal plasmon of GNRs is very sensitive to the surrounding medium[21,78–80]. This effect is used in many applications for sensing in chemistry[22,81–83] and biology[27]. However, the transient response to the excitation of the covered GNRs is not well studied. In order to have a better understanding of the complex sample architectures investigated studied in this work, I performed a series of pump-probe experiments for GNRs covered with different amounts of PSS/PAH. The results are presented in Figure 5-4, which shows the static and transient spectra of sample 24 (GNRs type III on 10nm PSS/PAH on Quartz) covered with 2, 4, 6, 8, 10 and 20 dl of PSS/PAH. Static spectra of reflection, transmission, and absorption are presented as the reference spectra in the Figure 5-4 b), c), e), d). The absorption spectrum shows an increase of the plasmon resonance intensity and a shift to higher wavelength for thicker covering film. This effect is connected to the changes in the average dielectric function of the surrounding medium, which then affects the positions and intensity of GNRs plasmon resonances. In a similar static experiment published by Kiel et al.[20] gold nanopsheres were covered by PSS/PAH double layers and the shift of the corresponding plasmon resonance was observed. After a certain coverage thickness, the shift saturates. The shift of the plasmon resonance was observed to be up to~30 nm depending on the particle size. In a recent publication by Mitzscherling et al.[21] where a similar investigation was performed for gold nanorods, the shift of the transverse plasmon resonance was found to be 15 nm until the saturation and up to 100 nm for the longitudinal plasmon resonance.

The key measurement presented in this subchapter is the relative change of the transient reflection, Figure 5-4 a). It shows that, depending on the coverage, the signal in ΔR/R may appear as positive or negative

signal. For instance, the transient signal of ΔR/R at 625 nm appears to be negative for the uncovered sample, while after the deposition of 20 dl of PSS/PAH the signal at this wavelength becomes positive, due to the strong shift of reflection pattern to higher wavelength.

Data for the ΔT/T signal (Figure 5-4 d), show a noticeable shift of the plasmon resonance- related spectral features, as well.

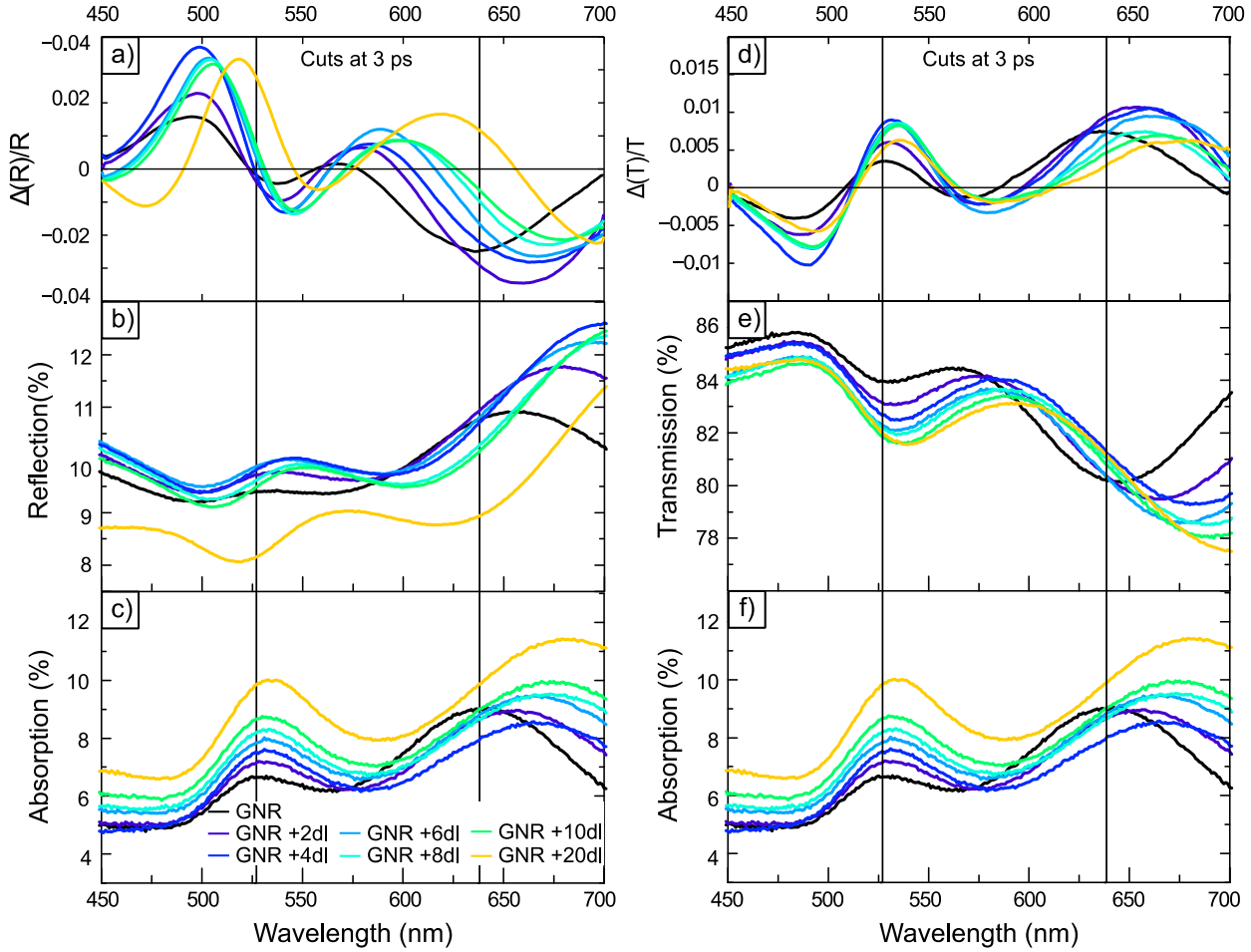

Figure 5-4 Sample 24 (GNRs type III on 10nm PSS/PAH on Quartz) was covered with PSS/PAH and measured after 2, 4, 6, 8,10 and 20 dl of polymers. Panel a) and b) show the transient and static reflection spectra, while c) presents the static absorption spectra to indicate the resonance position (vertical black lines). Panel d) and e) show the transient and static transmission, while f) reproduces the absorption data from panel c.

6. Azobenzene containing polymer as a transducer

Soft matter transducers are beneficial, in comparison with solids, for triggering strain into adjacent soft materials. The main advantage is the similarity of the acoustic impedances between transducer and the investigated object. The ease of the deposition process is another advantage. Besides being cheaper (costs of the equipment and material), in comparison to metal film deposition, polymer films can be easily removed by solvents. From a spectroscopic point of view, specifically the Azobenzene-based transducer is transparent to visible light, which is sometimes very beneficial for broad-band pump-probe spectroscopy.

One of the goals of the presented research project was to create and investigate a soft matter transducer. Some work in this direction has been performed by other members of the group (A. von Reppert, M. Sander, S. Mitzscherling) and is published, among other results, in their theses.[84–86] My work extends the knowledge of the photosensitive polyelectrolytes as transducers, investigating the changes of the optical and mechanical properties appearing within the transducer during the strain generation, and exploring more materials for the strain propagation.

Azobenzene molecules are known for their reversible photo-isomerization[87–89], which can be induced by illumination at certain wavelength ranges. Azobenzene - containing polyelectrolytes are chosen in this work for building the soft matter transducer; however, a number of other photoactive compounds are available. Azobenzene - containing transducers were prepared using the two methods, described in 3.1.2 and 3.2.2. The first „one drop“ (OD) method, provides a single, relatively thick layer of the polymer. In this method, the resulting thickness cannot be controlled precisely. Nevertheless, by varying the concentration of ethyleneglycol and the rotation speed of the spin coater during the deposition, one can change the average thickness of the resulting film. The second method uses the layer-by-layer (LBL) technique[66] and provides a precise control over the thickness of the structure and very smooth surfaces. It is yet unclear how important the density of the molecules is for the switching and whether the switching is crucial for the strain generation.

The comparison of these two different kinds of structures (OD and LBL) is interesting due to the different environments of the Azobenzene molecules, which allow different degree of steric hindrance for Azobenzene molecules. The comparison is also important to identify if the LBL structures consist of aligned Azobenzene molecules and whether or not that plays a role in the strain generation.

The photo induced dynamics of Azobenzene has attracted a lot of attention and has been studied not only on the molecular level but also as a driving mechanism for dynamics in polymer films[17,19,47,90–92] and liquid crystals[33,93–95]. Azobenzene containing polymer films have been studied as photosensitive materials in order to imprint gratings [16,47,96], manipulate free standing films[33,94,95], investigate their reversible expansion and refractive index change[18,19,97]. As a material for the generation of hyper-sound waves it was first studied by M. Sander (diploma thesis)[85], A. von Reppert (Bachelor thesis)[84], S. Mitzscherling (PhD thesis)[86]. In those studies thin layers of LBL-made PAzo/PAH on quartz were excited, and the strain in

Quartz had been the major object of interest. In this chapter, strain inside the Azobenzene containing films is discussed, in particular its effect on the refractive index change on the picosecond time scale.

6.1. Transmission data analysis

Transmission or absorption spectra are very informative for the analysis of internal processes such as molecular switching, relaxation, heat diffusion and others. In this chapter, static and transient transmission data of Azobenzene containing polymers are presented and discussed.

Typical static transmission and absorption spectra of LBL and OD films on quartz are presented in Figure 6-1. The thicknesses of the measured films are 60, 282, 423, 564, 705 nm (sample 17) for the LBL films and 2414 nm for the OD film. Spectra of the 60 nm film show clearly the position of the trans - Azobenzene absorption band, which is centered around 360 nm. Depending on the exact molecular structure of the Azobenzene containing molecule and the surrounding medium the position of this band may vary within[14] ±20 nm. As the film thickness increases, the absorption band saturates and extends to higher wavelengths up to 550 nm. For thicker films, it is also possible to distinguish oscillations, which are especially pronounced in transmission for wavelength > 550 nm. This effect of a pronounced interference in the reflected light is discussed in detail in chapter 6.2.

Extracting the percent of the transmitted light at 400 nm, for different film thickness for the static transmission spectra (Figure 6-1), I have built the graph, which allows for the definition of the penetration depth for the linear regime (Figure 6-2, blue squares). When the sample is illuminated with high fluence laser pulses, the linear regime of absorption is no longer valid. The data points for the nonlinear transmission regime are presented on the same plot (Figure 6-2, black circles). From this plot we estimate the penetration depth of the pump pulse in the pump-probe measurements to be ~600 nm.

Figure 6-3 a) shows the broad-band spectrum of the relative change of the transient transmission ($\Delta T/T$) of 1081 nm thick LBL PAzo/PAH (sample 17). On this graph, one can see the negative signal $\Delta T/T$ of throughout the entire spectrum for the early times, which then decays with a wavelength dependent time constant. The intensity of the negative signal, for the early times, also shows wavelength dependence. The spectral structure of the negative signal band can be seen in Figure 6-3 c). In Figure 6-3 a) the very rapid response is observed over a very broad spectral range from 450 nm (or even shorter) up to 750 nm.

Figure 6-3 b) shows the wavelength dependent decay of the negative signal for different wavelengths. In the most recent and complete study of the ultrafast broad band transient absorption of Azobenzene [14] M. Quick et al. presented a careful analysis of the different exited states of Trans and Cis Azobenzene. In this study, as well as in many earlier time resolved experiments[36,37,98], the following characteristic times were observed: 0.3, 3 and 16 ps for the trans-to-cis path upon $n\pi^*$ excitation. The 0.3 ps time is assigned to the relaxation of the population created at the Franck-Condon state to a local minimum (Figure 2-1). 3 ps is the time assigned to the relaxation to the intermediate state which then relaxes to the ground state within

16 ps. The exact times depend on the structure of the molecule and its surrounding medium. In the data presented in Figure 6-3, the first time scales of 0.3 is not resolved, however the decays of around 3 and 16 ps can be observed.

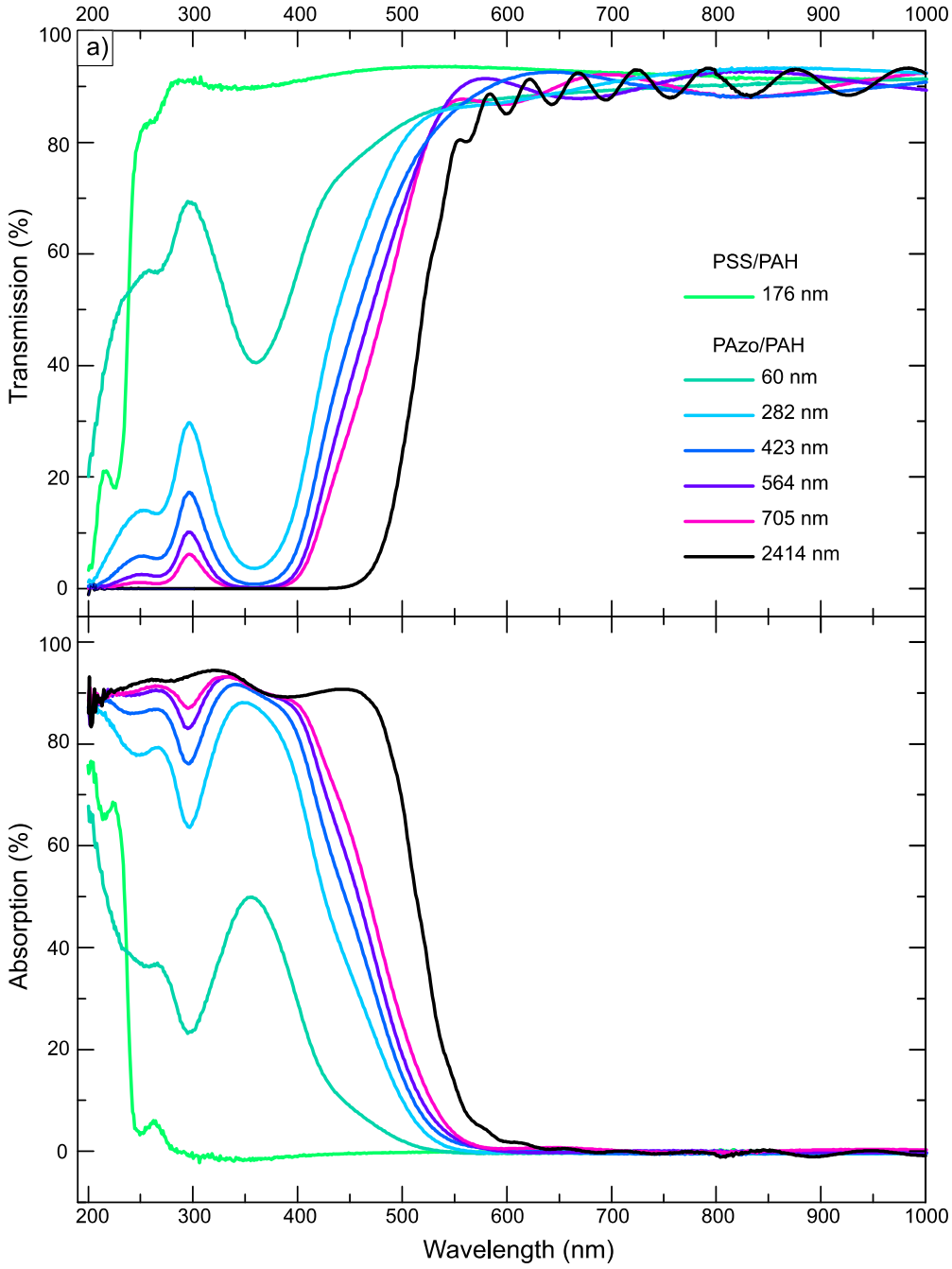

Figure 6-1 Static transmission and absorption spectra of PSS/PAH film and of the Azobenzene – containing films: Layer-by layer films of the thickness 60, 282, 423, 564, 705 nm (sample 17), and a 2414nm thick layer made by the «one drop» technique. Transmission spectra measured on a spectrometer with an Ulbricht sphere. Absorption spectra are calculated as A = 1 – T – R.

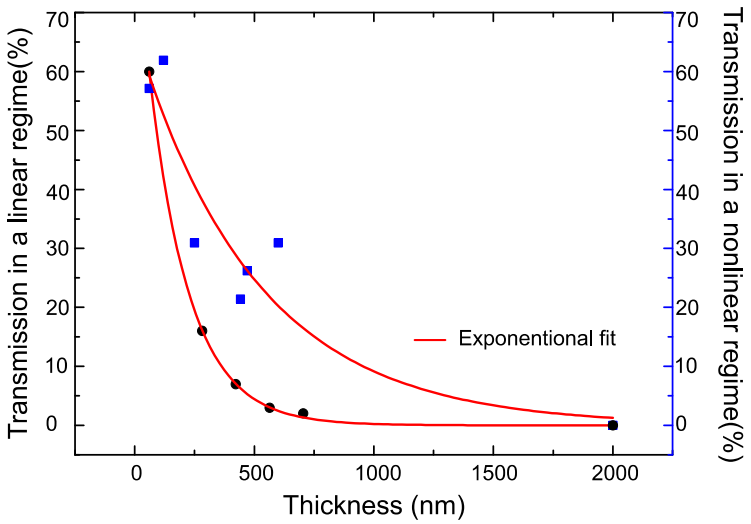

Figure 6-2 Transmission at 400 nm in linear (black circles) and nonlinear (blue squares) regimes.

The data set of the relative change of the transient transmission for the OD sample is presented in Figure 6-4. Similar to the data set for the LBL sample, the panel a) shows the broad-band spectrum of the relative change of the transient transmission (ΔT/T), b) is ΔT/T for certain wavelengths of the probe pulse and c) shows the broad-band ΔT/T spectra at certain time delays. One can see that the transmitted light does not extend beyond 470 nm for this sample. This is due the strong absorption extending up to 550nm (Figure 6-1). Another noticeable difference from the previous sample are oscillations in the wavelength region 550-700 nm. These oscillations are a characteristic of the thin film interference effect, which can be quantitatively evaluated from the static and the transient reflection spectra (chapter 6.2.1 and 6.2.2). These oscillations are present in the previous data set as well, but have a larger period and are less pronounced.

Spectra of both LBL and OD samples show the strongest negative change of the transmission at 490nm. Even though this signal decays significantly on short time scales (~20ps), it does not recover completely. In fact, the negative change in ΔT/T extends as long as 3.5 ns (Figure 6-5), which is the time limit of the setup. On the other hand, we know that the process is reversible since we performed the experiment at the 5 kHz pulse rate of the laser system. This implies that the induced modifications relax within 200 μs.

The negative response in the relative change of the transient transmission can be caused by several effects. First of all it corresponds to the excited state absorption of the Azobenzene molecule. Additional transient absorption might present during the relaxation to the ground state or the isomerized ground state. As mentioned above these events are on the time scales of several picoseconds, up to 16ps. Slower times scales of the change in transmission can be attributed to the heat flow, film expansion, refractive index change and secondary chemical products.

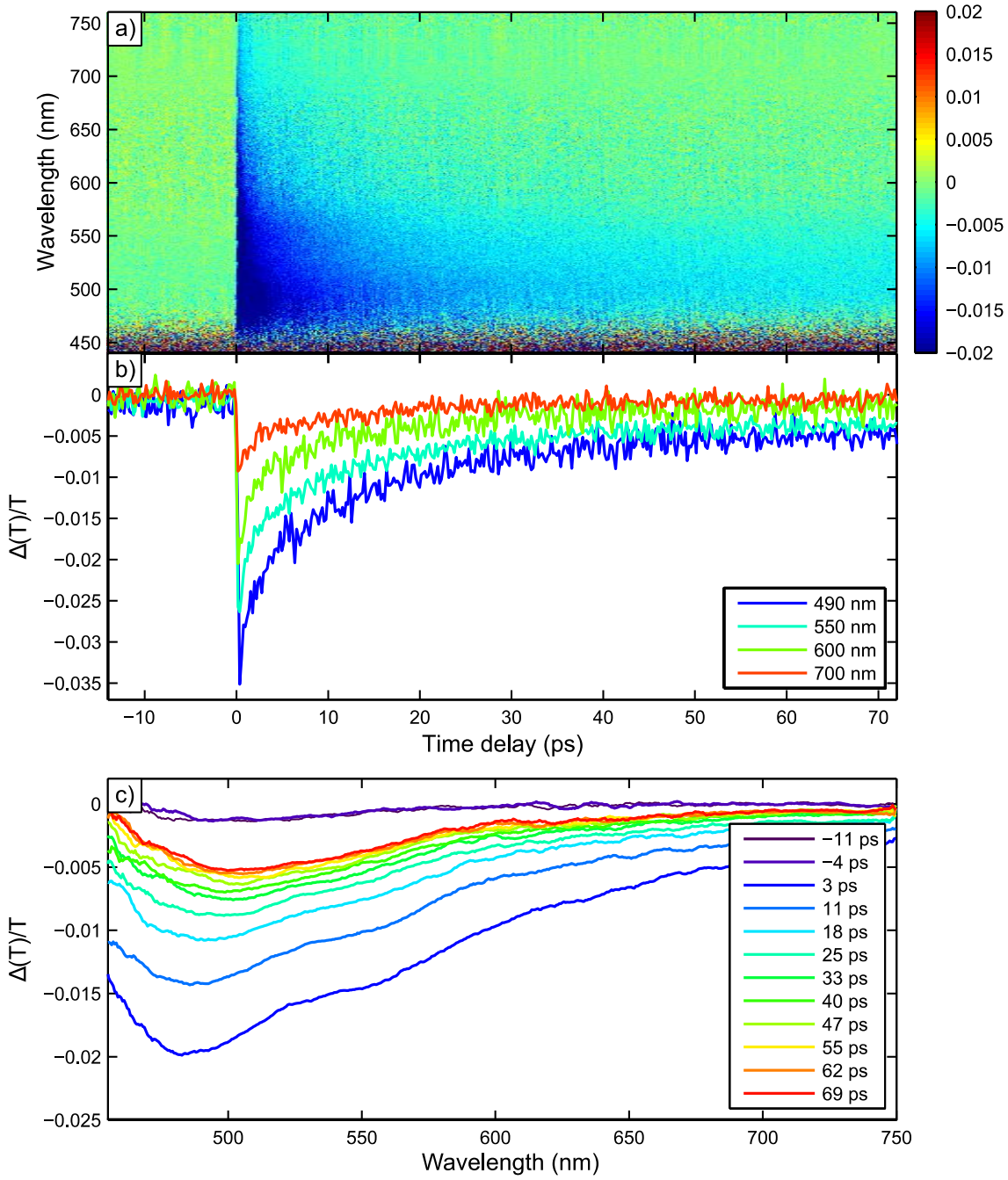

Figure 6-3 The relative change of the transient transmission of the 1081 nm thick LBL Azo sample under 398 nm excitation. a) Broad band ΔT/T. b) ΔT/T at 490-590 nm. c) Broad band ΔT/T at certain time delays.

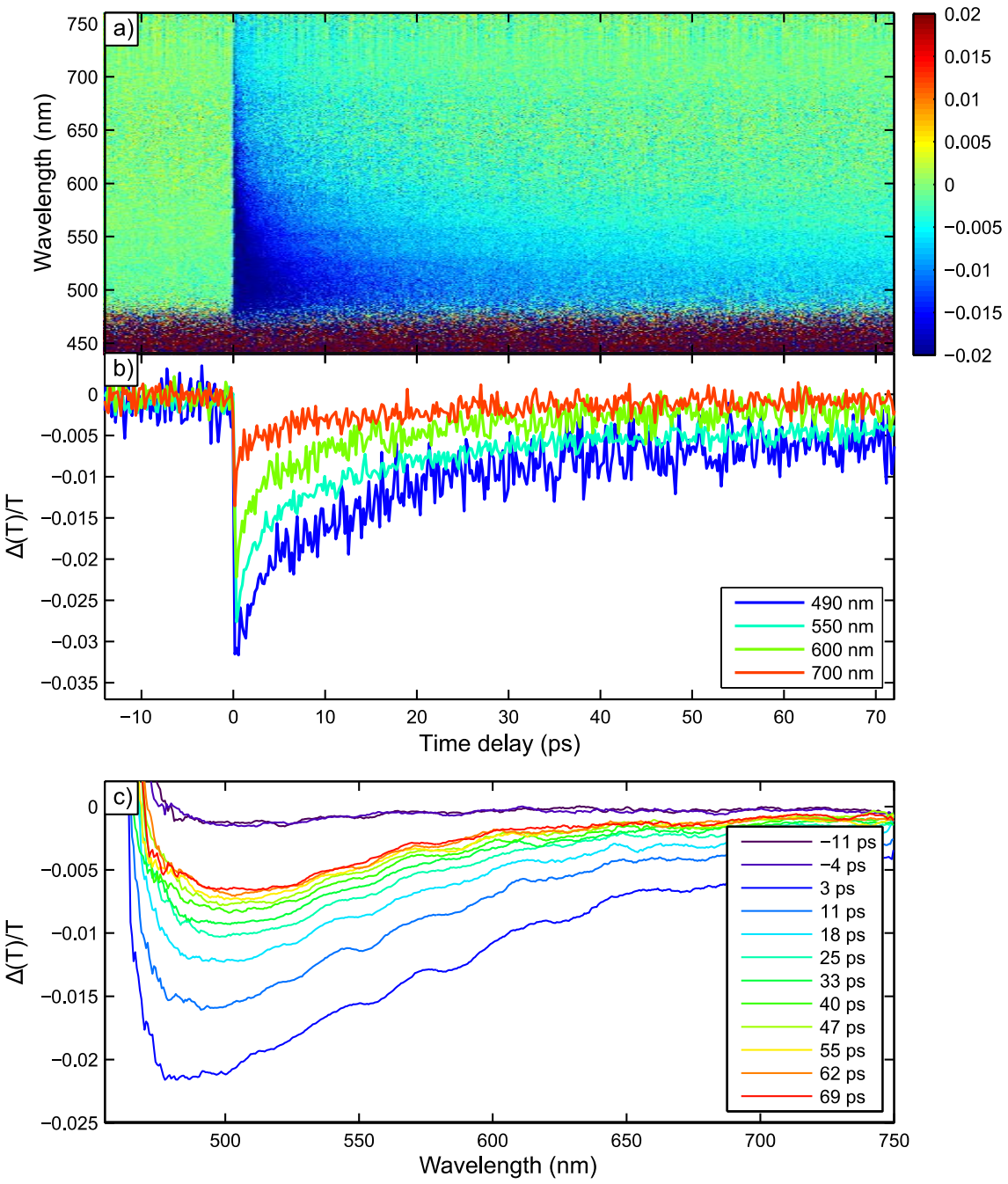

Figure 6-4 The relative change of the transient transmission of the 2414 nm thick OD Azo sample under 398 nm excitation. a) Broad band ΔT/T. b) ΔT/T at 490-590 nm. c) Broad band ΔT/T at certain time delays.

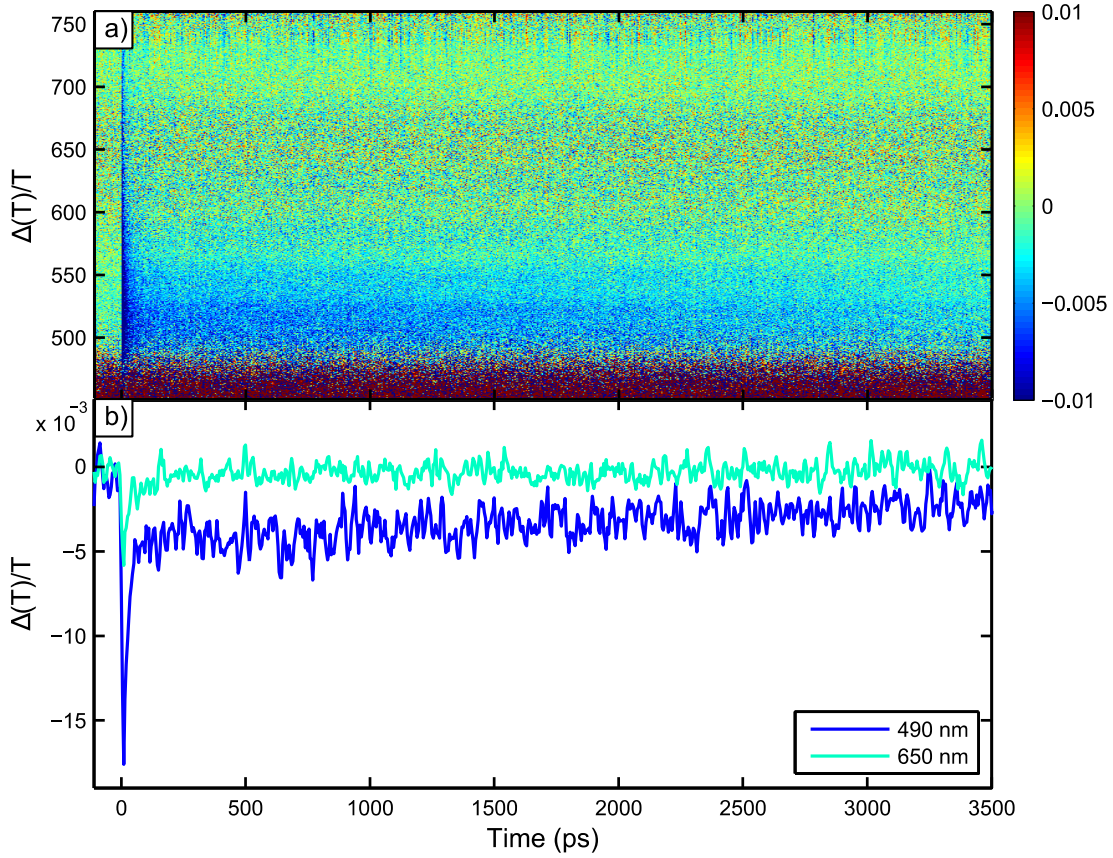

Figure 6-5 a) Broad-band spectrum of the relative change of the transient transmission of the 2414 nm thick OD sample. b) ΔT/T at 490 and 650 nm.

6.2. Reflection data analysis

Static and transient reflection spectra carry information about the thickness of the investigated film and about its refractive index. This information makes reflection spectroscopy a convenient tool for the investigation of generation and propagation of the strain, and the dynamics of the refractive index under the excitation.

Data for the transient measurements of the transmission spectra were always measured simultaneously with the reflection spectra, and those, which are relevant for the data analysis, will be presented in the discussion or in the appendix section.

6.2.1. Static Reflection

Static reflection spectra are used as reference to the transient reflection measurements. Reflection spectra for the Layer-by-layer made films of thickness 282, 423, 564 and 705 as well as for the 2414 nm thick OD film are presented in Figure 6-6. The spectra clearly show the modulations due to thin film interference effect. This effect appears when light beams reflected at the surface and at the polymer-substrate interface interfere with each other. Minima of the resulting interference pattern as a function of the wavelength λ appear when the following condition is fulfilled

$$2n_{film}dcos(\beta) = m\lambda \tag{6-1}$$

where β is the internal angle of incidence according to Snell's law in the film with the refractive index $n_{\text{film}}(\lambda)$ and thickness d. For the PAzo/PAH films, the refractive index at 600 nm was determined by ellipsometrly to be ~1.67 and ~1.71 for OD films.

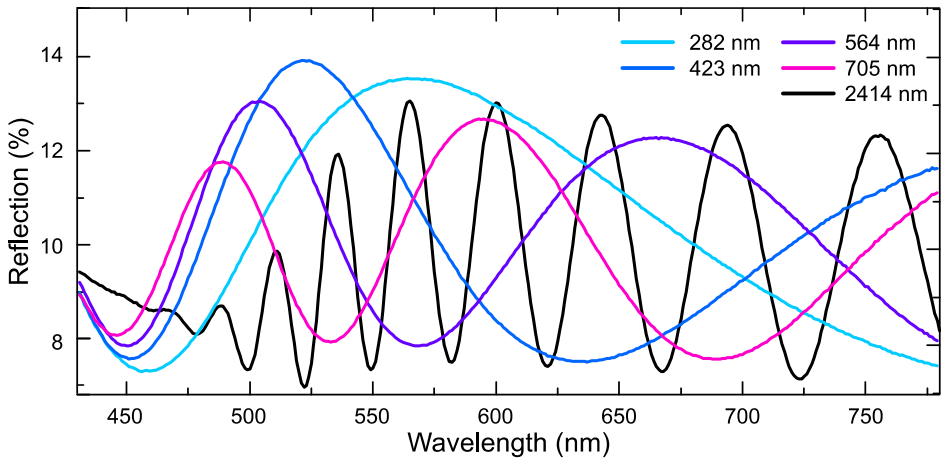

Figure 6-6 Static reflection spectra for the 282, 423, 564, 705 nm LBL films and for the 2014 nm OD film.

6.2.2. Transient reflection

In order to investigate generation, propagation, and reflection of the strain generated by layer-by-layer (LBL) prepared Azobenzene containing polyelectrolyte films, I have prepared a sample (sample 17) with a film thickness of 282 nm. After static and transient characterization, I increased the thickness of this film by additional LBL deposition up to 1081 nm with intermediate steps at 282, 423, 564, 705, and 864 nm. The measurements of the relative change of the transient transmission and reflection were performed for the time delay ranges of 340 and 640 ps. The measurements for time delays up to 340 ps were performed with the higher time resolution and better statistics by averaging over 15 loops. The measurements of the relative changes of the transient reflection and transmission of the time delays up to 640 ps have lower time resolution and were averaged over 10 loops. Nevertheless, the data are good enough to show the dynamics on the times scales several times greater than the time of the strain wave propagation, which is useful for the analysis of the strain dynamics within the film and at the interfaces. These measurements are placed in the Appendix section (chapter 11). The data sets for the transient reflection for time delays of

340 ps are presented in Figure 6-7 (for the film of 282, 423 and 564 nm) and Figure 6-8 (for the film of 705, 864 and 1081 nm). All the data sets show several pronounced features. First is the thin film interference effect (TFI), shown in the static reflection spectra (Figure 6-6). In the transient spectra, this effect appears as modulation of the sign of the ΔR/R across the wavelength axis. As shown in the static spectra, the number of the fringes increases as the film thickness increases. Therefore, in the ΔR/R spectrum of the 282 nm film one can observe only one region of the negative signal, while for 705 nm thick film three regions of the negative signal, corresponding to the TFI. The thin film interference related features in the transient spectra are observed immediately after the pump-pulse, indicating an instantaneous change of the refractive index of the sample upon excitation. This instantaneous change of the refractive index appears as areas of negative and positive signal on the transient ΔR/R spectra. Figure 6-7 shows the position of these areas overlaid with the static spectra of reflection.

In transient ΔR/R spectra, the TFI related pattern is changing in time, namely the entire pattern is shifting to lower wavelengths with time delay. For thicker samples, this shift is observed for longer time delays. Figure 6-9 shows the comparison of the relative shift of the TFI pattern for the samples with different thicknesses. The left y-axis represents the time until which the observed shift lasts, which is also the time when the strain generated at the surface reaches the substrate and reflects from it. The TFI pattern depends on the refractive index and the thickness (equation 6-1) therefore, the transient dynamics of this pattern must also be related to the changes in these parameters. The shift of the TFI pattern towards lower wavelengths means that thickness of the film increases and the refractive index decreases. This conclusion comes directly from the equation (6-1) applied for the case of an expanding film (d increases). Similar results have been observed by Tanchak et al[19] on longer time scales. This effect will be discussed in more detail in chapter 8.

Another notable feature for all the ΔR/R of sample 17 is the pronounced oscillations as a function of the time delay. The wavelength-dependence of the oscillation period is given by formula (2-19) and is characteristic of time-domain Brillouin scattering (TDBS)[3,99]. Here, β is the internal angle of incidence according to Snell's law in the film, with refractive index $n_{film}(\lambda)$ and the sound velocity in the film is v_s. TDBS can be interpreted as interference of the probe light reflected at the surface and from the propagating strain pulse (Figure 2-5). Figure 6-10 shows ΔR/R for a 564 nm thick LBL sample of PAzo/PAH. This measurement is averaged over 17 loops and has step size of 2 ps which results in good statistics of the measurement. The raw data in Figure 6-10 a) show pronounced "fan" – like structure of the oscillations, where the period is increasing with the wavelength. The oscillatory component is extracted by applying a high frequency filter. Only the components of the spectrum, oscillating with the period below 80 ps are extracted. The oscillatory component presented in Figure 6-10 b) shows this "fan" – like structure more clearly. The observation of the TDBS confirms the presence of a strain wave. The relation between the observed TDBS signal and the strain wave propagation is discussed in detail in chapter 8.

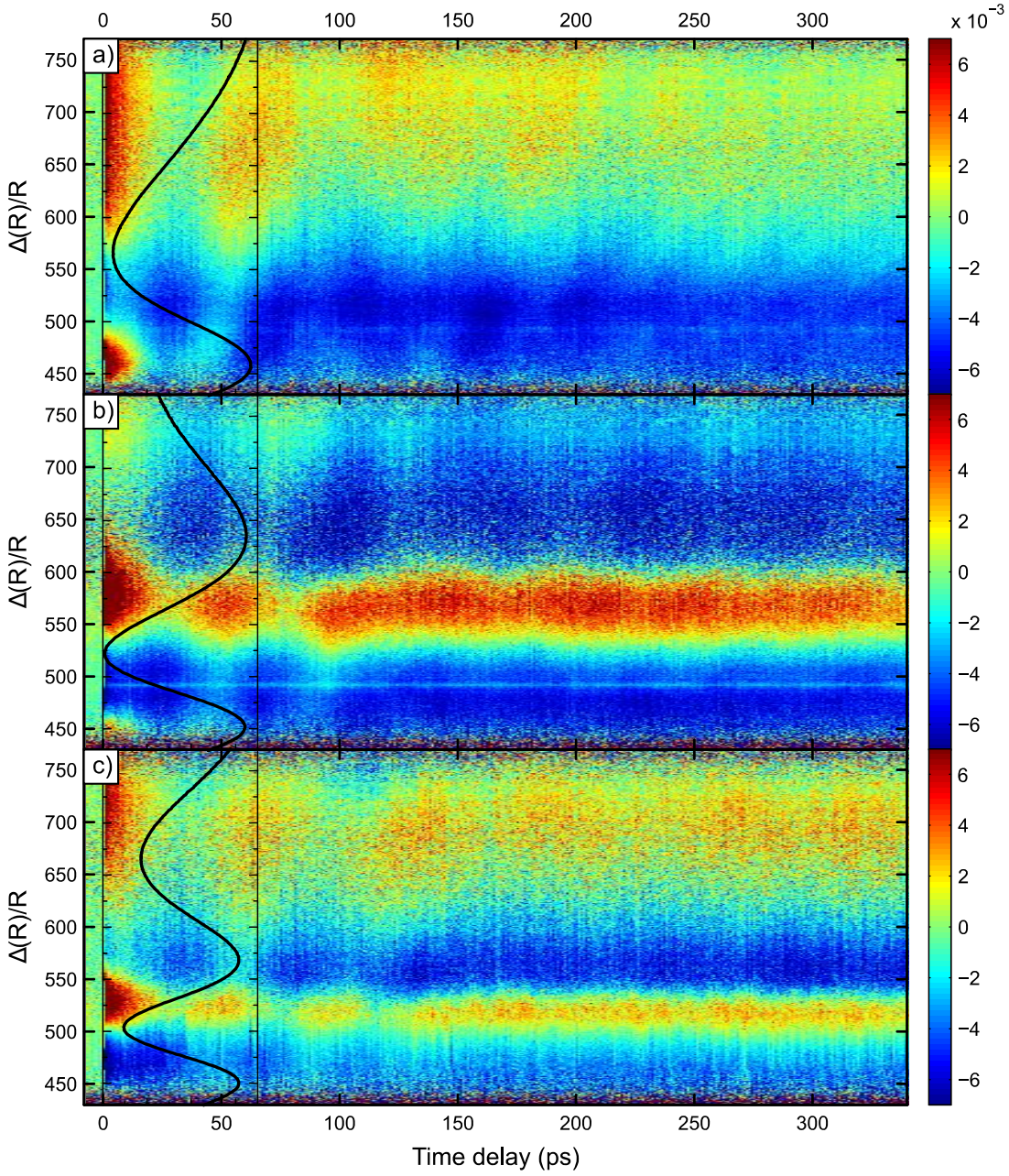

Figure 6-7 The relative change of the transient reflection for sample 17 (LBL film on Quartz) for different thicknesses. a) 282nm, b) 423nm) 564nm.

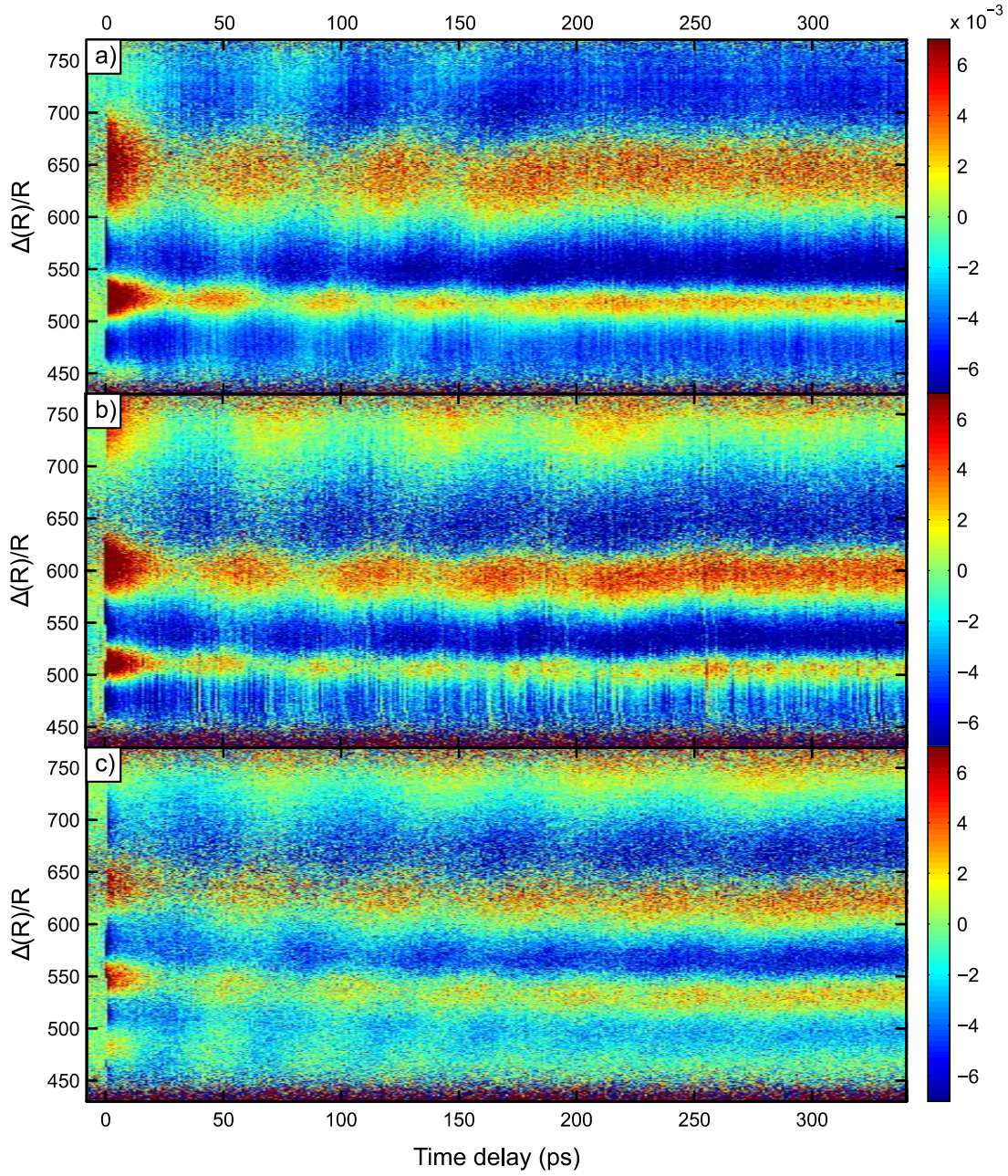

Figure 6-8 The relative change of the transient reflection for sample 17 (LBL film on Quartz) for different thicknesses. a) 705nm, b) 864nm) 1081nm.

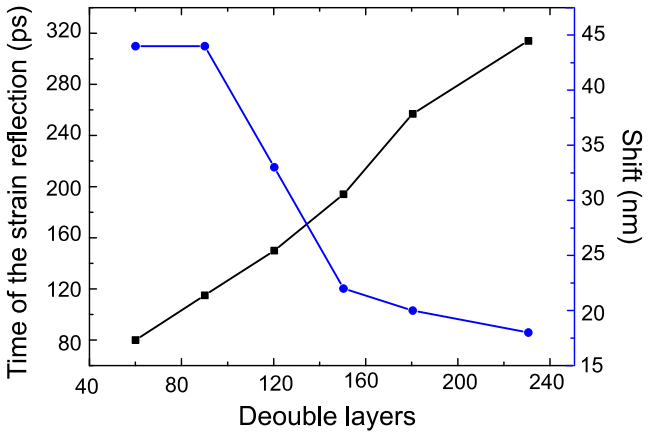

Figure 6-9 A comparison of the relative shift of the thin film interference pattern (right y-axis) for the samples with different numbers of double layers (thicknesses). The left y-axis represents the time until which the observed shift lasts, which is also the time when the strain generated at the surface reaches the substrate and reflects from it.

By analyzing the tilt of the TDBS oscillatory pattern one can follow the dynamics of the strain propagation within the transducer. The phase of these oscillations and their amplitude carries information about the interfaces impedance mismatch. At T_1 = 180 ps the strain generated at the surface has reached the Quartz substrate. The impedance of the polymer film is $Z_{poly} \approx 3.4$ and the impedance of Quartz is Z_Q = 12.7. This results in acoustic reflection coefficient $R_{ac} = (Z_{poly} - Z_Q)/(Z_{poly}+Z_Q) = 60\%$. Therefore, 60 % of the strain pulse is reflected from the Azo/Quartz interface, while 40 % propagates into the Quartz substrate. After T_1 the strain pulse propagates towards the surface, which result in an opposite tilt of the TDBS oscillation pattern with respect to the pattern before T_1. Another reflection occurs at $T_2 = 2*T_1 =$ 360ps. At the film/air interface, no losses occur and the whole strain pulse is reflected back into the polymer layer. The third reflection at the Azo/Quartz interface at T_3 = 540 ps again results in losses of the strain pulse to the substrate and the TDBS signal is no longer observed after this time delay. The timing of the discussed reflections is given by the thickness of the film d = 564 nm and by the sound velocity in the film, which is 3.4 nm/ps. The dynamics of the strain front propagation and reflections will be discussed in detail and compared to the simulations in chapter 8.

Strain related effects such as thickness changes are more pronounced in transient reflection spectra. Moreover, TDBS appears mainly in those spectra, therefore further analysis of the strain propagation, reflection, and interaction with nanoparticles will be performed by discussing the transient reflection spectra. Transient measurements of the transmission spectra were always measured simultaneously with the reflection spectra, and those, which are relevant for future data analyses will be presented in the discussion or in the appendix section.

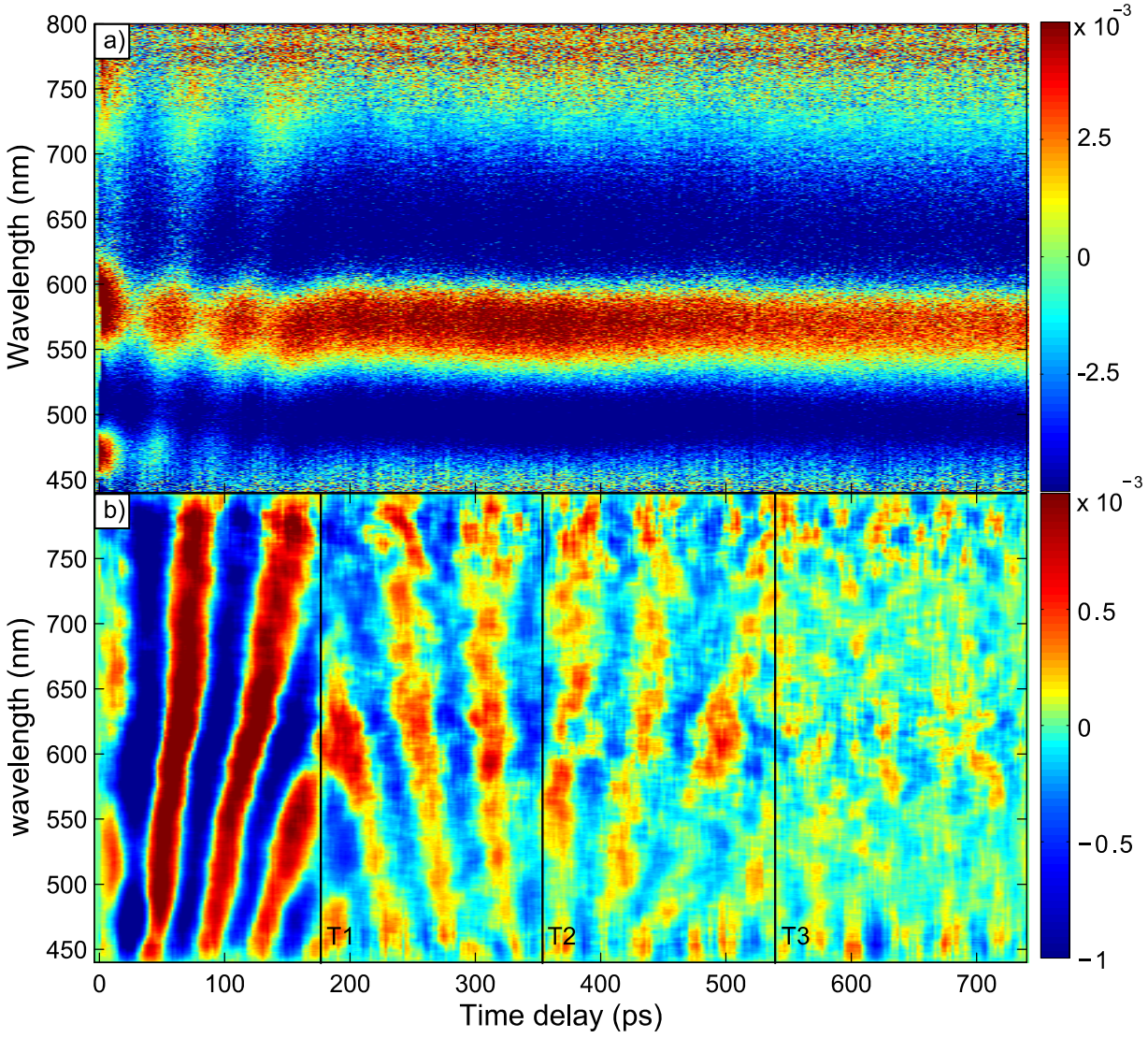

Figure 6-10 a) The relative change of the transient reflection (ΔR/R) of sample 35 (564 nm PAzo/PAH on Quartz). b) The oscillatory component of ΔR/R

6.2.3. «One drop» structure

This subchapter presents results obtained on "one drop" Azobenzene thin films, which are typically 1-2 μm thick and have a different structure compared to the LBL films. Unlike the LBL-made samples, films obtained by this method are not expected to have an ordered structure, caused by the preparation method. By measuring the transient reflection for these structures and comparing the data to the LBL samples, one can conclude if the order in LBL structures (if there is any) plays a role in the strain generation.

The thickness of the investigated film (Sample OD) was measured by ellipsometry (chapter 4.2) and found to be 2414 nm. Relative changes of the transient reflection for the 2414 nm OD sample are shown in

Figure 6-11 a). In Figure 6-11 b) the oscillatory component of the ΔR/R is presented. Both plots show features very similar to those observed for the LBL sample e.g.: the shift of the thin film interference pattern and the Brillouin scattering. For the 2412 nm thick film, these features are expected to last up to 700 ps, and such duration is observe in the presented transient spectra of ΔR/R. The presence and the length in time delay over which the TDBS oscillations can be observed, tell us that the strain has been created at the surface of the film and propagates towards the substrate, similar to the LBL-made structures. A detailed comparative analysis of the strain generation efficiency between these two Azobenzene – containing types of films, other types and other photosensitive molecules is certainly interesting and is a part of the outlook of this thesis.

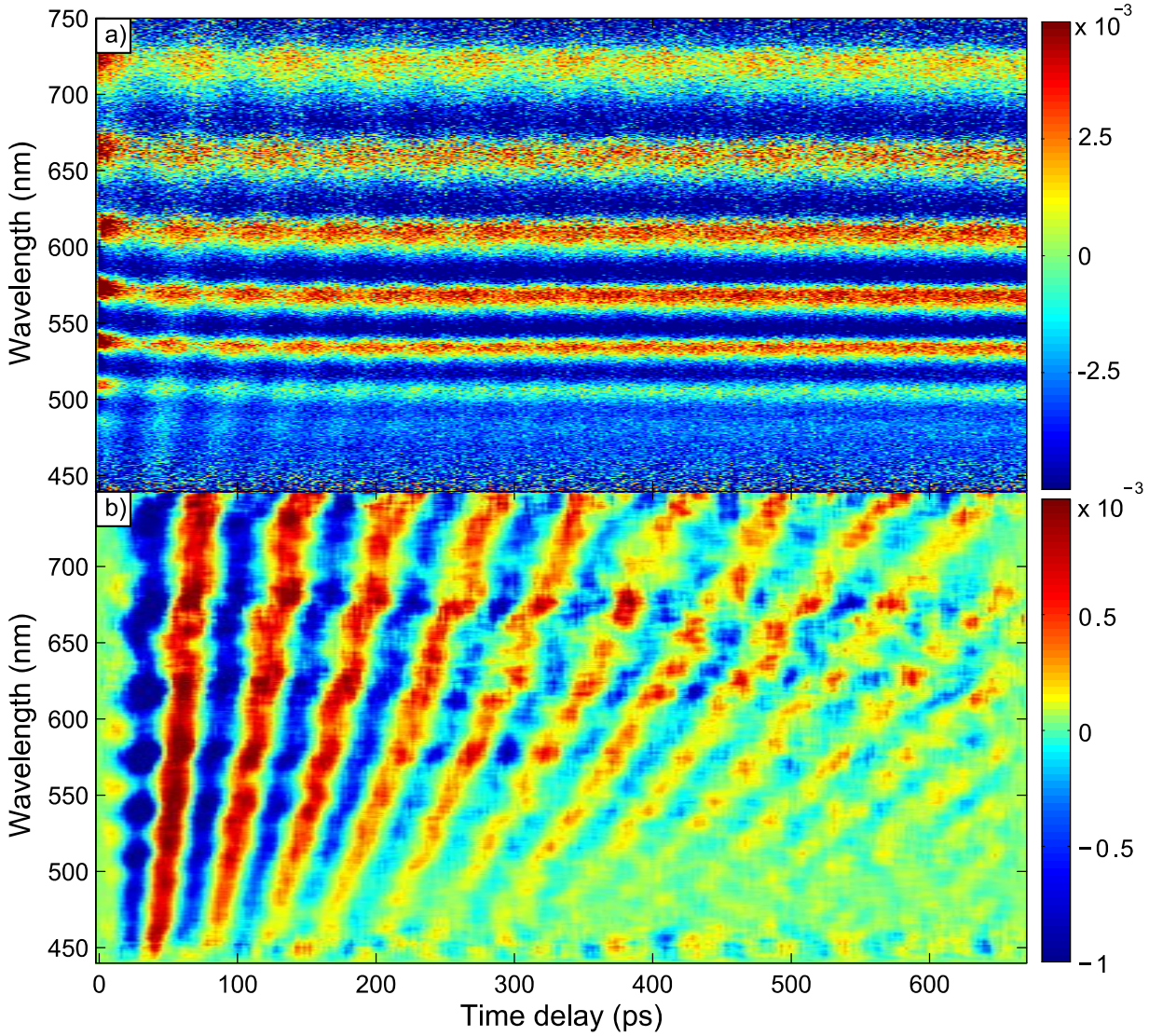

Figure 6-11 a) Relative change of the transient reflection (ΔR/R) of 2414 nm thick OD film on Quartz. b) Oscillatory component of ΔR/R.

6.3. Strain in an adjacent polymer

One of the main advantages of soft matter transducers is the match between the acoustic impedances of the transducer and the investigated soft materials such as polymers or biological tissues. Up to now, there are only few studies[7,9,100], that have investigated the properties of soft materials by following the strain inside the material on picosecond time scales. However, all of those studies use common metal transducers such as aluminum or titanium for the strain generation. Such hard materials have significantly different acoustic impedances compared to biological tissue. This results in multiple reflections of the strain wave at the interface. Most metal transducers reflect a lot of the incident pump light, which leads to low efficiency, in sense of the transformation of the incoming light into strain. Moreover, metal films usually require additional treatment in order to provide a reliable and homogeneous connection between the transducer and the studied material. Therefore, a soft matter transducer would be beneficial for the strain generation into other soft matter materials.

In order to investigate the strain propagation into an adjacent polymer, I have prepared a sample with the following structure: on a Quartz substrate 116 dl PSS/PAH - (GNR type III - 8 dl PSS/PAH)*4 - 104 dl PSS/PAH - 30 dl PAzo/PAH (sample 26 in Table 3-3). This structure allows investigation of the strain propagation inside the adjacent polymer and shows the opportunity to detect the position of inner impurities down to tens of nanometers. PSS and PAH polyelectrolytes do not absorb light in the region of the pump pulse wavelength of 400nm as can be seen in Figure 6-1. The relative change of the transient reflection for this sample (Sample 26) is presented in Figure 6-12 a). The wavelength range is chosen to avoid the areas of the plasmon resonances, which are at 530 and 700 nm. Similar to the data discussed in chapter 6.2.2, one can see the modulation of the signal across the wavelength range. This is the thin film interference – related pattern, which appears from the interference between the probe pulse, reflected from the surface and the film/Quartz interface. Another feature similar to the data discussed before is the intensity modulation of the signal along the time delay axis. This is the time-domain Brillouin scattering (TDBS), originating from the interference of the probe light reflected at the surface and from the propagating strain pulse. The presence of the TDBS confirms that the strain generated by the Azobenzene-containing transducer is propagating thought the adjacent polymer. Unlike in the previous data, no shift of the thin film interference pattern is observed in this case. Due to the small thickness of the transducer relative to the total thickness of the sample, both parts of the bipolar strain pulse must be present in the structure at early times (81 ps). Only the first half of the bipolar strain pulse is present in the sample up to 41 ps, however the signal of the hot electrons is dominant at these time delays. The changes of the thickness and the refractive index are canceled out by the opposite signs of the bipolar strain pulse parts, therefore no shift of the TFI pattern is observed.

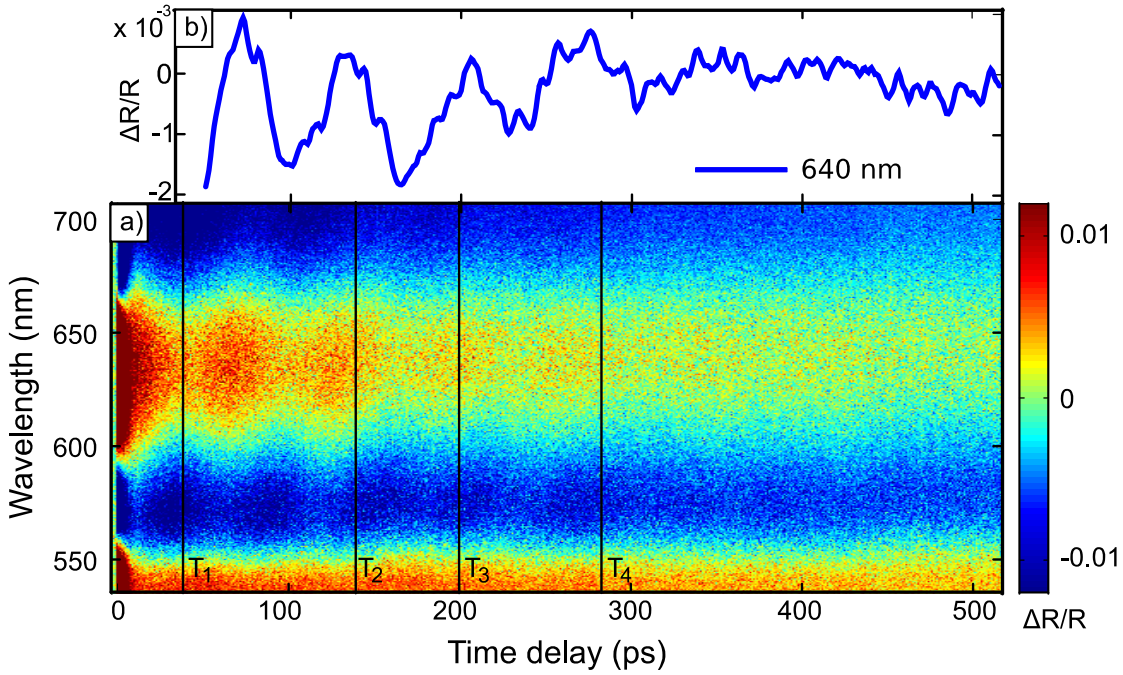

Figure 6-12 a) The relative change of the transient reflection for sample 26 (252 dl PSS/PAH with GNR incorporated in it, plus 30 dl PAzo/PAH on top). T_1 is the time when the strain generated at the surface of the sample has reached the PSS/PAH layer. T_2 corresponds to the time when the strain has reached GNR. T_3 is the time after which the strain leaves the layer of GNR. T_4 corresponds to the time when the strain has reached the Quartz substrate. b) ΔR/R for 640nm, the exponential decay has been subtracted.

6.4. Strain in hard adjacent materials

One of the central advantages of PAzo/PAH transducers is the match of the acoustic impedance with soft materials. However, it can also send strain into hard adjacent materials, such as Quartz or Mica. In this chapter strain propagation and detection in such hard materials is discussed.

6.4.1. Strain in Quartz

Sample 17 is a film of PAzo/PAH on Quartz. In this measurement, the film thickness was 60 dl, which corresponds to approximately 282 nm. The relative change of the transient reflection for this sample was briefly discussed in chapter 6.2.2, where the data of ΔR/R are shown in Figure 6-7 a). The original data of ΔR/R discussed in this sub-chapter were measured for longer delay time and placed in the appendix section (Figure 11-1 a). Here we will discuss only the oscillatory component of ΔR/R, shown in Figure 6-13. The dynamics of the TDBS pattern discussed in 6.2.2 for T_1, T_2, T_3 for the same sample with the PAzo/PAH film of 564nm is also true for the thickness 282 nm and discussed in this subchapter. The only

difference is the timing, which is now shorter due to the smaller thickness. For this sample, only one full period of the TDBS can fit between the reflections from the interfaces. After the third reflection, no TDBS from the strain propagating within the polymer film is observed, but TDBS with a higher frequency appears. These higher frequencies of the Brillouin scattering come from the strain propagation in a material with a higher sound velocity. In quartz it is 5.8 nm/ps versus 3.4 nm/ps in PAzo/PAH[101]. The observation of the TDBS with a frequency corresponding to the sound velocity in Quartz (according to the equation (2-19)) confirms that strain has propagated into the substrate. In samples with thinner layers of PAzo/PAH the TDBS in Quartz is more visible because the phonon spectrum generated by thinner transducers is more suitable for the spectral region covered by our white light probe[85].

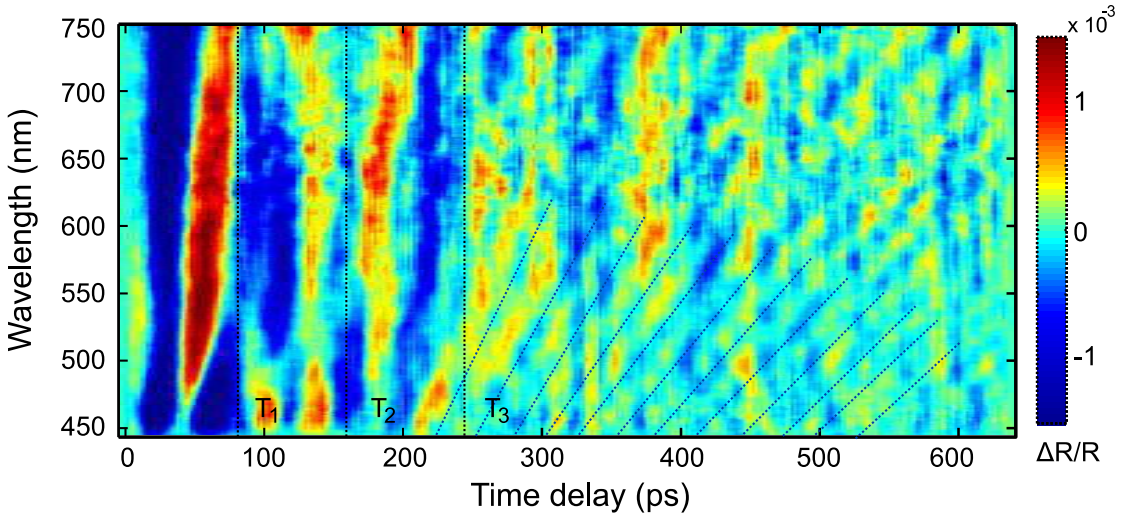

Figure 6-13 Oscillatory component of $\Delta R(t)/R_0$ for 282 nm thick PAzo/PAH film on quartz (sample 17).

6.4.2. Strain in Mica

In order to calibrate the strain amplitude generated by the optical excitation of PAzo/PAH films we measured the strain as it propagates into a crystalline medium. The change of the lattice constant can be measured in real time by ultrafast X-ray diffraction[61]. We chose mica as a suitable substrate since it has a weak absorption at 400 nm and it is suitable for the deposition of polyelectrolytes. Another advantage of mica over other crystalline materials is the relative ease in obtaining thin films (several μm). It is important that the thicknesses of the substrate and the transducer film are comparable so that the strained area in the substrate is comparable to the unstrained one. I prepared a film with $d_{PAzo/PAH}$ = 880 nm onto a 4.5 μm thick Mica substrate (Sample M). Figure 6-14 shows the detected shift of the Bragg angle Θ, from which the transient strain calculated via $\varepsilon_{obs}(t) = \Delta c(t)/c = -\Delta\Theta * \cot(\Theta)$, where c is the out-of-plane lattice constant of mica. The maximum compression of mica is observed at t = 260 ps, when the expansion wave created at the surface has propagated fully through the transducer. At this time, the compressive leading part of the wave front has propagated around 1.3 μm into the substrate[61]. The average strain within

the first micrometer is about four times larger than the measured strain since the remaining 3.2 µm of the mica film are unchanged from its initial lattice constant. Hence the strain pulse detected in mica has an amplitude of about $\varepsilon = -5\times10^{-5}$. This is consistent with our simulation[62,63] of the strain in mica (dashed line in Figure 6-14) based on a linear chain-model (chapter 2.3.2). The agreement of the simulation with the measured data confirms that the hyper-sound-pulses creation and propagation of sound in the investigated soft-matter materials can be well described by a linear chain model (with the sound-velocity $v_{poly} = 3.4$ nm/ps characteristic of hyper-sound in polymers).

From our model we predict that the corresponding expansion of the PAzo/PAH film at $t = 260$ ps will be $\varepsilon = 5\times10^{-4}$. The model simulates a linear chain of masses and springs, which are adjusted such, that the mass density and sound velocity of the materials are described correctly. The optical excitation is assumed to instantaneously generate a stress profile with given by the absorption depth in the PAzo/PAH film. For calculating the strain in PAzo from the measured lattice deformation in mica, the model automatically takes into account three factors[61,63]: i) 60 % of the compressive sound has been reflected at the PAzo/Quartz interface due to the acoustic impedance mismatch. ii) The static expansion of the photoexcited PAzo layer adds to the coherent sound wave. iii) The strain in mica is reduced by ratio 5/3. iv) of the sound velocities as the pulse is stretched.

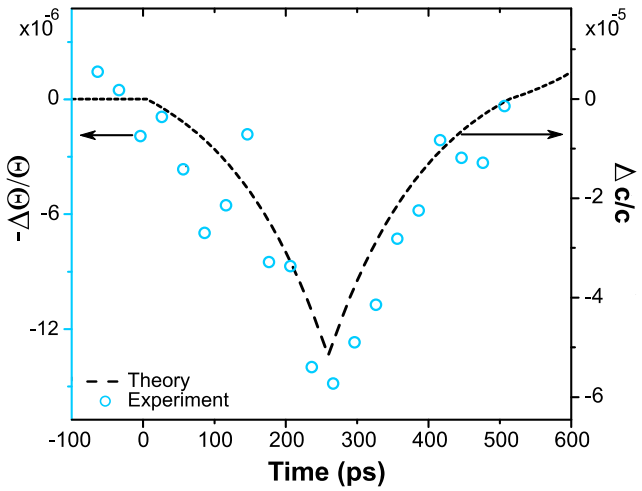

Figure 6-14 The time dependence and amplitude of the measured change of the diffraction angle ΔΘ (blue circles) agrees well with the average strain of the strained part of mica as calculated by the linear chain model (dashed line).

7. Transient response of gold nanorods to hyper-sound waves

One of the main goals of the project was to explore the interaction between gold nanoparticle and hyper-sound waves on the picosecond time scale. To reach this goal I have tested numerous structures, varying the components thicknesses, order, and other parameters. In this chapter, I will present the measurements obtained for selected samples that contributed the most into understanding the phenomena. The second part of the chapter represents the data showing the response of GNRs to hyper-sound

7.1. Sample Architecture

Designing the sample structure is an important step in measuring and understanding phenomenon. It is especially challenging when the phenomena are novel and no literature is available. This chapter will show the steps of the sample design which were taken on the way to our successful results. The results presented in this chapter shows the results of the systematic analysis of the structures, which helped to develop a better understanding of the phenomena of GNRs ability to sense the hyper-sound waves.

7.1.1. Position of the GNR within the sample

Sample 15 After it was established that PAzo/PAH film can generate strain and the strain will then propagate into the substrate (chapter 6.4.1), it was logical to design sample architecture such that the GNRs are placed between the polymer transducer and the Quartz substrate. Measurements of the transient spectroscopy were performed for the sample after the deposition of GNR type II on 8 dl of PSS/PAH. The relative changes of the transient reflection are shown in Figure 7-1 a). Data for the transmission are placed in the Appendix (Figure 11-5 a). Both plots clearly show the signal related to the transverse and the longitudinal plasmon resonances. This crosscheck measurement was performed to make sure that the particles are deposited and provide the signal in the transient data under the excitation by the 398 pump-pulse. After this cross check measurement, additional 60 dl (282 nm) of PAzo/PAH were deposited on top of GNRs. The relative changes of the transient reflection and transmission for this sample structure are presented in Figure 7-1 b) and Figure 11-5 b) respectively. These measurements should be compared to the data presented in paragraph 6.2.1, where the data for the PAzo/PAH film on Quartz are discussed. Besides the characteristic features discussed in that section such as thin film interference effect and time domain Brillouin scattering, one can also observe the signal related to GNRs. This signal can be observed clearly at the wavelengths around 525 nm, the region that is related to the dynamics of the transverse plasmon resonance of GNRs. The signal appears at the higher wavelength relative to the uncovered sample Because the GNRs are now covered (see chapter 5.3). The positive signal at 525 nm decays significantly within 50 ps and stays visible up to 600 ps. However, relative to the data without GNRs, no

difference is observed at the wavelengths containing the signal related to the longitudinal mode of the plasmon resonance. Neither of the modes show pronounced strain related dynamics. This sample has been grown up to 230 dl of PAzo/PAH, however already after 90 dl the signal from PAzo/PAH becomes a dominant and the signal related to GNRs was not observed. This brings us to the conclusion that the density of GNRs as well the amount of the absorbed light is important for the visibility of the induced dynamics of the plasmon resonances.

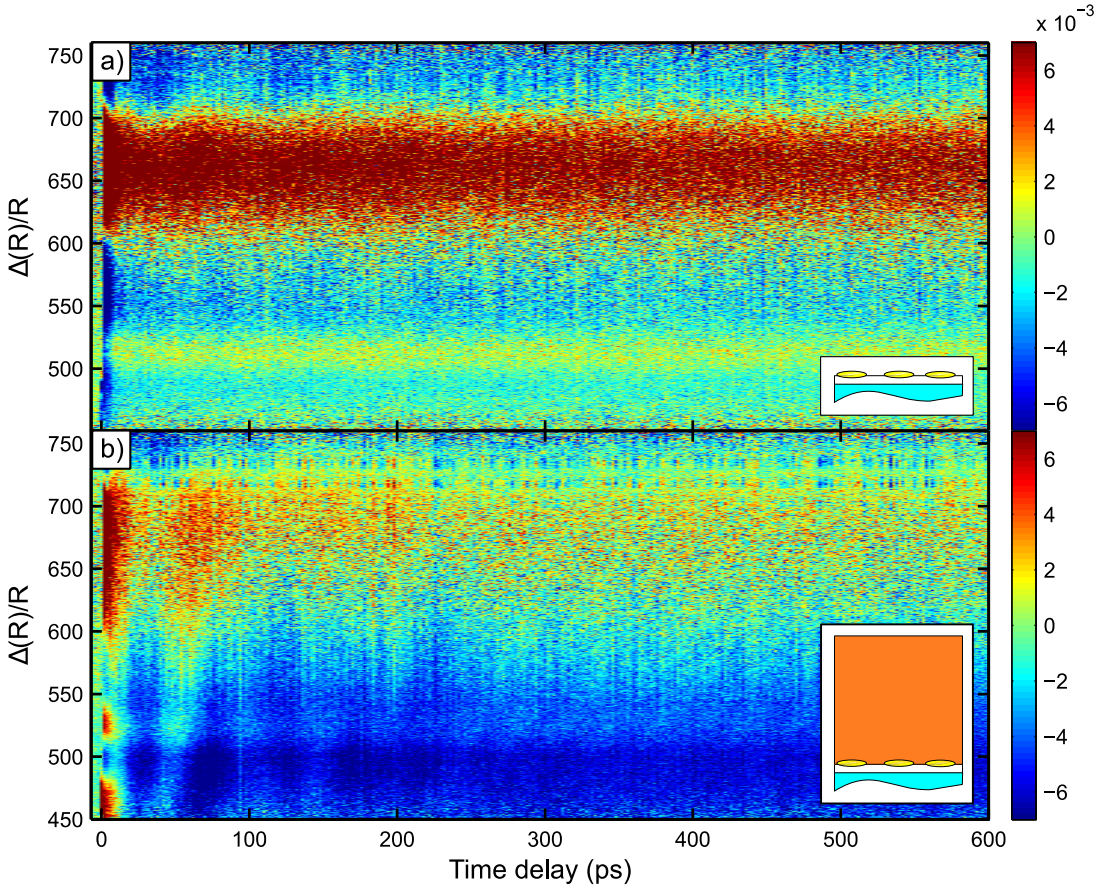

Figure 7-1 The relative change of the transient reflection for sample 15 (GNR type II on 8 dl of PSS/PAH on Quartz, covered 60 dl PAzo/PAH on top.

Sample 40 The idea of the next design was to place the gold nano-particles on the top of PAzo/PAH layer to make sure that enough light will reach them and excite the plasmon resonances. In order to increase the amount of the particles in the sample, a stack of GNRs/poly multilayer was built on the top of a PAzo/PAH film. The exact structure of sample 40 is the following: 90 dl of PAzo/PAH grown on a Quartz substrate, followed by 8 repetitions of (GNR III + 8 dl PSS/PAH). Static reflection and absorption spectra of the resulting structure are presented in Figure 7-2 a). The reflection spectrum shows two main spectral features - thin film interference effect and the plasmon resonances. The transverse plasmon resonance is centered at 525 nm and the longitudinal one contributes is at 700 nm. The absorption

spectrum shows clearly the positions of both modes of the plasmon resonance. These positions are shifted relative to the reference values from Table 3-2, because the GNRs are covered (see paragraph 5.3). The transient reflection spectrum (Figure 7-2 b)) shows features related to both components of the reflection spectrum (thin film interference and the plasmon resonances). The analysis of the oscillatory component of ΔR/R (Figure 7-2 c) shows that there is time domain Brillouin scattering, which disappears after approximately 30 ps. This can be explained by the strong damping caused by the several layers of GNRs. From this we can conclude that the observed shift of the maximum at 600-700 nm in ΔR/R can be attributed to the interaction between GNRs and the hyper-sound wave, however a different sample architecture is required for a clearer investigation of the phenomenon. The data of the relative change of the transient transmission is placed in the appendix section (Figure 11-6).

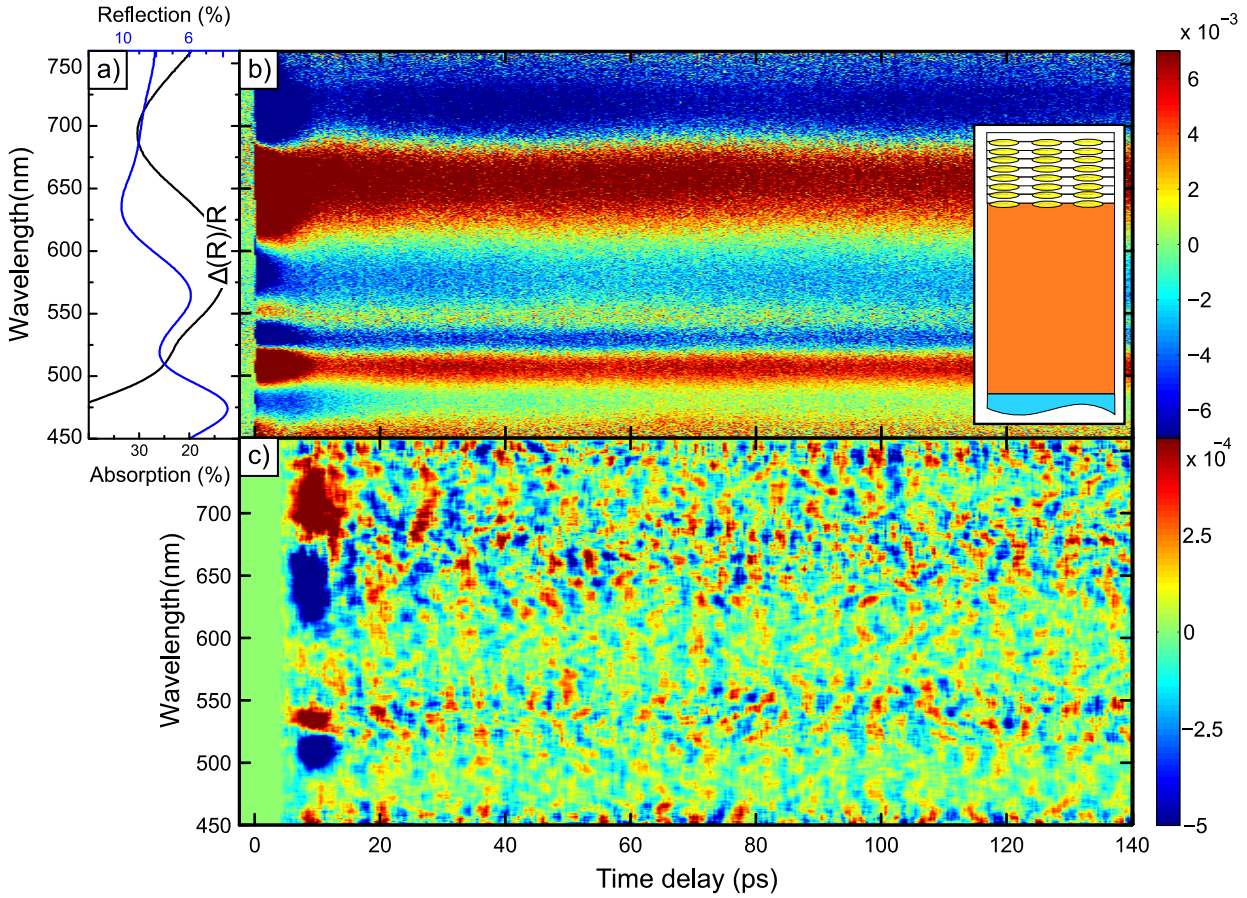

Figure 7-2 a) The measured static spectrum of reflection (R) and the absorption spectrum constructed as A = 1 –R – T. b) Relative change of the transient reflection for sample 40 (Quartz – 90 dl PAzo/PAH – (GNR type III – 8 dl PSS/PAH)*8). c) The oscillatory component of the ΔR/R.

Sample 42 This sample is very similar to the previous one and consist of 90 dl of PAzo/PAH deposited on the Quartz substrate, covered with two repetition of (GNRs type III + 16 dl PSS/PAH). By decreasing the number of layers with gold, the damping of the propagating strain wave should be reduced. However, it also leads to much weaker absorption by GNRs, hence the lower intensity of the GNRs -

related signal in ΔR/R. The static spectra of reflection and absorption of sample 42 are presented in Figure 7-3 a). The position of the longitudinal plasmon resonance appears at~710 nm. The transverse mode of the plasmon resonance is masked by the strong absorption of PAzo/PAH. The thin film interference pattern is clearly visible in the static reflection spectrum. Figure 7-3 c) shows the relative change of the transient transmission. This plot shows the negative signal corresponding to the excitation of Azobenzene, as well as the positive signal at 680 nm, corresponding to the longitudinal mode of GNRs and a weak signal at 530, corresponding to the transverse plasmon resonance. This plot is used as a reference for the tracking of GNRs- related features. In Figure 7-3 b) one can also see the spectral features, corresponding to GNRs signal, however it is difficult to distinguish them from the TFI-related pattern. The weak positive signal at 650 nm shifts to higher wavelength for about 20 ps. This shift is assigned to the dynamics of GNRs. However, the shift either does not last for long or moves out of the available spectral range of the probe-pulse, which does not allow us to assign is to the clear observation of the interaction between GNRs and the hyper-sound wave. The plot of the extracted oscillatory component of the ΔR/R for this sample (not presented) shows the Brillouin scattering effect, but only one period of the TDBS oscillation fit into the measured time delay range of 85ps.

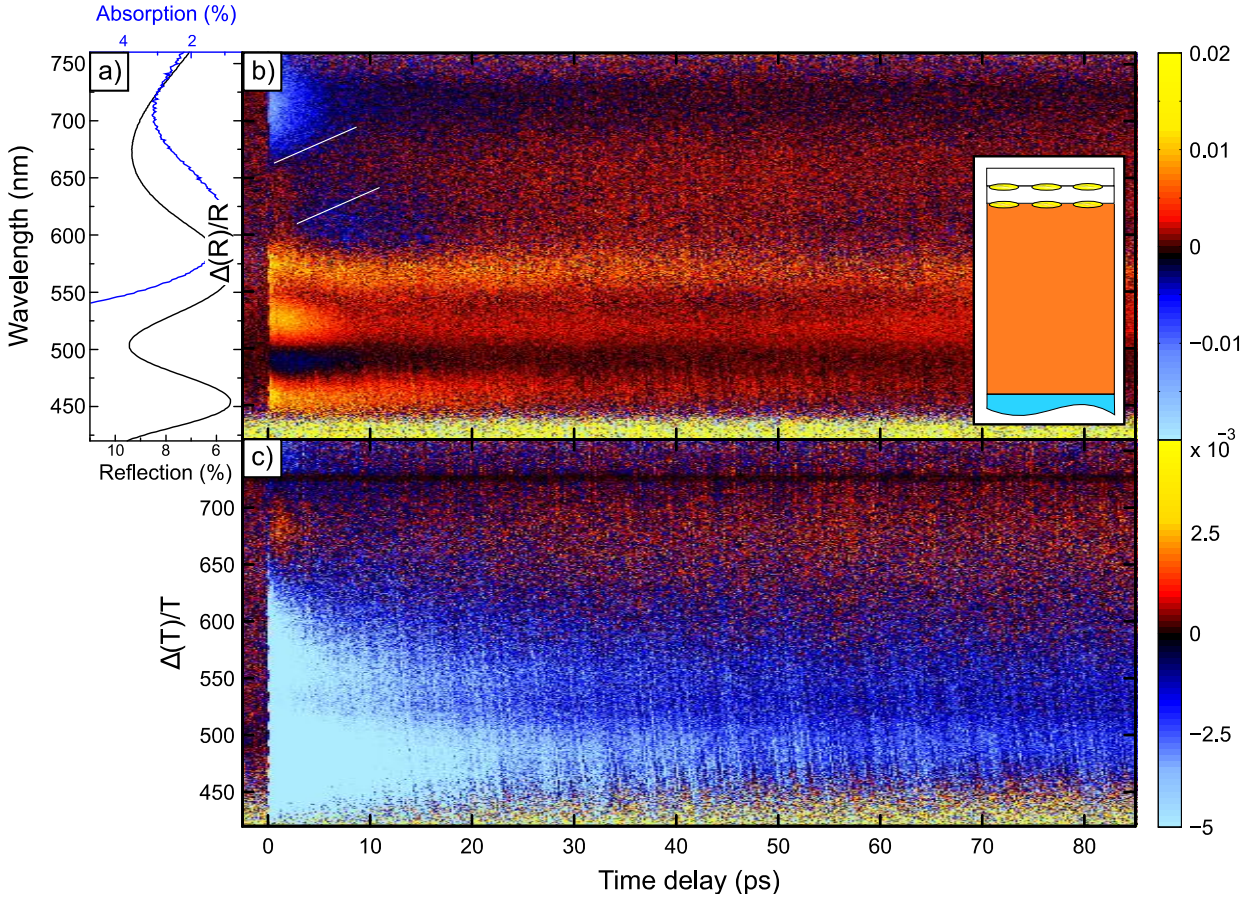

Figure 7-3 a) The measured static spectrum of reflection (R) and the absorption spectrum constructed as A = 1 –R – T. b) Relative change of the transient reflection for sample 42 (Quartz – 90 dl PAzo/PAH – (GNR type III – 16 dl PSS/PA)*2). c) The relative change of the transient transmission.

Sample 49 The idea behind the structure of this sample is to use the particles with the position of the longitudinal resonance at the wavelengths as small as possible, in order to be able to observe the dynamics throughout the entire spectrum of the used white light. To prevent the damping of the strain pulse propagating though the GNRs layer, I used only one layer of GNRs but with an increased concentration. The structure of sample 49 is the following: Quartz – 120 dl PAzo/PAH – 70 dl PSS/PAH – GNRs type V. The static reflection and absorption spectra of the sample are shown in Figure 7-4 a). In the static absorption spectrum, the peak of the longitudinal resonance extends up to 680 nm. This is probably caused by the presence of GNR clusters, which may have their longitudinal resonance at much higher wavelength than the single rods. However, in the plot of the relative change of the transient transmission (Figure 7-4 b) one can clearly see that the maximum of the positive signal related to the longitudinal plasmon resonance of GNRs appears at 580 nm, as expected for the GNRs type V. The results for the relative change of the transient reflection are show in Figure 7-4 b). No pronounced dynamics related to the GNRs interaction with the hyper-sound were observed. The cause of absence of the spectral features related to the response of GNRs to hyper-sound, in this data set is the overlay of the GNR spectral features and the fringes related to the thin film interference effect.

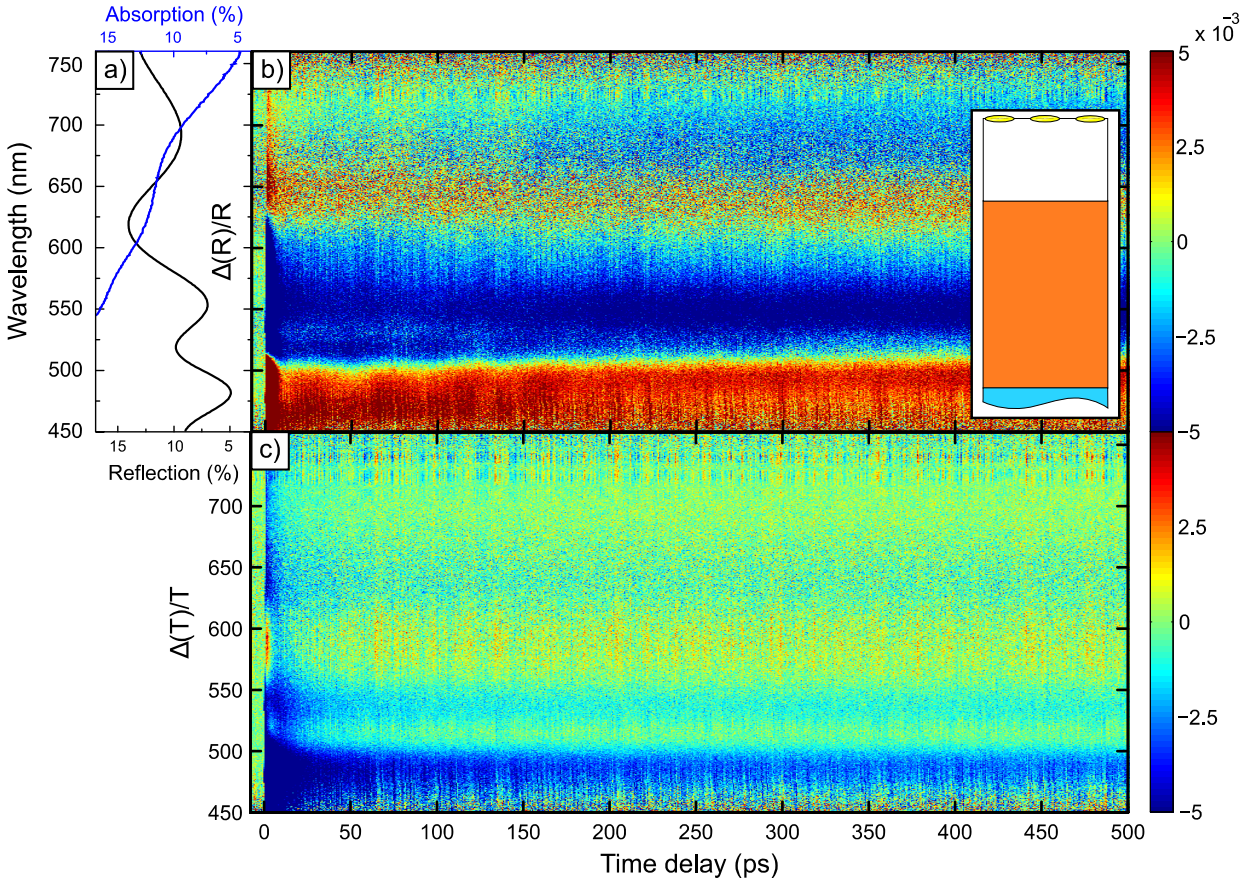

Figure 7-4 a) The measured static spectrum of reflection (R) and the absorption spectrum constructed as A = 1 –R – T. b) The relative change of the transient reflection for sample 49 (Quartz – 120 –70 dl PSS/PAH – GNRs V c) The relative change of the transient transmission.

In conclusion, of this chapter several parameter of the sample architecture were found to be important for the observation of the desired effect of GNRs response to the hyper-sound generated by a polymer transducer.

- The layer of GNRs has to have a high enough density to produce a strong transient signal.
- For the clearer visibility, the thickness of the transducer has to be thick enough to produce a relatively long strain pulse, in order to prolong the interaction between GNRs and the strain.
- In order to be able to observe the dynamics of the GNRs plasmon resonances, particles should be chosen such that their longitudinal resonance is at lower wavelength (close to the transverse mode).
- The total thickness of the sample has to be tailored in such a way that the thin film interference does not overlay with the position of the GNRs longitudinal plasmon resonance.

7.2. GNRs' response to the hyper-sound waves

The knowledge gained during the investigation of the samples described in the previous chapter allowed us to design samples that show the desired effect of GNR sensing hyper-sound wave on the picosecond time scale. In this chapter, the transient measurements of these samples will be presented and discussed.

Sample 52 This sample consists of a relatively thick transducer layer deposited on a Quartz substrate, followed by a transparent spacer layer with GNRs on top. The exact structure of the sample is the following: Quartz – 180 dl PAzo/PAH – 70 dl PSS/PAH – GNRs type IV. The static absorption and reflection spectra are presented in Figure 7-5 a). The static spectrum of the reflection shows the thin film interference pattern. In the static absorption spectrum, the longitudinal mode of GNRs plasmon resonance appears at 650 nm and the transverse mode (530 nm) is masked by the strong absorption of Azobenzene.

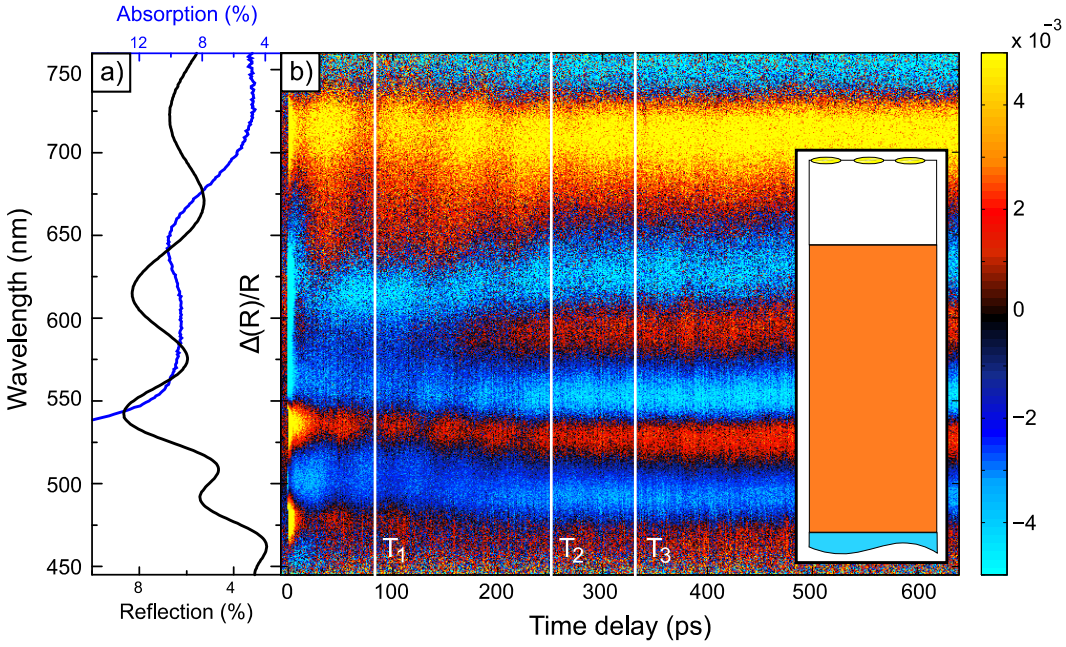

Figure 7-5 The measured static spectrum of reflection (R) and the absorption spectrum constructed as A = 1 –R – T. b) The relative change of the transient reflection for sample 52 (Quartz – 180 dl PAzo/PAH – 110 dl PSS/PAH – GNR IV)

The plot of the relative change of the transient reflection is shown in Figure 7-5 b). The transient data clearly show the features, observed in the previous samples, such as the thin film interference and the Brillouin scattering. White lines indicate the timing of notable features. T_2 = 248 ps is the time when the strain pulse, generated at the PAzo/spacer interface reaches the substrate. The time is calculated from the thickness of the PAzo/PAH layer (846 nm) and the sound velocity in the polymer (3.4 nm/ps). In the ΔR/R plot this time is indicated by the disappearance of the modulations related to the Brillouin scattering from the strain in the transducer film, indicating that the strain has reached the Quartz substrate and has been weakened by the reflection. T_1 = 80 ps is the time when the strain pulse, generated at the PAzo/spacer

interface, has reached the layer of GNRs. The time range between T_1 and $T_3 = T_1 + T_2 = 328$ ps corresponds to the time over which GNRs are exposed to the propagating strain pulse. During this time, the negative signal in the ΔR/R at 630 nm shows a shift towards higher wavelength. This feature is related to the response of GNRs to the hyper-sound wave by timing of the response. Our interpretation of the physics behind this process is explained in detail in the discussion section. The buffer layer of PSS/PAH in this sample allows us to distinguish features related to the response of GNRs. The plot of the relative change of the transient transmission is placed in the appendix (Figure 11-7).

Sample 22 In order to crosscheck the dynamics related to the GNRs observed in the previous sample (Sample 52), I have designed another sample with different type of GNRs and with different thicknesses of the transducer and spacer layer. Due to the different thicknesses, the timing of the described characteristic features is expected to be different. Due to the different type of the GNRs used in this sample, the position of the spectral features related to the interaction between GNRs and the strain wave is expected to be at a different wavelength in comparison to the previous sample. This sample has a reduced spacer thickness with respect to the previous structure in order to shorten the delay before the strain pulse arrival to the layer of GNRs. However, in order to maintain the same conditions of the interaction between GNRs and the strain wave the spacer layer cannot be left out completely. The structure of sample 22 is the following: Quartz – 120 dl PAzo/PAH – 30 dl PSS/PAH – GNRs type II. The thicknesses of the transducer, the spacer, and the type of GNRs are chosen in order to avoid the superimposing of the spectral feature in the transient spectrum of ΔR/R.

Figure 7-7 a) shows the static absorption and reflection spectra. The static reflection spectrum shows the thin film interference. The absorption spectrum shows the position of the longitudinal plasmon resonance of GNRs. The spectrum shows two plasmon resonances at ≈ 630 and at ≈ 710 nm. The resonance at higher wavelength is likely to be caused by the clustering of GNRs. The relative change of the transient reflection is presented in

Figure 7-7 b). The observed features are the same as for sample 52: thin film interference, Brillouin scattering, and the GNRs response to the strain wave. For this sample, the response of the transverse mode of the plasmon resonance is clearly visible. At wavelength around 525 nm the positive signal of ΔR/R shows only a weak shift to higher wavelengths. This is due to the relatively low sensitivity of the transverse mode of the plasmon resonance[80,102,103].

The main difference between this sample and the previous one (sample 52) is the timing of the GNRs response. Because the spacer layer between the transducer and GNRs is reduced in this sample, the strain wave reached the GNRs earlier and the shift of the signal related to the longitudinal plasmon resonance occurs earlier. The time difference in the observed features, confirms the assumption that the red shift is indeed a GNRs' related feature. Our interpretation of the physics behind this process is explained in the discussion section. The plot of the relative change of the transient transmission is placed in the appendix (Figure 11-8).

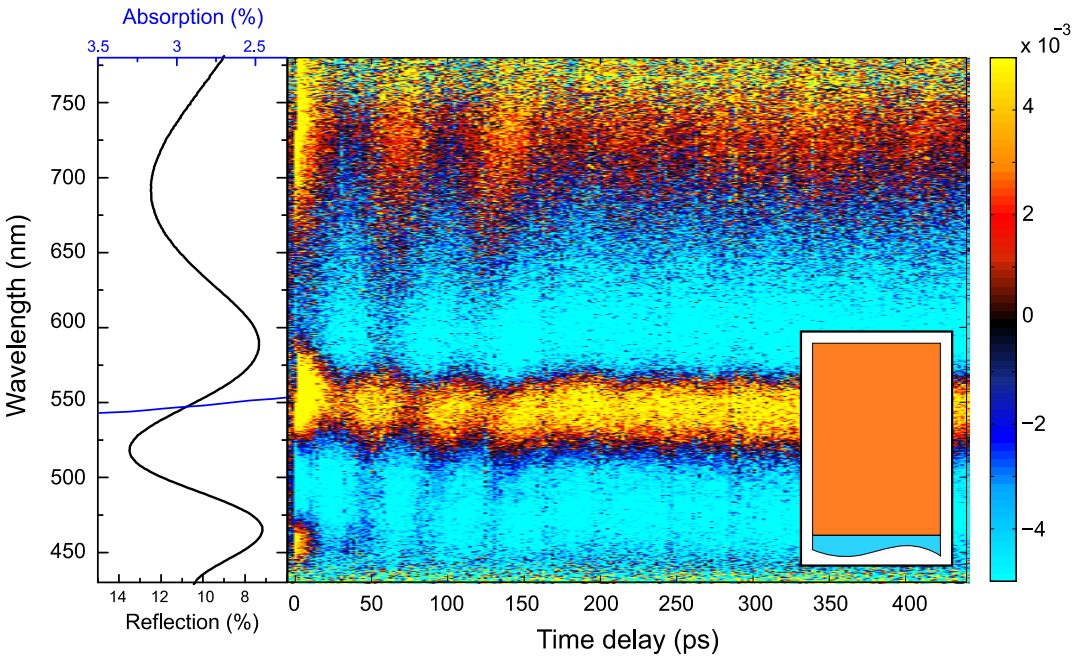

Figure 7-6 The measured static spectrum of reflection (R) and the absorption spectrum constructed as A = 1 –R – T. b) The relative change of the transient reflection for sample 22 (Quartz – 120 dl PAzo/PAH)

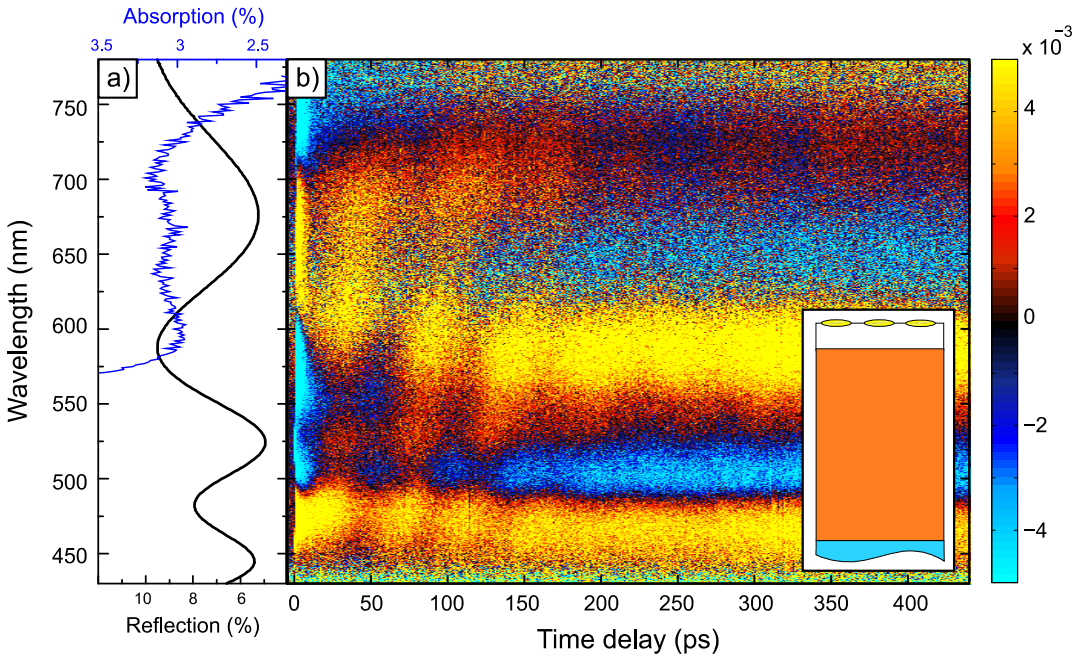

Figure 7-7 The measured static spectrum of reflection (R) and the absorption spectrum constructed as A = 1 –R – T. b) The relative change of the transient reflection for sample 22 (Quartz – 120 dl PAzo/PAH – 30 dl PSS/PAH – GNR II)

Sample 145 In this sample, 4 layers of GNRs type III are embedded in a thick layer of PAzo/PAH. The exact structure of the sample is Quartz – 90 dl PAzo/PAH – (GNR III – 15 dl PAzo/PAH)*3 – GNR III – 60 dl PAzo/PAH. Figure 7-8 a) shows the static absorption and reflection spectra. The static reflection spectrum shows the thin film interference pattern. The absorption spectrum shows the position of the longitudinal plasmon resonance of GNRs, which is strongly shifted to higher wavelengths, because GNRs are embedded in a medium with a relatively high refractive index. The transverse mode of the plasmon resonance is hidden by the strong absorption of Azobenzene. Figure 7-2 b) shows the relative change of the transient reflection. In the wavelength range 450-650 nm one can see the shift of the thin film interference pattern, similar to the previous samples. At 550 nm the signal related to the transverse mode of the plasmon resonance is visible. Besides the dynamics at very early times (~10 ps) it remains in the same position, similar to the dynamics of the transverse plasmon resonance in the ΔR/R of the previous sample (sample 22). Thin film interference and the Brillouin scattering are observed in the relative change of the transient reflection. The dynamics of the longitudinal plasmon resonance of the embedded GNRs is discussed in chapter 8. The plot of the relative change of the transient transmission is placed in the appendix (Figure 11-9).

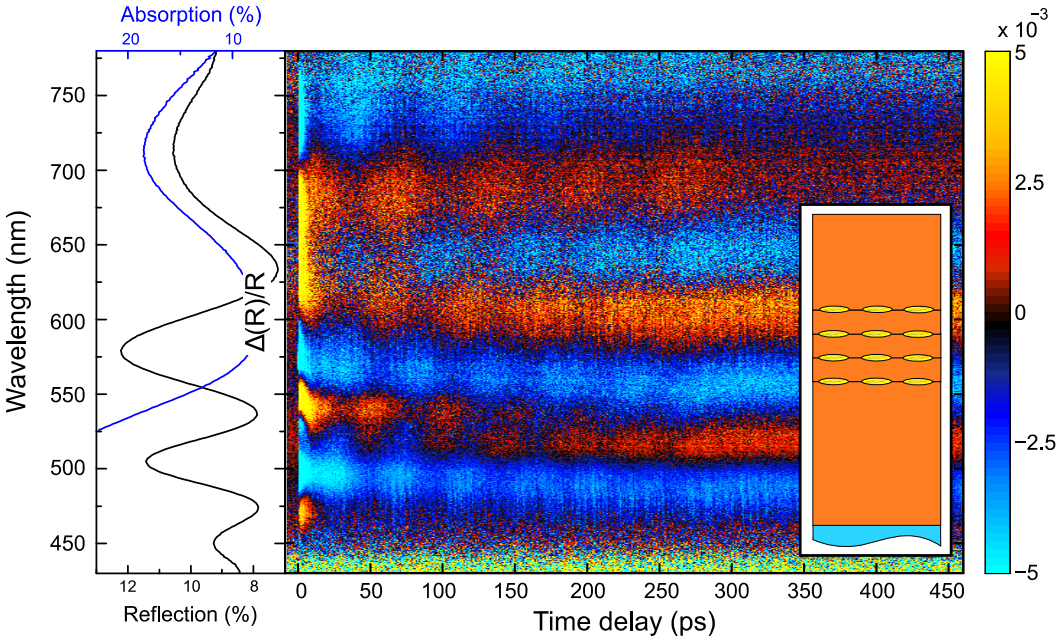

Figure 7-8 The measured static spectrum of reflection (R) and the absorption spectrum constructed as A = 1 –R – T. b) The relative change of the transient reflection for sample 45 (Quartz – 90 dl PAzo/PAH – (GNR III – 15 dl PAzo/PAH)*3 – GNR III – 60 dl PAzo/PAH).

8. Discussion

In this chapter we discuss the results presented in the previous sections and will develop a physical model of the observed phenomena. A linear chain model (chapter 2.3.2) is used to guide the intuition and to confirm the observed timescales and sign changes. The simulations are only a first step towards modeling the ultrafast viscoelastic response of the polymer.

8.1. Strain dynamics

In order to analyze the properties of PAzo/PAH as a transducer and additionally to calibration the strain by X-ray experiments (chapter 6.4.2), we have simulated the data from the optical experiments (Figure 6-10). Using Fresnels' equations for a multilayered structure, and treating the propagating strain wave as a reflecting interface (difference of the refractive index), we could reproduce the optical data and retrieve the transient change of the refractive index. A decreased refractive index n_{azo} of Azo-containing polymers for expanded films was already observed by Tanchak et. al[19] on much longer time scales. In their publication the observed decrease of the refractive index of $\Delta n/n$ = - 1% for a relative thickness change of $\Delta d/d$ = + 1.4 %. The ratio between the changes in thickness and refractive index is consistent with our observations on ultrafast time scales: the strain calibrated by X-rays is $\varepsilon = \Delta d/d \sim 5\text{x}10^{-4}$ and the refractive index change, retrieved from the simulations of the optical data (Figure 6-10) is $\Delta n/n = -2.6\text{x}10^{-4}$.

Using the linear-chain model, described in paragraph 2.3.2 we have simulated the strain for sample 35. Figure 8-1 shows four snapshots of the strain front motion at times, at which the main strain-front originating at the surface is in the center of the film. The green shaded area depicts the static strain profile generated by the stress profile assumed in the simulations, according to the approximate penetration depth of about 500 nm for the intense excitation pulses with a wavelength of 398 nm. In the linear regime (Figure 6-1) the penetration depth is less than 250 nm. The lines (red, orange, green, blue) in Fig. 3(c) indicate the time-dependent profile of the coherent bipolar strain pulse. Adding the static (green shaded area) and propagating bipolar strain yield the total transient strain. Initially, it is essentially an expansion wave travelling from the surface to the substrate with a smaller leading compressive part[61]. The reflection of the bipolar strain pulse from the substrate - a material with larger acoustic impedance - conserves its sign. According to the acoustic impedance mismatch, a fraction of $(Z_{poly} - Z_Q)/(Z_{poly}+Z_Q) = 60$ % of the wave is reflected (Table 8-1). After the first reflection (t = 180 ps), the acoustic waveform propagates towards the laser probe-pulse. The refractive index change at the strain front now has the opposite sign, yielding a phase shift of π in the oscillation pattern (Figure 6-10 b). At t = 360 ps the acoustic pulse is reflected at the surface/air interface which reverses the sign of the wave and of the propagation direction. Therefore, no phase shift is observed in the TDBS signal (oscillatory pattern). The third reflection at t = 540 ps is so weak that the signal vanishes in the noise.

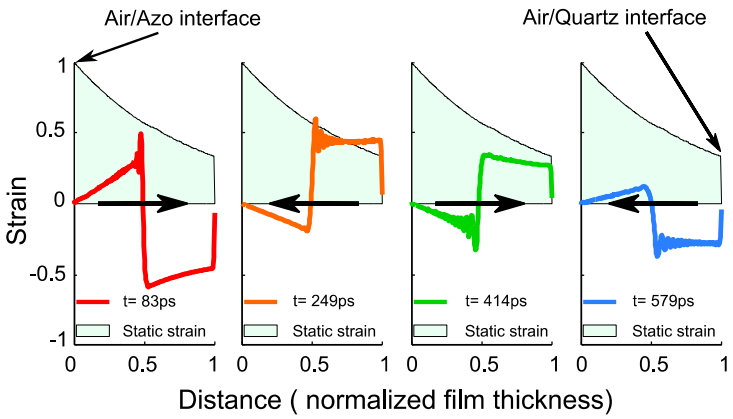

Figure 8-1) A representation of the calculated strain front within the PAzo/PAH (sample 35) at different time delays. The green shaded area corresponds to the static strain in the polymer layer resulting from the optical excitation

Due to the high precision of the Layer-by-layer sample preparation, the thickness of the PAzo/PAH transducer films can be tuned to produce the strain waves in the frequency range 1 -100 GHz. The thickness of the transducer also defines the generated phonon spectrum in the adjacent material (see chapter 2.3.2). By tuning the thickness of the transducer film, one can tune the generated phonon spectrum in the adjacent/investigated material.

Table 8-1 Optical and acoustic properties of the materials used.

Material	Density [kg/m^3]	Sound velocity [nm/ps]	Acoustic impedance Z [10^6 Ns/m^3]	Refractive index @ λ = 600 nm
PSS/PAH	940[69]	3.4	3.1	1.47
PAzo/PAH	Unknown (estimated value 1000)	3.4	3.4	1.67
Quartz	2200[101]	5.8[101]	12.7	1.45[101]
Mica	2700	5.0[104]	13.5	1.56

Values from the literature are indicated by citations. Sound velocities are measured values according to the equation (2-19). Refractive indices are measured by ellipsometry.

8.2. Sensing hyper-sound waves with gold nanorods

The qualitative (chapter 8.1) and quantitative (chapter 4.4) agreement of the simulations in the linear-chain model with the experiments allows us to use it for understanding the interaction between the strain waves and gold nanoparticles.

Figure 8-2 shows schematic representation of the structures for samples 52 and 22 (Figure 7-5 and

Figure 7-7). The inset represents a zoom into the area at the surface. The arrows schematically represent the dynamics of the strain waves. At the (PAzo/PAH)/(PSS/PAH) interface after the excitation, an expansion wave propagates towards the substrate, and a compression wave propagates towards the surface. At the surface, the strain wave is reflected differently: from the (PSS/PAH)/air interface the strain is reflected with a change of sign (case a), whereas the sign of the strain amplitude stays the same when the wave is reflected from a (PSS/PAH)/GNR interface.

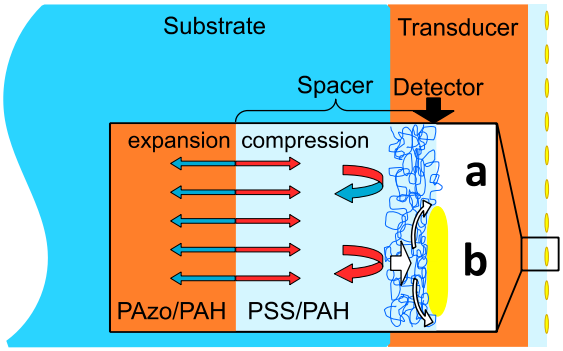

Figure 8-2 A schematic of the sample composed of an Azo-functionalized optoacoustic transducer (PAzo/PAH), a transparent PSS/PAH layer for the free propagation of hyper-sound waves and GNRs on the surface. The arrows schematically represent the dynamics of the strain waves. At the surface in case a), a compression wave reflects from the (PSS/PAH)/air interface with a change of sign, whereas the sign of the strain amplitude stays the same when the wave is reflected from a (PSS/PAH)/GNR interface. This leads to transient tangential pressure within the polyelectrolyte at the interface with the GNRs.

The evolution of the strain pulse for cases a and b was simulated and the results are shown in Figure 8-3. For the case a, when the strain pulse is reflected at the (PSS/PAH)/air interface, for times up to 80 ps the strain front is negative (compression). After the reflection, the strain reverses the sign and becomes an expansion wave and therefore cancels out the compression at the surface at later times. Figure 8-3 b) presents the simulations of the evolution of the strain pulse for the sample with bulk gold on top. The larger acoustic impedance of gold (Z_{GNR}= 63.810^6 Pa*s/m^3 compared to $Z_{PSS/PAH}$= 3.4*10^6 Pa*s/m^3) leads to a reflection without inversion of the sign, therefore the superposition of the incident and the reflected waves leads to an enhanced compressive strain in the out of plane direction. In fact, 87 % of the wave is reflected as a compression wave and 13 % would nominally propagate through the particle. Then these 13 % would reflect from the GNR/air interface with the change of sign and become an expansion wave. In our simulation, we used a very thick gold layer to get rid of the reflection at the surface, because we are convinced that the reflected soundwave will be no plane wave since the soundwave is scattered by the surface curvature of the particle.

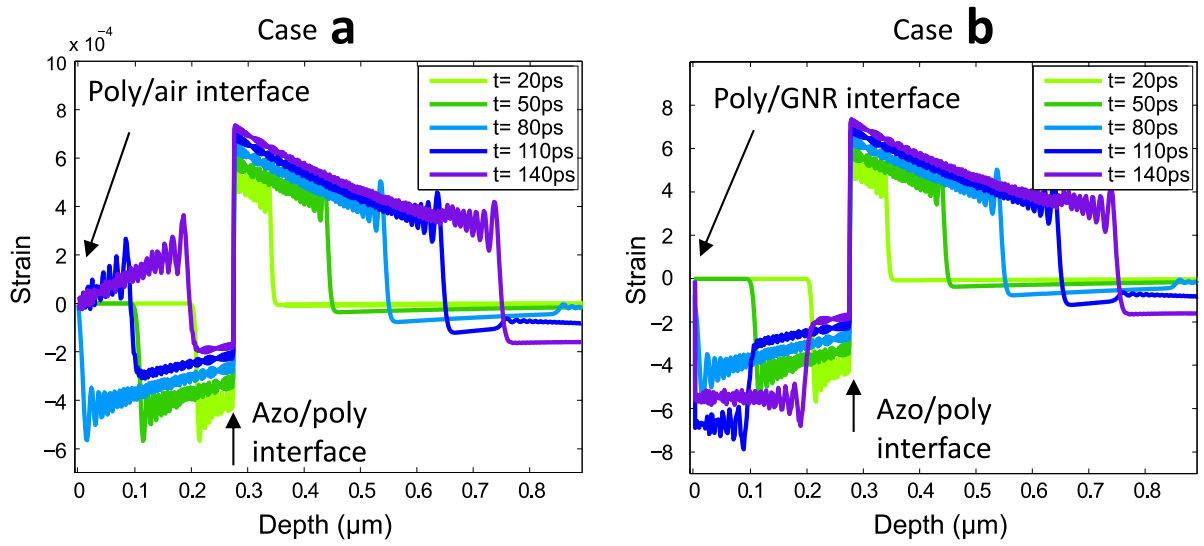

Figure 8-3 The simulation of the strain pulse evolution. The horizontal axis represents the sample depth. z=0 corresponds to the sample surface. The interface between PAH/PSS and PAzo/PAH is at 300 nm. a) Simulations of the strain pulse evolution for sample 52, without gold on top. b) Same structure, however, with bulk gold on top to simulate the strain dynamics at the interface to the gold nanoparticles.

Although this 1D model oversimplifies the interaction of the strain wave with the nanoparticle, we can qualitatively derive an order-of magnitude estimate for the out of plane strain ε, which has previously been calibrated by ultrafast X-ray diffraction[105]. Figure 8-4 a) shows the strain ε_z averaged over the first 30 nm beneath the polymer/air interface ($\varepsilon_{\mathrm{poly/air}}$ - blue line) and beneath the polymer/gold interface ($\varepsilon_{\mathrm{poly/gold}}$ - yellow line). The time of about 300 ps for the decay of $\varepsilon_{\mathrm{poly/gold}}$ is given by the thickness of the PAzo/PAH layer. The strain rises again, when the strain wave reflected from the substrate arrives at the gold layer (~350 - 550 ps). Using the high-frequency elastic constant for PSS/PAH we can translate the strain into an out-of-plane compressive stress σ_x, which will yields a stress with a similar magnitude parallel to the particle interface by virtue of Poisson's effect (Figure 8-4 b). For convenience Figure 8-4 not only plots the strain-difference calculated for the first 30 nm beneath the surface, but also shows the conversion into an ultrafast stress according to $\sigma = Y\varepsilon$, where Y=10.9 GPa/cm^2 is Young's modulus of PAH/PSS at high frequencies. Figure 8-4 c) shows the observed shift of the longitudinal plasmon resonance on the same time axis. The shift is steep, when a large pressure gradient σ_x, forces the polymer to move around the GNR.

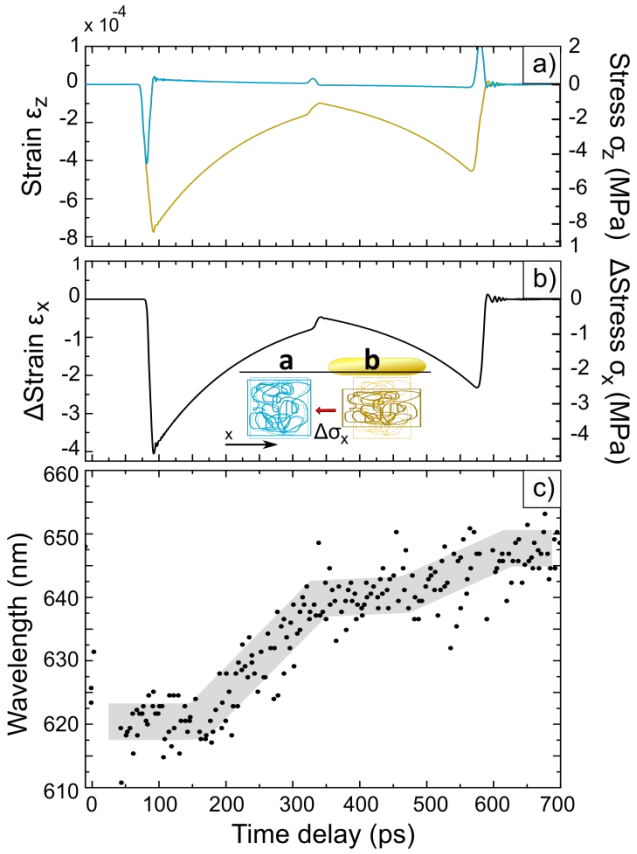

Figure 8-4 a) Integrated stress σ_z and strain ε_z averaged over the first 30 nm beneath the surface. Blue line corresponds to the case a, according to the schematic in Figure 8-2, and the yellow line corresponds to the case b. b) The graph shows the in-plane differences of the stress $\Delta\sigma_x$ and the strain $\Delta\varepsilon_x$ at the polymer/gold and polymer/air interface. The inset visualizes the difference in deformation. c) Trace of the position of the experimentally measured $\Delta R/R_0$ minimum (white arrow in Fig. 2b), related to the longitudinal plasmon resonance of GNRs in Sample 52.

The analysis of the strain in the vicinity of GNRs placed on the surface, leads to the following interpretation of the shift observed in both ΔR/R for sample 52 and 22. We assign the shift of the ΔR/R related to the longitudinal plasmon resonance of GNRs to a viscoelastic dynamic response of the polyelectrolytes near the surface. The induced shift of the PR_L remains for times much longer than the sound pulse is incident on the GNRs. In fact, we have not observed any recovery up to 1ns. On the other hand, we know that the process is reversible since we repeat the experiment at the 5 kHz pulse rate of the laser system. This implies that the modifications around the GNRs relax within 200 μs.

As indicated schematically in Figure 8-2, the incident compressive strain wave is reflected as an expansion wave at the interface to air, which cancels the compressive stress of the incident wave near the surface. At the interface to GNRs (Figure 8-2 case b), the hyper-sound-wave is reflected as a compression wave. Therefore, the incident and reflected waves add up to a large compressive stress in the vicinity of

GNRs. We suggest that this pressure difference (under the gold interface and at the poly/air interface) leads to a deformation of polyelectrolyte towards the ends of the GNR, which in turn leads to a red shift according to effective medium models[21]. As the pressure-difference ceases after few nanoseconds, a viscoelastic deformation brings the PSS/PAH polyelectrolyte back to the starting configuration within the repetition rate of the experiment. We emphasize that no light is absorbed by the PAH/PSS and therefore the response of GNRs on the surface can be safely attributed to the ultrafast pressure step.

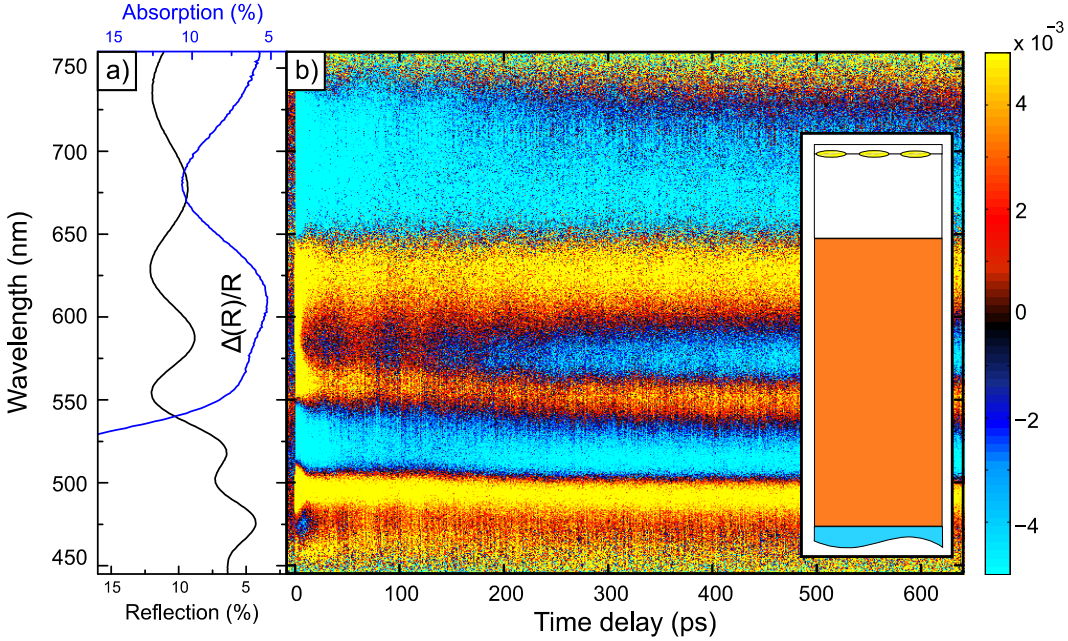

Figure 8-5 The measured static spectrum of reflection (R) and the absorption spectrum constructed as A = 1 –R – T. b) The relative change of the transient reflection for sample 52 after additional PSS/PAH on the top of the structure (Quartz – 180 dl PAzo/PAH – 70 dl PSS/PAH – GNR IV – 8 dl PSS/PAH)

In order to crosscheck the presented assumption I have added extra 8 dl of PSS/PAH on the top of sample 52. The static reflection and absorption spectra of sample 52 after the coverage are shown in Figure 8-5 a). The thin film interference pattern in the reflection spectrum is slightly shifted comparing to the uncovered sample, due to the slight change of the total thickness. The position of the plasmon resonance in the absorption spectrum is shifted to higher wavelengths, due to the modified dielectric environment of the particle (GNRs are now fully embedded in polymer). Figure 8-5 b) shows the relative change of the transient reflection for sample 52 after the coverage.

In this architecture the interface of (PSS/PAH)/air is moved away from the particles, therefore the low-pressure zone at the ends of GNRs is weaker. Thus, the gradient of the pressure between the zones under the gold particles and at their edges is smaller. Moreover, the material transport around the ends of GNRs is now sterically hindered by the cover layer. The signal, related to the longitudinal resonance, does not show a shift in time. The absence of the shift can be explained by the smaller gradient of the stress under the particles and at their edges, which does not result in the viscoelastic deformation of the polymer

around the GNRs. This confirms the assumption that in samples 52 and 22 the observed shift of the PR_L is cause by the viscoelastic deformation of the polymer around GNRs. The plot of the relative change of the transient transmission for this sample architecture is placed in the appendix (Figure 11-10).

In the case of sample 45, GNRs are embedded into the transparent polymer, while in case of sample 45 they are embedded in the PAzo/PAH film, which absorbs the light of the excitation pulse. Different to the covered version of sample 52, spectral features related to the longitudinal plasmon resonance of GNRs in sample 45 show a shift towards higher wavelengths (Figure 7-8 b). Figure 8-6 shows the time dependent position of the maximum positive change of ΔR/R in the wavelength range 650-769 nm, related to the longitudinal plasmon resonance of GNRs in this sample. Up to 100 ps the peak position remains unchanged. This time corresponds to the time that it takes for a strain wave generated at the (PAzo/PAH)/Air interface to reach the first layer of GNRs. After 100 ps, the position of the peak shifts up to 270 ps, which corresponds to the time that it take for the strain wave generated at the surface to reach the substrate. In this sample structure, the red shift of the PR_L is caused by the change of the refractive index of PAzo/PAH due to the strain wave propagation.

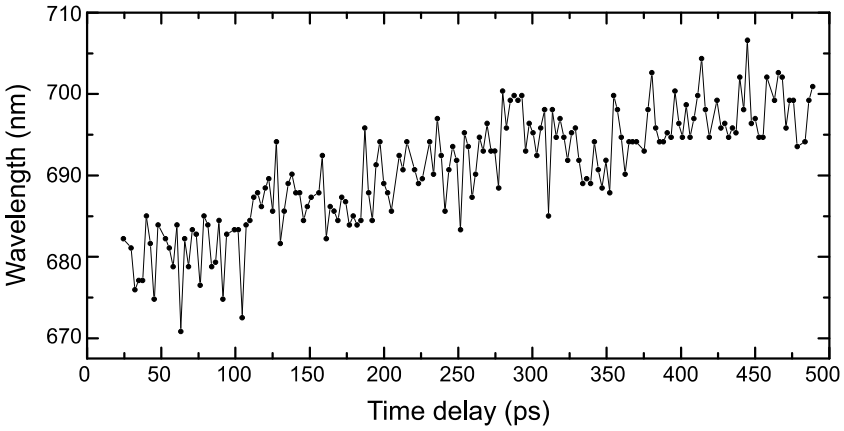

Figure 8-6 The position of the maximum positive change of ΔR/R in the wavelength range 650-769 nm for sample 45 (Quartz – 90 dl PAzo/PAH – (GNR III – 15 dl PAzo/PAH)*3 – GNR III – 60 dl PAzo/PAH).

9. Summary

In the presented work, I have investigated two types of Azobenzene containing polymer film as transducers. Both, Layer-by-layer and "One drop" films were investigated via static and transient pump-probe spectroscopy. By analyzing the time-domain Brillouin scattering (TDBS), we have defined the sound velocity in both polymers to be 3.4±0.3 nm/ps. The analysis of the frequency and the amplitude of the TDBS pattern for different sample architectures allowed us to investigate the reflection of the strain waves from different interfaces (polymer/quartz, polymer/air) and propagation of the strain into soft (polymer) and hard (quartz) adjacent materials. I also showed that the hyper-sound wave is attenuated by scattering of GNRs embedded in polymer. This bears the possibility of sensing the position of nano particles in polymer under the surface.

A shift of the thin film interference related pattern observed in the transient reflection spectra for PAzo/PAH films of different thicknesses was thoroughly analyzed. The observed shift was simulated, and interpreted as the transient change of the thickness and the refractive index of the transducer film under the excitation. The relative transient change of the refractive index retrieved from the optical measurements is $\Delta n/n = -2.6*10^{-4}$.

The strain generated by the Azobenzene-based soft matter transducer has been calibrated by X-ray diffraction. Tracking the position of the Bragg peak of the Mica film with the transducers on the top, allowed us to retrieve the value of the induced strain $\varepsilon = \Delta d/d \sim 5x10^{-4}$ generated by laser pulse with fluence of 4 mJ at 398 nm wavelength. The experimental results were confirmed by a simulation based on the linear-chain-mode.

In order to explore the interaction between GNRs and the hyper-sound waves I have performed a systematic analysis of various sample architectures. Those, which have contributed the most into understanding the phenomena, were presented and analyzed in the thesis. Two samples, with the similar structures (Substrate – transducer – spacer – GNR) showed the shift of the spectroscopic feature related to the longitudinal plasmon resonance. The attribution of the observed shift to the GNR-related signal is confirmed by the different thickness of the sample components and therefore different timing of the feature. The observed shift of the $\Delta R/R$ signal related to the longitudinal plasmon resonance was assigned to the viscoelastic dynamic response of the polyelectrolytes near the surface. We argue that the viscoelastic deformation of the polymer around GNRs is induced by the out of plane difference in strain in the area directly under a particle and next to it. This conclusion is supported by simulations of the strain dynamics. Experimentally this assumption is proven by investigating the same structure, with GNR embedded in PSS/PAH polymer layer. In this case, no shift of the features, related to the longitudinal plasmon resonance, were observed.

Finally, a structure with GNRs embedded into PAzo/PAH polymer was investigated. Spectra features related to the longitudinal plasmon resonance of GNRs showed a red shift, which in this case was interpreted to be driven mostly by the change of the refractive index of the surrounding medium of GNRs.

10. Future Prospects

This work is only a step towards the development of soft matter transducers and a structural analysis of complex soft matter structures. Performing a systematic characterization of the PAzo/PAH transducer, for different fluences, and other parameter will be a natural step forward. The investigation of the generated phonon spectra in adjacent materials depending on the transducers and capping layer thicknesses[85] will develop a convenient tool for the further applications of the proposed transducers.

Designing new sample architectures for a more informative analysis of the structures is certainly a promising direction of the development for the multidisciplinary research. One of the advantages of a transducer made of polyelectrolytes is a possibility to create local transducers on nanometer scale, which would allow us to investigate elastic properties of single nano-objects such as gold nanorods and their functionalized shells. One of the proposed structures could be the direct coverage of gold nanoparticles, by a transducer (Figure 10-1 a). Another possible application is to investigate a single nano-object under high-pressure conditions by building a transducer lens (Figure 10-1 b).

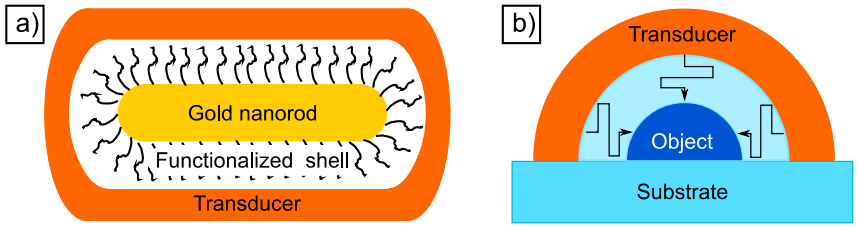

Figure 10-1 a) A schematic of a single nanorods, functionalized and covered by a transducer for the analysis of the functionalized shell properties as well as the interface between GNR and shell. b) A schematic of a nano-object investigated under high pressure, created by a soft-matter transducer lens.

References

1. Devos, A. Colored ultrafast acoustics: from fundamentals to applications. *Ultrasonics* **56,** 90–97 (2015).
2. Bargheer, M. *et al.* Coherent atomic motions in a nanostructure studied by femtosecond X-ray diffraction. *Science* **306,** 1771–1773 (2004).
3. Bojahr, A. *et al.* Brillouin scattering of visible and hard X-ray photons from optically synthesized phonon wavepackets. *Opt Express* **21,** 21188–21197 (2013).
4. Schick, D. *et al.* Following Strain-Induced Mosaicity Changes of Ferroelectric Thin Films by Ultrafast Reciprocal Space Mapping. *Phys. Rev. Lett.* **110,** 95502 (2013).
5. Lomonosov, A. M. *et al.* Nanoscale noncontact subsurface investigations of mechanical and optical properties of nanoporous low-k material thin film. *ACS nano* **6,** 1410–1415 (2012).
6. Ayouch, A. *et al.* Elasticity of an assembly of disordered nanoparticles interacting via either van der Waals-bonded or covalent-bonded coating layers. *ACS nano* **6,** 10614–10621 (2012).
7. Danworaphong, S. *et al.* Three-dimensional imaging of biological cells with picosecond ultrasonics. *Applied Physics Letters* **106,** 163701 (2015).
8. Dehoux, T. *et al.* All-optical broadband ultrasonography of single cells. *Scientific reports* **5,** 8650 (2015).
9. Gadalla, A., Dehoux, T. & Audoin, B. Transverse mechanical properties of cell walls of single living plant cells probed by laser-generated acoustic waves. Planta. *Planta* **239,** 1129–1137 (2014).
10. Rossignol, C. *et al.* In Vitro picosecond ultrasonics in a single cell. *Appl. Phys. Lett.* **93,** 123901 (2008).
11. Decher, G., Hong, J. D. & Schmitt, J. Buildup of ultrathin multilayer films by a self-assembly process. III. Consecutively alternating adsorption of anionic and cationic polyelectrolytes on charged surfaces. *Thin Solid Films* **210-211,** 831–835 (1992).
12. Decher, G. & Schlenoff, J. B. *Multilayer Thin Films: Sequential Assembly of Nanocomposite Materials* (Wiley, 2006).
13. Bandara, H. M. D. & Burdette, S. C. Photoisomerization in different classes of azobenzene. *Chemical Society reviews* **41,** 1809–1825 (2012).
14. Quick, M. *et al.* Photoisomerization dynamics and pathways of trans- and cis-azobenzene in solution from broadband femtosecond spectroscopies and calculations. *J Phys Chem B* **118,** 8756–8771 (2014).
15. Lednev, I. K., Ye, T.-Q., Hester, R. E. & Moore, J. N. Femtosecond Time-Resolved UV−Visible Absorption Spectroscopy of trans -Azobenzene in Solution. *J. Phys. Chem.* **100,** 13338–13341 (1996).

16. Yadavalli, N. S., Korolkov, D., Moulin, J.-F., Krutyeva, M. & Santer, S. Probing opto-mechanical stresses within azobenzene-containing photosensitive polymer films by a thin metal film placed above. *ACS Appl Mater Interfaces* **6,** 11333–11340 (2014).

17. Ikeda, T. & Tsutsumi, O. Optical switching and image storage by means of azobenzene liquid-crystal films. *Science* **268,** 1873–1875 (1995).

18. Nedelchev, L., Nazarova, D., Mateev, G. & Berberova, N. *Birefringence induced in azopolymer (PAZO) films with different thickness* (International Society for Optics and Photonics, 2015).

19. Tanchak, O. M. & Barrett, C. J. Light-Induced Reversible Volume Changes in Thin Films of Azo Polymers. The Photomechanical Effect. *Macromolecules* **38,** 10566–10570 (2005).

20. Kiel, M., Klötzer, M., Mitzscherling, S. & Bargheer, M. Measuring the range of plasmonic interaction. *Langmuir* **28,** 4800–4804 (2012).

21. Mitzscherling, S., Cui, Q., Koopman, W. & Bargheer, M. Dielectric function of two-phase colloid-polymer nanocomposite. *Physical chemistry chemical physics : PCCP* **17,** 29465–29474 (2015).

22. Zijlstra, P., Paulo, P. M. R. & Orrit, M. Optical detection of single non-absorbing molecules using the surface plasmon resonance of a gold nanorod. *Nat Nanotechnol* **7,** 379–382 (2012).

23. Ni, W., Yang, Z., Chen, H., Li, L. & Wang, J. Coupling between molecular and plasmonic resonances in freestanding dye-gold nanorod hybrid nanostructures. *J. Am. Chem. Soc.* **130,** 6692–6693 (2008).

24. Focsan, M., Gabudean, A. M., Vulpoi, A. & Astilean, S. Controlling the Luminescence of Carboxyl-Functionalized CdSe/ZnS Core–Shell Quantum Dots in Solution by Binding with Gold Nanorods. *J. Phys. Chem. C* **118,** 25190–25199 (2014).

25. Rex, M., Hernandez, F. E. & Campiglia, A. D. Pushing the limits of mercury sensors with gold nanorods. *Anal. Chem.* **78,** 445–451 (2006).

26. Ungureanu, C. *et al.* Light interactions with gold nanorods and cells: implications for photothermal nanotherapeutics. *Nano letters* **11,** 1887–1894 (2011).

27. Huang, X., El-Sayed, I. H., Qian, W. & El-Sayed, M. A. Cancer cell imaging and photothermal therapy in the near-infrared region by using gold nanorods. *Journal of the American Chemical Society* **128,** 2115–2120 (2006).

28. Demselben. Ueber das Stickstoffbenzid. *Annalen der Pharmacie* **12,** 311–314 (1834).

29. Merino, E. & Ribagorda, M. Control over molecular motion using the cis-trans photoisomerization of the azo group. *Beilstein J Org Chem* **8,** 1071–1090 (2012).

30. Di Florio, G., Brundermann, E., Yadavalli, N. S., Santer, S. & Havenith, M. Graphene multilayer as nanosized optical strain gauge for polymer surface relief gratings. *Nano letters* **14,** 5754–5760 (2014).

31. Goldenberg, L. M., Lisinetskii, V., Gritsai, Y., Stumpe, J. & Schrader, S. Second order DFB lasing using reusable grating inscribed in azobenzene-containing material. *Opt. Mater. Express* **2,** 11 (2012).

32. Fujii, T. *et al.* Molecular dynamics in azobenzene liquid crystal polymer films measured by time-resolved techniques. *Physical chemistry chemical physics : PCCP* **16,** 10485–10490 (2014).

33. Yu, Y., Nakano, M. & Ikeda, T. Photomechanics: directed bending of a polymer film by light. *Nature* **425,** 145 (2003).

34. Garcia-Amorós, J., Sánchez-Ferrer, A., Massad, W. A., Nonell, S. & Velasco, D. Kinetic study of the fast thermal cis-to-trans isomerisation of para-, ortho- and polyhydroxyazobenzenes. *Phys. Chem. Chem. Phys.* **12,** 13238 (2010).

35. Bahrenburg, J., Röttger, K., Siewertsen, R., Renth, F. & Temps, F. Sequential photoisomerisation dynamics of the push–pull azobenzene Disperse Red 1. *Photochem. Photobiol. Sci.* **11,** 1210 (2012).

36. Nägele, T., Hoche, R., Zinth, W. & Wachtveitl, J. Femtosecond photoisomerization of cis-azobenzene. *Chemical Physics Letters* **272,** 489–495 (1997).

37. Satzger, H., Root, C. & Braun, M. Excited-State Dynamics of trans - and cis -Azobenzene after UV Excitation in the $\pi\ \pi^*$ Band. *J. Phys. Chem. A* **108,** 6265–6271 (2004).

38. Böckmann, M., Doltsinis, N. L. & Marx, D. Enhanced photoswitching of bridged azobenzene studied by nonadiabatic ab initio simulation. *J. Chem. Phys.* **137,** 22A505 (2012).

39. Jiang, C. W., Xie, R. H., Li, F. L. & Allen, R. E. Comparative studies of the trans-cis photoisomerizations of azobenzene and a bridged azobenzene. *The journal of physical chemistry. A* **115,** 244–249 (2011).

40. Ruiz, D. S., Cembran, A., Garavelli, M., Olivucci, M. & Fuss, W. Structure of the conical intersections driving the cis-trans photoisomerization of conjugated molecules. *Photochemistry and photobiology* **76,** 622–633 (2002).

41. Fujino, T., Arzhantsev, S. Y. & Tahara, T. Femtosecond Time-Resolved Fluorescence Study of Photoisomerization of trans -Azobenzene. *J. Phys. Chem. A* **105,** 8123–8129 (2001).

42. Chang, C. W., Lu, Y. C., Wang, T. T. & Diau, E. W. Photoisomerization dynamics of azobenzene in solution with S1 excitation: a femtosecond fluorescence anisotropy study. *Journal of the American Chemical Society* **126,** 10109–10118 (2004).

43. Lednev, I. K. *et al.* Femtosecond time-resolved UV-visible absorption spectroscopy of trans-azobenzene: dependence on excitation wavelength. *Chemical Physics Letters* **290,** 68–74 (1998).

44. Fujino, T. & Tahara, T. Picosecond Time-Resolved Raman Study of trans -Azobenzene. *J. Phys. Chem. A* **104,** 4203–4210 (2000).

45. Satzger, H. *et al.* Fluorescence spectra of trans- and cis-azobenzene – emission from the Franck–Condon state. *Chemical Physics Letters* **372,** 216–223 (2003).

46. Rau, H. & Yu-Quan, S. Photoisomerization of sterically hindered azobenzenes. *Journal of Photochemistry and Photobiology A: Chemistry* **42,** 321–327 (1988).

47. Nataraja Sekhar Yadavalli,Felix Linde,Alexey Kopyshev,Svetlana A Santer. Soft Matter Beats Hard Matter: Rupturing of Thin Metallic Films Induced by Mass Transport in Photosensitive Polymer Films. *ACS Appl Mater Interfaces* **5,** 7743–7747 (2013).

48. Di Florio, G., Bründermann, E., Yadavalli, N. S., Santer, S. & Havenith, M. Polarized 3D Raman and nanoscale near-field optical microscopy of optically inscribed surface relief gratings: chromophore orientation in azo-doped polymer films. *Soft Matter* **10,** 1544–1554 (2014).

49. Hartland, G. V. Optical studies of dynamics in noble metal nanostructures. *Chem Rev* **111,** 3858–3887 (2011).

50. Johnson, P. B. & Christy, R. W. Optical Constants of the Noble Metals. *Phys. Rev. B* **6,** 4370–4379 (1972).

51. Coronado, E. A. & Schatz, G. C. Surface plasmon broadening for arbitrary shape nanoparticles. A geometrical probability approach. *J. Chem. Phys.* **119,** 3926 (2003).

52. Bohren, C. F. & Huffman, D. R. *Absorption and scattering of light by small particles* (Wiley, New York, 1983).

53. Kreibig, U. & Vollmer, M. *Optical properties of metal clusters* (Springer, Berlin, New York, 1995).

54. Gans, R. Über die Form ultramikroskopischer Silberteilchen. *Ann. Phys.* **352,** 270–284 (1915).

55. Voisin, C., Christofilos, D., Del Fatti, N. & Vallée, F. Environment effect on the acoustic vibration of metal nanoparticles. *Physica B: Condensed Matter* **316-317,** 89–94 (2002).

56. Sun, C.-K., Vallée, F., Acioli, L. H., Ippen, E. P. & Fujimoto, J. G. Femtosecond-tunable measurement of electron thermalization in gold. *Phys. Rev. B* **50,** 15337–15348 (1994).

57. Voisin, C. *et al.* Ultrafast electron-electron scattering and energy exchanges in noble-metal nanoparticles. *Phys. Rev. B* **69,** 195416 (2004).

58. Bigot, J.-Y., Halté, V., Merle, J.-C. & Daunois, A. Electron dynamics in metallic nanoparticles. *Chemical Physics* **251,** 181–203 (2000).

59. Hu, M. *et al.* Vibrational response of nanorods to ultrafast laser induced heating: theoretical and experimental analysis. *J. Am. Chem. Soc.* **125,** 14925–14933 (2003).

60. Gaal, P. *et al.* Time-domain sampling of x-ray pulses using an ultrafast sample response. *Appl. Phys. Lett.* **101,** 243106 (2012).

61. Schick, D. *et al.* Ultrafast lattice response of photoexcited thin films studied by X-ray diffraction. *Structural Dynamics* **1,** 64501 (2014).

62. Herzog, M. *et al.* Analysis of ultrafast X-ray diffraction data in a linear-chain model of the lattice dynamics. *Appl. Phys. A* **106,** 489–499 (2012).

63. Schick, D. *et al.* udkm1Dsim—A simulation toolkit for 1D ultrafast dynamics in condensed matter. *Computer Physics Communications* **185,** 651–660 (2014).

64. Bojahr, A. Dissertation. Universität Potsdam, 2016. http://www.udkm.physik.uni-potsdam.de/publications.

65. Sau, T. K. & Murphy, C. J. Seeded high yield synthesis of short Au nanorods in aqueous solution. *Langmuir* **20,** 6414–6420 (2004).

66. Decher, G. & Schmitt, J. in *Trends in Colloid and Interface Science VI,* edited by C. Helm, M. Lösche & H. Möhwald (Steinkopff1992), pp. 160–164.

67. Chiarelli, P. A. *et al.* Controlled Fabrication of Polyelectrolyte Multilayer Thin Films Using Spin-Assembly. *Adv. Mater.* **13,** 1167–1171 (2001).

68. Chiarelli, P. A. *et al.* Polyelectrolyte Spin-Assembly. *Langmuir* **18,** 168–173 (2002).

69. Haberska, K. & Ruzgas, T. Polymer multilayer film formation studied by in situ ellipsometry and electrochemistry. *Bioelectrochemistry (Amsterdam, Netherlands)* **76,** 153–161 (2009).

70. Izquierdo, A., Ono, S. S., Voegel, J.-C., Schaaf, P. & Decher, G. Dipping versus spraying: exploring the deposition conditions for speeding up layer-by-layer assembly. *Langmuir* **21,** 7558–7567 (2005).

71. Lvov, Y., Decher, G. & Moehwald, H. Assembly, structural characterization, and thermal behavior of layer-by-layer deposited ultrathin films of poly(vinyl sulfate) and poly(allylamine). *Langmuir* **9,** 481–486 (1993).

72. Zhang, J.-y., Huang, J. Y., Wang, H., Wong, K. S. & Wong, G. K. Second-harmonic generation from regeneratively amplified femtosecond laser pulses in BBO and LBO crystals. *J. Opt. Soc. Am. B* **15,** 200 (1998).

73. Brodeur, A. & Chin, S. L. Ultrafast white-light continuum generation and self-focusing in transparent condensed media. *J. Opt. Soc. Am. B* **16,** 637 (1999).

74. Shen, Y. R. & Yang, G.-Z. *Theory of Self-Phase Modulation and Spectral Broadening* (Springer New York, 2006).

75. Wang, Q. Z., Ho, P. P. & Alfano, R. R. *Supercontinuum Generation in Condensed Matter* (Springer New York, 2006).

76. Schick, D. *et al.* Normalization schemes for ultrafast x-ray diffraction using a table-top laser-driven plasma source. *The Review of scientific instruments* **83,** 25104 (2012).

77. Zamponi, F. *et al.* Femtosecond hard X-ray plasma sources with a kilohertz repetition rate. Applied Physics A. *Appl. Phys. A* **96,** 51–58 (2009).

78. Kedem, O., Tesler, A. B., Vaskevich, A. & Rubinstein, I. Sensitivity and optimization of localized surface plasmon resonance transducers. *ACS nano* **5,** 748–760 (2011).

79. Kelly, K. L., Coronado, E., Zhao, L. L. & Schatz, G. C. The Optical Properties of Metal Nanoparticles. The Influence of Size, Shape, and Dielectric Environment. *J. Phys. Chem. B* **107,** 668–677 (2003).

80. Link, S., Mohamed, M. B. & El-Sayed, M. A. Simulation of the Optical Absorption Spectra of Gold Nanorods as a Function of Their Aspect Ratio and the Effect of the Medium Dielectric Constant. *J. Phys. Chem. B* **103,** 3073–3077 (1999).

81. Sýkora, D. *et al.* Application of gold nanoparticles in separation sciences. *J Sep Sci* **33,** 372–387 (2010).

82. Huang, J., Jackson, K. S. & Murphy, C. J. Polyelectrolyte wrapping layers control rates of photothermal molecular release from gold nanorods. *Nano letters* **12,** 2982–2987 (2012).

83. Vigderman, L., Khanal, B. P. & Zubarev, E. R. Functional Gold Nanorods: Synthesis, Self-Assembly, and Sensing Applications. *Advanced Materials* **24,** 4811–4841 (2012).

84. A. von Reppert. Bachelor Thesis. Universität Potsdam, 2012. http://www.udkm.physik.uni-potsdam.de/publications.

85. M. Sander. Diplomarbeit. Universität Potsdam, 2013. http://www.udkm.physik.uni-potsdam.de/publications.

86. S. Mitzscherling. Dissertation. Universität Potsdam, 2015. http://www.udkm.physik.uni-potsdam.de/publications.

87. Cembran, A., Bernardi, F., Garavelli, M., Gagliardi, L. & Orlandi, G. On the Mechanism of the cis−trans Isomerization in the Lowest Electronic States of Azobenzene. S 0 , S 1 , and T 1. *J. Am. Chem. Soc.* **126,** 3234–3243 (2004).

88. Choi, B.-Y. Conformational Molecular Switch of the Azobenzene Molecule: A Scanning Tunneling Microscopy Study. *Phys. Rev. Lett.* **96,** 156106 (2006).

89. Joshi, G. K. *et al.* Ultrasensitive photoreversible molecular sensors of azobenzene-functionalized plasmonic nanoantennas. *Nano letters* **14,** 532–540 (2014).

90. Han, J. *et al.* Layer-by-layer ultrathin films of azobenzene-containing polymer/layered double hydroxides with reversible photoresponsive behavior. *J Phys Chem B* **114,** 5678–5685 (2010).

91. Ichimura, K. Light-Driven Motion of Liquids on a Photoresponsive Surface. *Science* **288,** 1624–1626 (2000).

92. Saremi, F. & Tieke, B. Photoinduced Switching in Self-Assembled Multilayers of an Azobenzene Bolaamphiphile and Polyelectrolytes. *Adv. Mater.* **10,** 389–391 (1998).

93. Koshima, H., Ojima, N. & Uchimoto, H. Mechanical motion of azobenzene crystals upon photoirradiation. *J. Am. Chem. Soc.* **131,** 6890–6891 (2009).

94. Zhang, Y., Ma, Y. & Sun, J. Reversible actuation of polyelectrolyte films: expansion-induced mechanical force enables cis-trans isomerization of azobenzenes. *Langmuir* **29,** 14919–14925 (2013).

95. Ube, T., Takado, K. & Ikeda, T. Photomobile materials with interpenetrating polymer networks composed of liquid-crystalline and amorphous polymers. *J. Mater. Chem. C* **3,** 8006–8009 (2015).

96. Goldenberg, L. M., Kulikovska, O. & Stumpe, J. Thermally stable holographic surface relief gratings and switchable optical anisotropy in films of an azobenzene-containing polyelectrolyte. *Langmuir : the ACS journal of surfaces and colloids* **21,** 4794–4796 (2005).

97. Ferreira, Q. *et al.* Influence of ionic interactions on the photoinduced birefringence of poly1-4-(3-carboxy-4 hydroxyphenylazo) benzene sulfonamido-1,2-ethanediyl, sodium salt films. *Journal of nanoscience and nanotechnology* **7,** 2659–2666 (2007).

98. Lednev, I. K. *et al.* Femtosecond time-resolved UV-visible absorption spectroscopy of trans-azobenzene. Dependence on excitation wavelength. *Chemical Physics Letters* **290,** 68–74 (1998).

99. Abbas, A. *et al.* Picosecond time resolved opto-acoustic imaging with 48 MHz frequency resolution. *Optics express* **22,** 7831–7843 (2014).

100. Dehoux, T. *et al.* Probing single-cell mechanics with picosecond ultrasonics. *Ultrasonics* **56,** 160–171 (2015).

101. Zha, C.-s., Hemley, R. J., Mao, H.-k., Duffy, T. S. & Meade, C. Acoustic velocities and refractive index of SiO2 glass to 57.5 GPa by Brillouin scattering. *Phys. Rev. B* **50,** 13105–13112 (1994).

102. Mohamed, M. B., Ismail, K. Z., Link, S. & El-Sayed, M. A. Thermal Reshaping of Gold Nanorods in Micelles. *J. Phys. Chem. B* **102,** 9370–9374 (1998).

103. Yu, Chang, S.-S., Lee, C.-L. & Wang, C. R. C. Gold Nanorods. Electrochemical Synthesis and Optical Properties. *J. Phys. Chem. B* **101,** 6661–6664 (1997).

104. Cebula, D. J. Observation of Longitudinal Acoustic Phonons in Layer-Silicates by Neutron Inelastic Scattering. *Clay Minerals* **17,** 195–200 (1982).

105. Pavlenko, E. S. *et al.* Azobenzene - functionalized polyelectrolyte nanolayers as ultrafast optoacoustic transducers. *Nanoscale* (2016).

11. Appendix

This chapter contains the data, which were measured for the longer delay times for sample 17, and the data that were used for cross-check of the experimental results, discussed in the main body of the thesis.

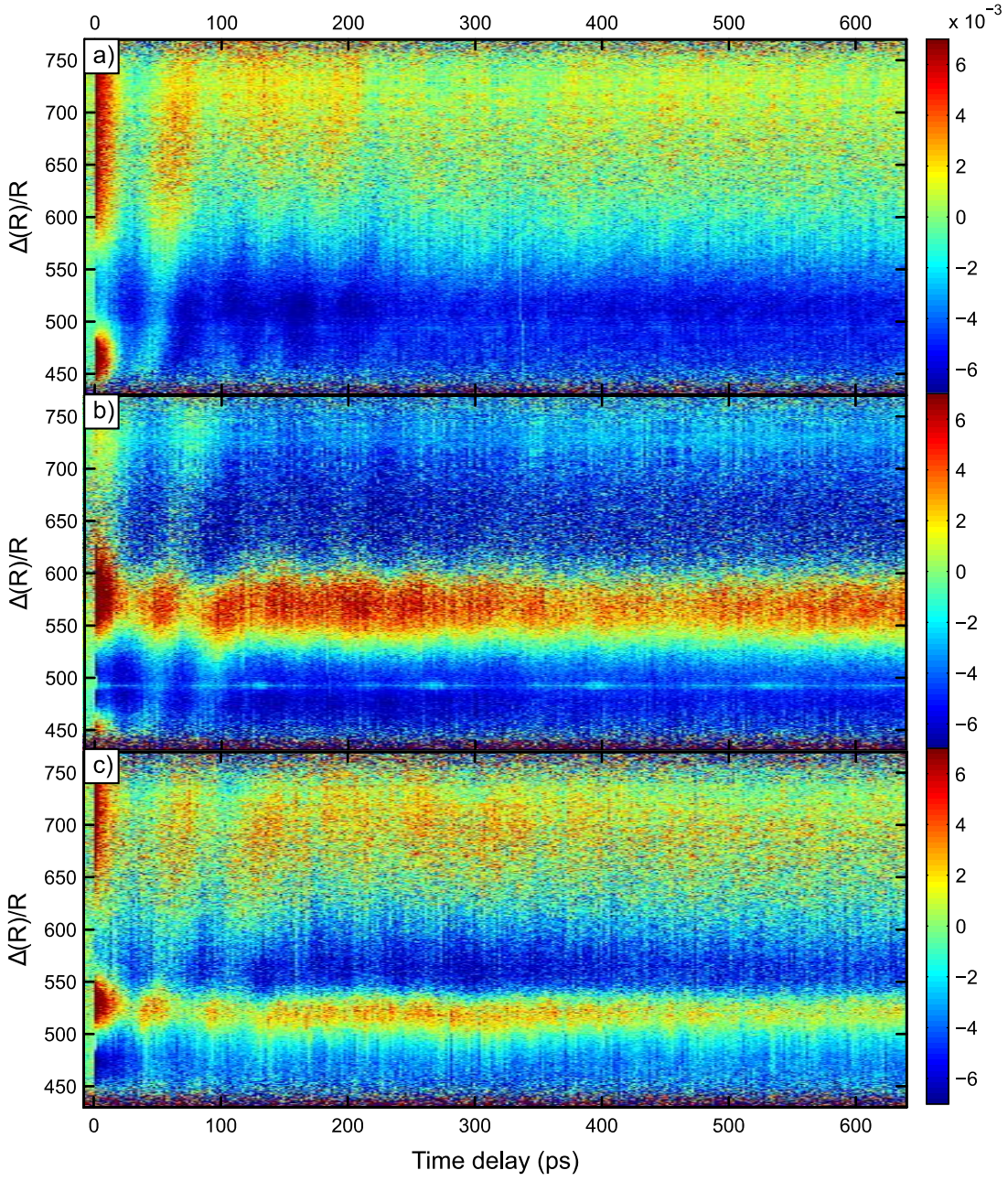

Figure 11-1 Relative change of the transient reflection for sample 17 for different thicknesses. a) 282nm, b) 423nm) 564nm. (See the discussion in chapter 6.2.2)

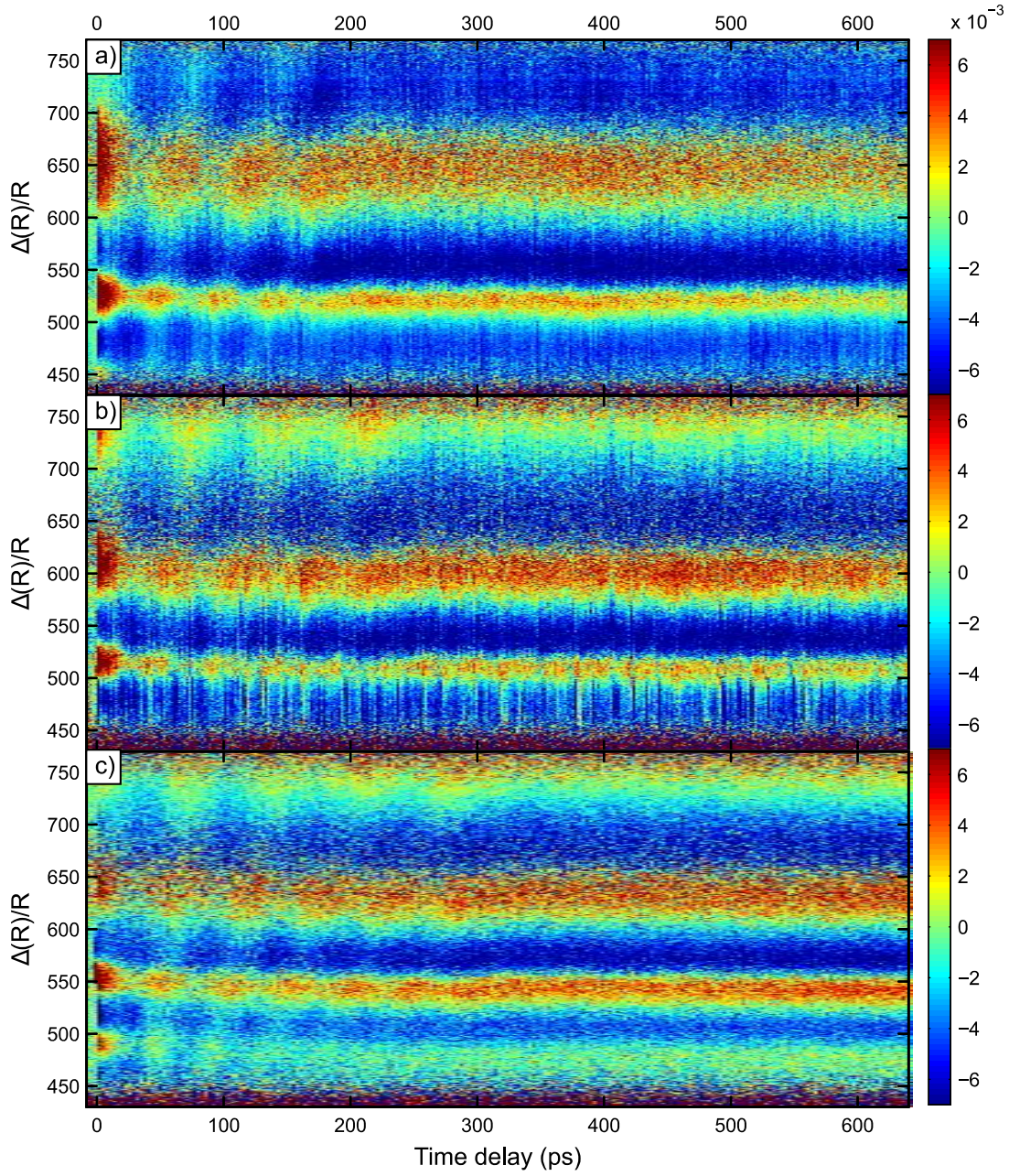

Figure 11-2 Relative change of the transient reflection for sample 17 for different thicknesses. a) 705nm, b) 846nm) 1081nm. (See the discussion in chapter 6.2.2)

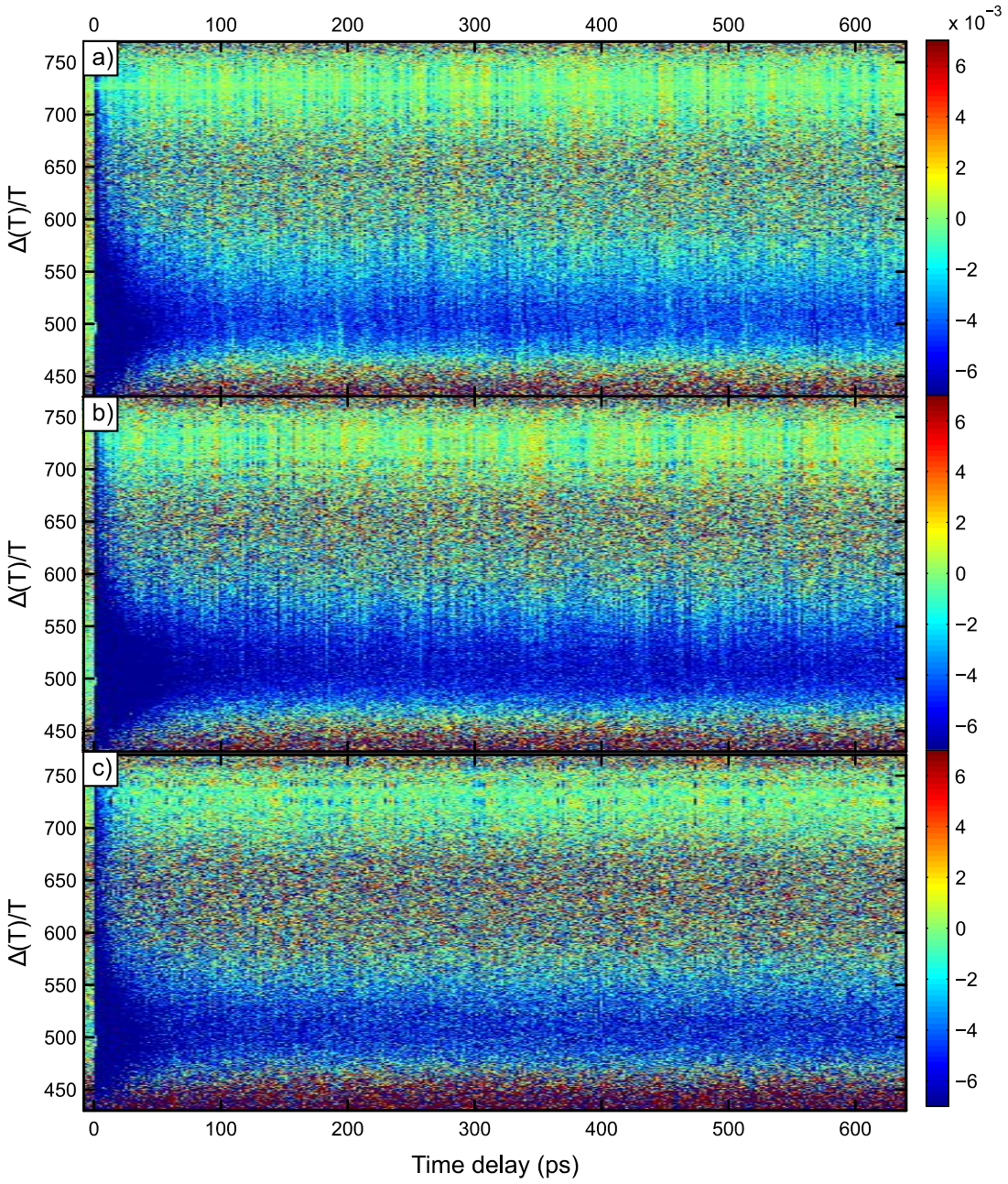

Figure 11-3 Relative change of the transient transmission for sample 17 for different thicknesses. a) 282nm, b) 423nm) 564nm. (See the discussion in chapter 6.2.2)

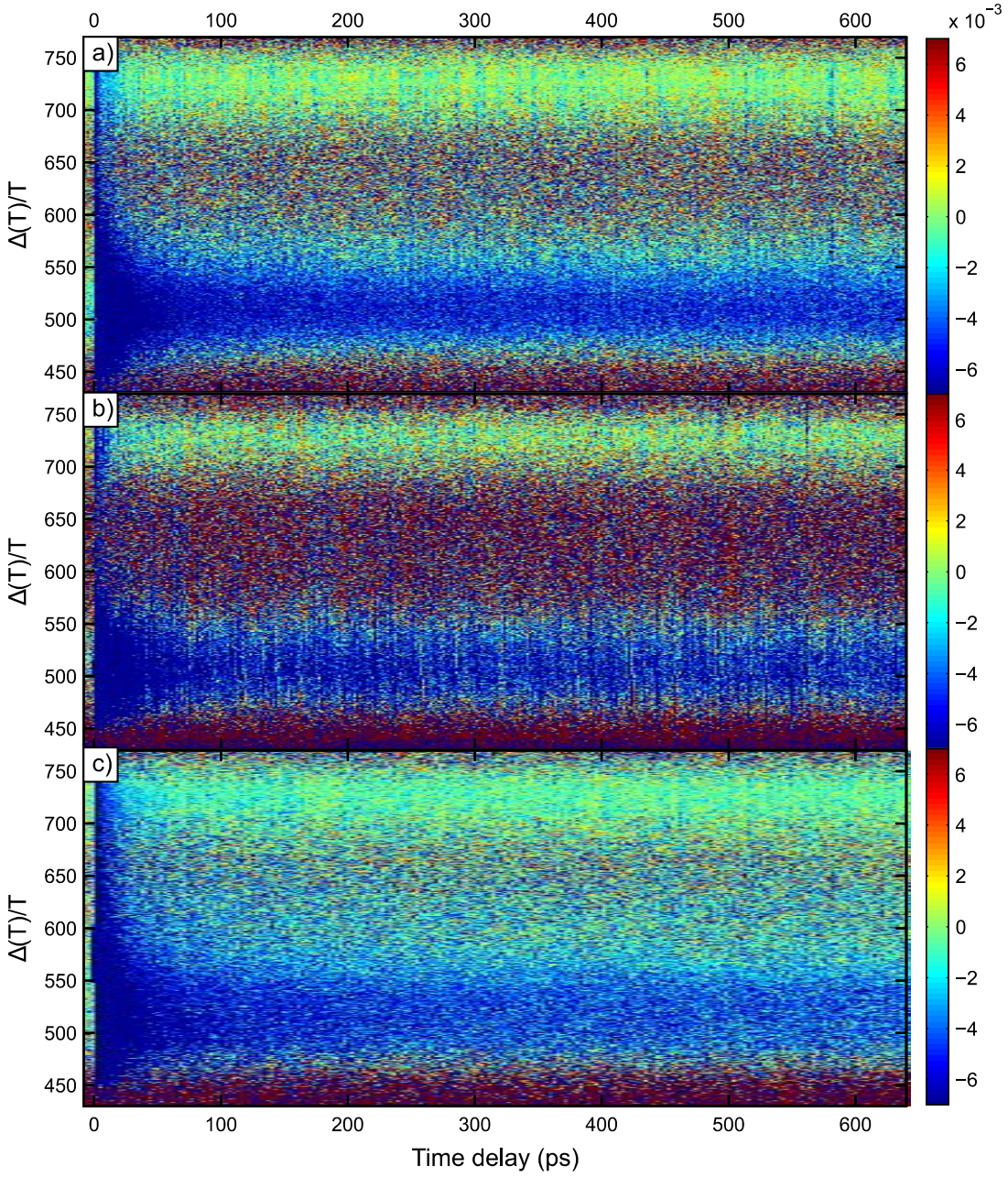

Figure 11-4 Relative change of the transient transmission for sample 17 for different thicknesses. a) 705nm, b) 846nm) 1081nm. (See the discussion in chapter 6.2.2)

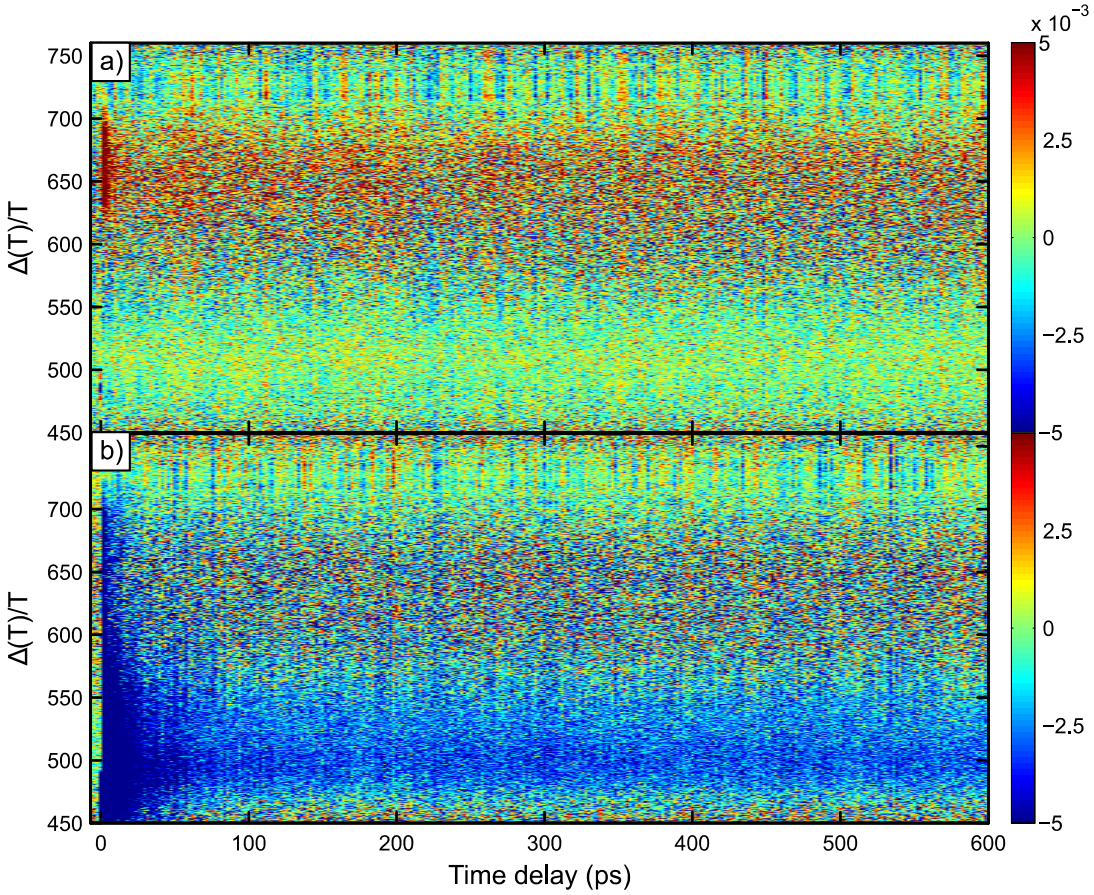

Figure 11-5 Relative change of the transient transmission for sample 15 a) GNR type II on 8 dl PSS/PAH on Quartz b) GNRs and 60 dl PAzo/PAH on top. (See the discussion in chapter 7.1.1)

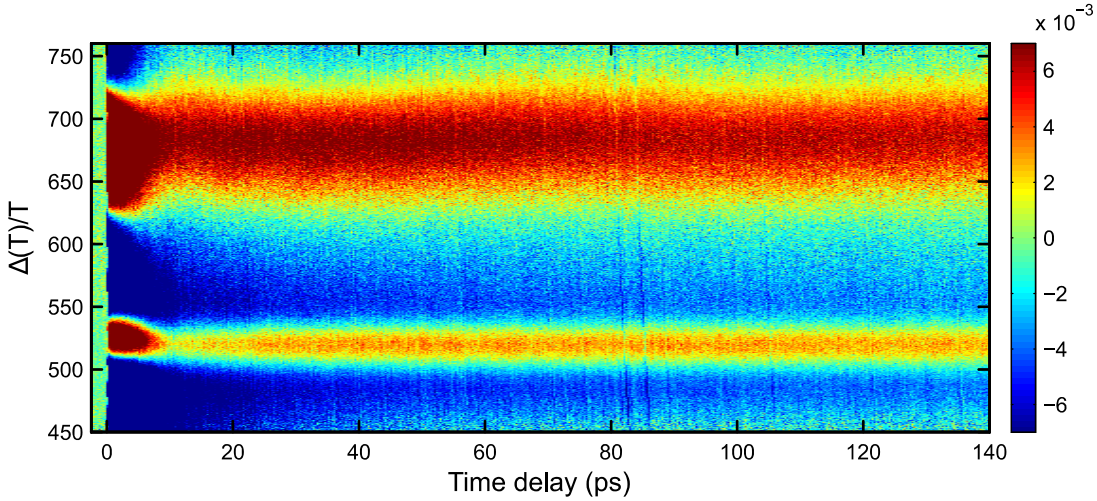

Figure 11-6 Relative change of the transient transmission for sample 40 (Quartz – 90 dl PAzo/PAH – (GNR type III – 8 dl PSS/PAH)*8). (See the discussion in chapter 7.1.1)

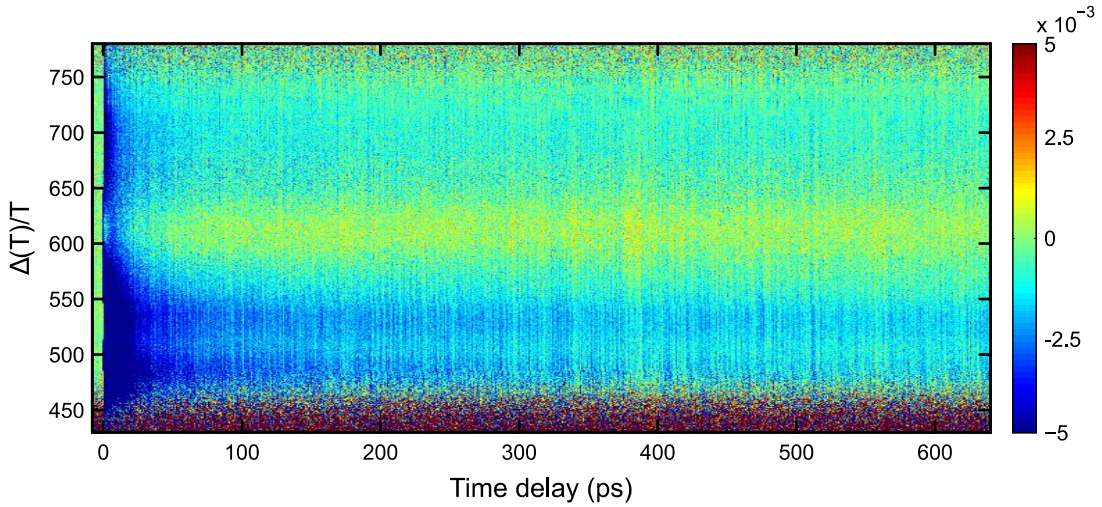

Figure 11-7 Relative change of the transient transmission for sample 52 (Quartz – 180 dl PAzo/PAH – 70 dl PSS/PAH – GNR IV). (See the discussion in chapter 7.2)

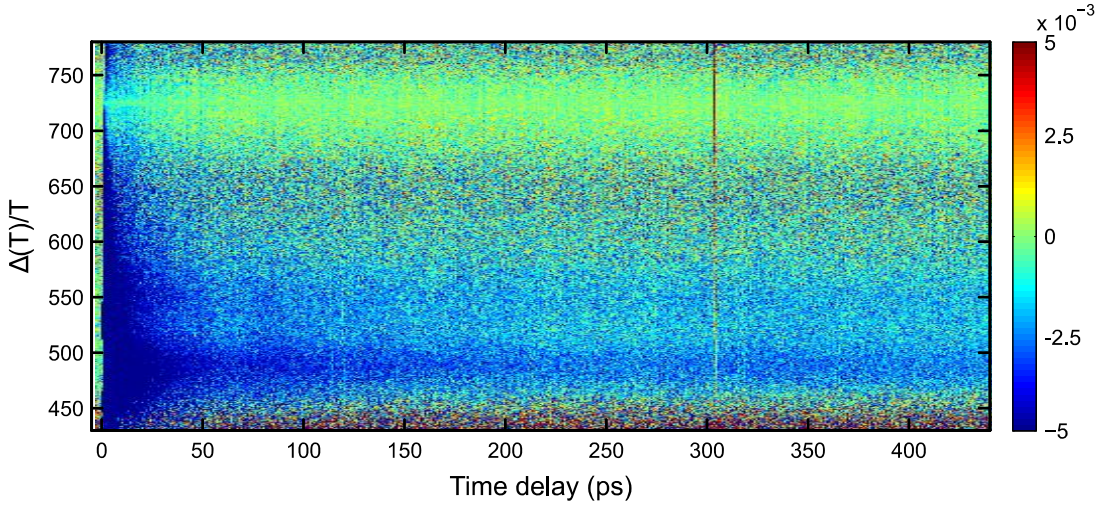

Figure 11-8 Relative change of the transient transmission for sample 22 (Quartz – 120 dl PAzo/PAH – 30 dl PSS/PAH – GNR III). (See the discussion in chapter 7.2)

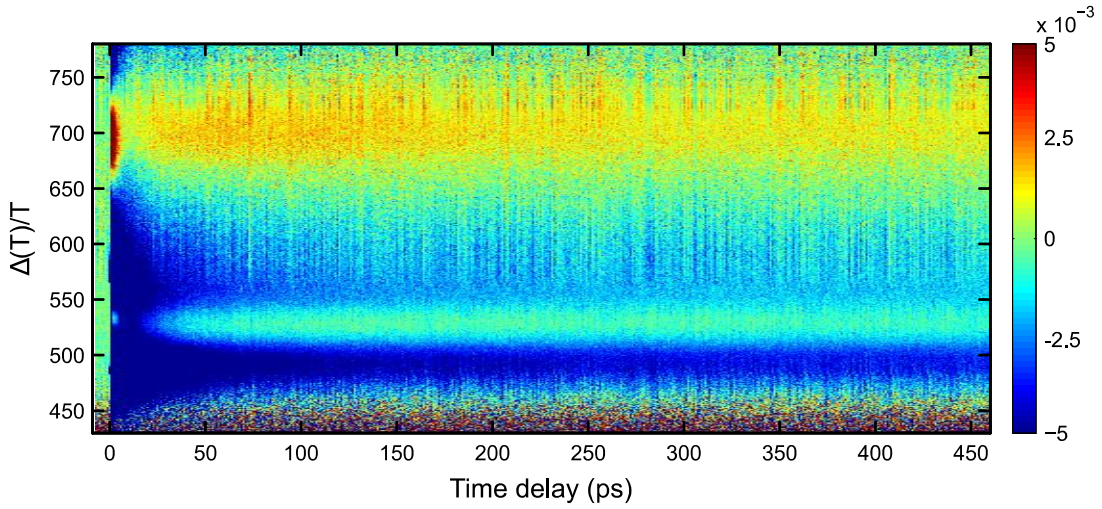

Figure 11-9 Relative change of the transient transmission for sample 45 (Quartz – 90 dl PAzo/PAH – (GNR III – 15 dl PAzo/PAH)*3 – 60 dl PAzo/PAH). (See the discussion in chapter 7.2)

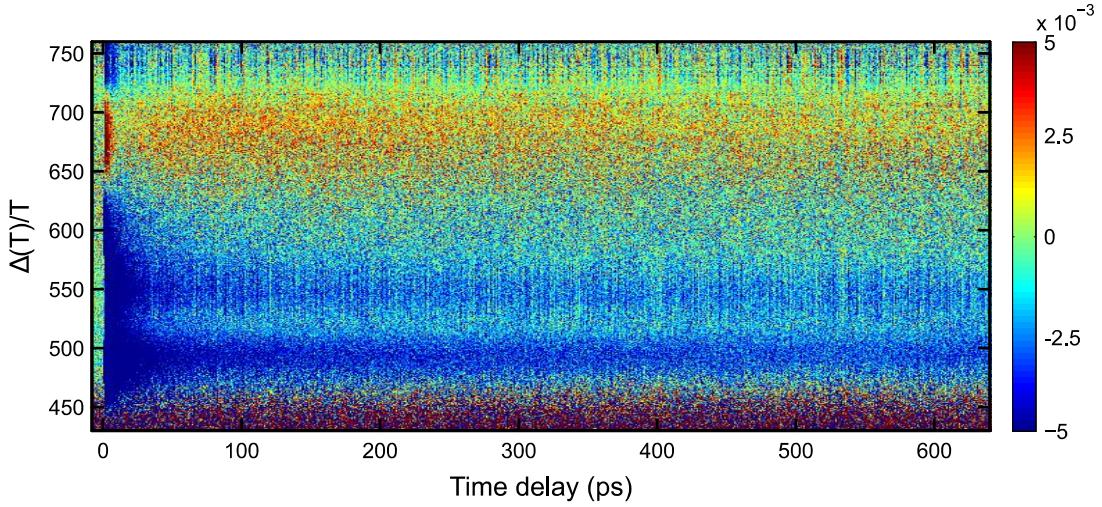

Figure 11-10 Relative change of the transient transmission for sample 52 after additional PSS/PAH on the top of the structure (Quartz – 180 dl PAzo/PAH – 70 dl PSS/PAH – GNR IV – 8 dl PSS/PAH). (See the discussion in chapter 8.2)

11.1. List of abbreviations

A	Absorption
BBO	Beta-barium borite
CTAB	Cetrimonium bromide
DL	Double layer
GNR	Gold nanorods
LBL	Layer-by-layer
OD	One drop
PAH	Poly (allylamine hydrochloride)
PEI	Poly (ethyleneimine)
PAzo	Poly [1-[4-(3-carboxy-4-hydroxyphenylazo) benzenesulfonamido]-1,2-ethanediyl, sodium salt]
PSS	Poly(sodium 4-styrensulfonate)
PR_T	Transverse plasmon resonance
PR_L	Longitudinal plasmon resonance
R	Reflection
RCTR	Relative change of the transient reflection
RCTT	Relative change of the transient transmission
SEM	Scanning electron microscopy
T	Transmission
TDBS	Time-domain Brillouin scattering
TFI	Thin film interference

Acknowledgments

First of all, I would like to express my sincere gratitude to Prof. Matias Bargheer. I particularly valued all the time he has dedicated to our numerous discussions and for all the help he offered during my PhD. His optimism and enthusiasm helped to drive my own inspiration throughout the work on this project. It was a great experience to work under the supervision of such actively involved supervisor, who besides being a specialist in quite a few areas is always opened for more areas to explore

I am also grateful to all the professors whose discussions and advice provided extensive contributions to this work. The expert opinion of Prof. Santer, and Prof. Möhwald have been especially useful.

Special thanks should be expressed to Andre Bojahr for all the help, advice, and knowledge that he enthusiastically shared. He helped me quickly familiarise myself with the topic in the beginning and provided great insights into the interpretation of the data at the later stages of the project.

I am also very grateful to Steffen Mitzscherling for help with the preparation technique, and to Qianling Cui for her excellent expertise in chemistry. Sample preparation was a big part of this project, and could not be done without the contribution of these former group members.

Moreover, I would like to thank Mathias Sander and Wouter Koopman for their contributions to numerous discussions and their expertise in the simulations of the data.

I am thankful to all my colleagues of the Ultrafast Dynamics in Condensed Matter group for various contributions via discussions and seminars.

Many thanks to all the participants of the graduate school SALSA (School of analytical sciences Adlreshof). This school made it possible to exchange lots of interdisciplinary knowledge between students and professors, which was a great experience and contributed to my development as a scientist. Special thanks go to Esther Santel and Katharina Schultens for their great support and patience.

Finally, I would like to thank my family and close friends. Even being separated by thousands of kilometers, their support was strong and very, very helpful.

Thank you!

Statement of Authorship

I hereby certify that this dissertation was written independently and without assistance from third parties. Other than the stated sources and aids were not used. Parts of the sources that have been used verbatim or in substance are identified as such. This dissertation has not been presented in the same or similar form to any audit authority and was not published.

Potsdam 20.06.2016

_____

(Elena Pavlenko)